THE UNIVERSITY OF OKLAHOMA

GRADUATE COLLEGE

ULTRASONIC PULSE PROPAGATION IN THE COLD-WORKED LAYER OF RAILROAD RAIL

A DISSERTATION

SUBMITTED TO THE GRADUATE FACULTY

in partial fulfillment of the requirements for the

degree of

DOCTOR OF PHILOSOPHY

BY

DONALD EUGENE BRAY

Norman, Oklahoma

1976

ULTRASONIC PULSE PROPAGATION IN THE COLD-WORKED LAYER OF RAILROAD RAIL

APPROVED BY

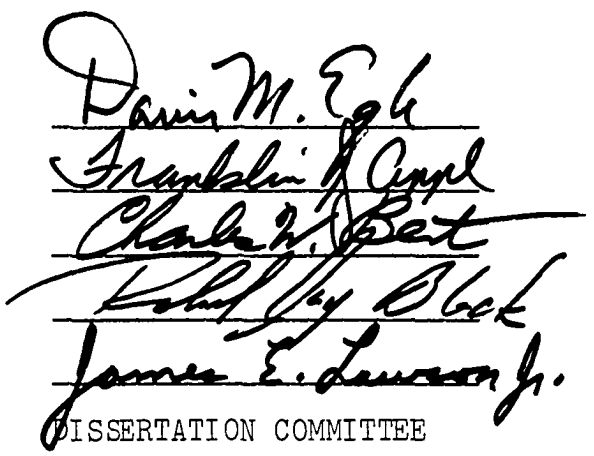

DISSERTATION COMMITTEE

ACKNOWLEDGEMENTS

As with any dissertation, it is hoped that the results reported herein can serve some useful purpose. Even if that does not turn out to be the case, this dissertation still represents the culmination of three years of very enjoyable work on the part of the author. This endeavor has certainly not been an individual effort. Many persons have contributed in various ways to the completion of the task.

First, the author's graduate advisor, Dr. Davis M. Egle, has continually provided a unique combination of technical and academic leadership that will always be gratefully remembered. The other members of the dissertation committee have also generously contributed their expertise to this effort. These include Dr. Charles W. Bert, Jr. and Dr. Franklin J. Appl of the School of Aerospace, Mechanical and Nuclear Engineering and Dr. Robert J. Block of the School of Chemical Engineering and Materials Science. Before leaving The University of Oklahoma School of Geology and Geophysics, Dr. Leon Reiter was of considerable help in the layered-wave propagation studies that were crucial to the early part of the work. Dr. James E. Lawson, Jr. of The University of Oklahoma Earth Sciences Observatory then joined the committee and provided many helpful comments on the dissertation.

Mr. William B. O'Sullivan of the Federal Railroad Administration, Department of Transportation, and Dr. William J. Harris, Jr. of the Association of American Railroads were jointly responsible for the financial support which made this work possible. Mr. W. S. Autrey, Chief Engineer, and Mr. C. W. Groh, Assistant Division Engineer, both of the Santa Fe Railway, were generous in their donation of both time and materials to this project.

The completion of the graduate studies and the dissertation could not have been attained without the sympathetic encouragement of my wife, Elizabeth, and the tolerance of my sons, Jeff and Ben. The readability and the appearance of the manuscript have been greatly enhanced by the diligent editing and typing efforts of my wife.

There are, of course, many others who contributed to the completion of this research through discussions, comments, etc. Although they cannot all be individually named, their assistance is appreciated.

TABLE OF CONTENTS

	Page
ACKNOWLEDGEMENTS	iii
LIST OF TABLES	vi
LIST OF FIGURES	viii
LIST OF SYMBOLS	xiv
Chapter	
I. INTRODUCTION	1
II. THE RAIL HEAD AND THE COLD-WORKED LAYER . .	10
Cold Working of the Rail Head During Service	14
Microstructure of the Cold-Worked Zone . . .	18
Effect of the Cold-Worked Zone on Crack Growth	22
Texture of Cold-Worked Steel (Preferred Orientation)	22
Wave Velocities and Isotropic Poisson's Ratios for New and Used Rail	25
Shear Wave Velocities and Critical Refraction Angles in the Cold-Worked Layer	27
III. WAVE PROPAGATION IN THE COLD-WORKED LAYER .	33
Wave Propagation in Layered Media	42
Computation of Phase and Group Velocities for the Fundamental and First Shear Mode (Geophysical and Rail Models)	52

TABLE OF CONTENTS (CONT'D.) Page

Summary and Conclusions 72

IV. WAVE VELOCITY CHANGES IN COLD-WORKED MATERIAL 73

Effect of Residual Stress on Velocity Change in the Cold-Worked Layer 74

Effect of Preferred Orientation (Texture) on the Velocity Change in the Cold-Worked Layer 78

Texture Models for Determining Preferred Orientation in Used Rail 80

Experimental Investigations of Velocities in Cold-Worked Samples 100

Experimental Investigations of Velocity Variations in Rail Samples 106

Summary and Conclusions 119

V. SUMMARY, SUGGESTIONS FOR FURTHER WORK, AND CONCLUSIONS 120

Suggestions for Further Work 124

Conclusions 126

REFERENCES 127

APPENDICES

A. PULSE CHARACTERISTICS AND ULTRASONIC CIRCUITRY. . 133

B. ARRIVAL TIME DETERMINATION 136

LIST OF TABLES

TABLE		Page
I.	Chemical Composition of Rail Steel [7]	13
II.	Typical Mechanical Properties of Control-Cooled Rail Steel [8]	13
III.	Wave Velocities and Isotropic Poisson's Ratios for the Rail Head	27
IV.	Wave Arrival Times and Velocities	39
V.	Computational Parameters for Geophysical and Rail Models	53
VI.	B_1T/H, C_R/B_1 and C_S/B_1 for Rails Seven and Eleven	61
VII.	B_1T/H, C_R/B_1 and C_S/B_1 for New Values of B_1 . .	65
VIII.	Material Constants for Iron	86
IX.	Textures in Worked Steel	89
X.	Predicted Velocities from Various Ideal Textures (m/s)	96
XI.	Description of Laboratory Samples Used in Texture Investigations	102

LIST OF TABLES (CONT'D.)

TABLE Page

XII. Experimental Results of Velocity Measurements in Rail Samples (m/s) 108

XIII. Summary of Comparable Wave Velocities from Studies of Layered-Media Wave Propagation and Material Texture 123

LIST OF FIGURES

FIGURE		Page
1.	Apparatus for Surface Wave Measurements on Full-Sized Rail [6]	5
2a.	Pulse Arrivals at 100 mm Increments, Rail No. 7, 119 lb. Used Rail, Freq. 1.7 MHz, Time Base 50 μs/div. [6]	7
2b.	Pulse Arrivals at 100 mm Increments, Rail No. 7, 119 lb. Used Rail, Freq. 1.7 MHz, Time Base 5 μs/div. [6]	7
2c.	Pulse Arrivals at 100 mm Increments, Rail No. 8, 115 lb. New Rail, Freq. 1.7 MHz, Time Base 50 μs/div. [6]	7
2d.	Pulse Arrivals at 100 mm Increments, Rail No. 8, 115 lb. New Rail, Freq. 1.7 MHz, Time Base 5 μs/div. [6]	7
3a.	Pulse Arrivals at 100 mm Increments, Rail No. 7, 119 lb. Used Rail, Freq. 0.5 MHz, Time Base 50 μs/div. [6]	8
3b.	Pulse Arrivals at 100 mm Increments, Rail No. 7, 119 lb. Used Rail, Freq. 0.5 MHz, Time Base 5 μs/div. [6]	8

LIST OF FIGURES (CONT'D) Page

3c. Pulse Arrivals at 100 mm Increments, Rail No. 8, 115 lb. New Rail, Freq. 0.5 MHz, Time Base 50 μs/div. [6] 8

3d. Pulse Arrivals at 100 mm Increments, Rail No. 8, 115 lb. New Rail, Freq. 0.5 MHz, Time Base 5 μs/div. [6] 8

4. Cross-Section of 57.0 Kg/m (115 lb/yard) Rail [6] 11

5. Variation in the Longitudinal Residual Stress Pattern in New and Used Rail [11] 15

6. Plane-Strain Compression for $\Delta = 5$ [13] . . . 17

7. Overall View of a Used 119 lb. AREA Rail Head (3.3 X, Villa's Etch), Block [6] 19

8. Section Through the Top of the Used Rail Head (100 X, Nital Etch), Block [6] 21

9. Growth Rings for Transverse Fracture in Rail (Courtesy Sperry Rail Service 23

10. Transverse Fracture in Rail (Courtesy Sperry Rail Service) 23

11. Shear Wave Velocity in Rail Top Layer Versus Sine of Excitation Angle in Plastic Wedge 29

12. Schematic of Apparatus Used on Full-Sized Rail [6] 34

13. Probe and Guide Arrangement for Surface Wave Measurements 36

14. First Shear and Fundamental Rayleigh Mode Arrivals in Rail 11 at 0.5 MHz, 0.7MHz, 1.0 MHz, 1.7 MHz, and 2.0 MHz, Time Base 50 μs/div. . 41

15. Structural Model for Layered Wave Propagation Studies 44

16. Phase and Group Velocities for Fundamental Rayleigh and First Shear Mode Geophysical Model 54

17. Displacements for the Fundamental Rayleigh and First Shear (Sezawa) Modes for $B_1T/H = 2.5$ [40] 57

18a. Phase and Group Velocities and Experimental Data for Rail Seven 59

18b. Phase and Group Velocities and Experimental Data for Rail Eleven. 59

19a. Phase and Group Velocities and Experimental Data for Rail Model 7A 66

19b. Phase and Group Velocities and Experimental Data for Rail Model 11A 66

20. Cubic Crystal 81

21. Stereographic Projection System 81

22a. Isospeed Contours for Longitudinal Waves in Iron [v_1(m/s)] 85

22b. Isospeed Contours for Slow Shear Waves in Iron [v_2(m/s)] 85

22c. Isospeed Contours for Fast Shear Waves in Iron [v_3(m/s)] 85

23. Velocities for (100)[001] Texture in Horizontal and Vertical Planes 91

24. Velocities for (100)[011] Texture in Horizontal and Vertical Planes 92

25. Velocities for (110)[001] Texture in Horizontal and Vertical Planes 93

26. Velocities for $(\bar{5}31)$[112] Texture in Horizontal and Vertical Planes 94

27. Specimens for Rail Texture Studies 101

28. Ultrasonic Goniometer 103

29. Fast Shear Wave Arrivals Propagating in the Horizontal Plane at 90° to the Rolling Direction. Top

Trace-Propagation Through Worked Layer, Bottom Trace-Propagation Through Center Section.(Time Base 0.2 μs/div.). 110

30a. Fast and Slow Shear Wave Arrivals Propagating Through the Worked Layer in the Vertical Plane and at 90° to the Rolling Direction (Specimen T10) Top Trace - 0° Polarization, Bottom Trace - 90° Polarization. (Time Base 0.5 μs/div.). . . 110

30b. Fast and Slow Shear Wave Arrivals Propagating Through the Upper Layer of New Rail in the Vertical Plane and at 90° to the Rolling Direction (Specimen T13) Top Trace - 0° Polarization, Bottom Trace - 90° Polarization. (Time Base 0.5 μs/div.). . 110

31. Experimental Data and Predicted Velocities for (100) [001] Texture 113

32. Experimental Data and Predicted Velocities for (100) [011] Texture 114

33. Experimental Data and Predicted Velocities for (110) [001] Texture 115

34. Experimental Data and Predicted Velocities for ($\bar{5}$31) [112] Texture 116

LIST OF FIGURES (CONT'D) Page

35. Basic Ultrasonic Pulse Circuit [61] 133

36. Shear Wave and Rayleigh Wave Arrivals at 2.0 MHz on Rail 11 Vertical 0.2 v/div., Time Base 50 μs/div. 137

LIST OF SYMBOLS

Symbol	Definition
A_1, A_2	Dilatational wave velocities in layers 1 and 2, respectively
B_1, B_2	Shear wave velocities in layers 1 and 2, respectively
A_1', B_1'	Dilatational and shear wave velocities in layer 1 resulting from residual stress variation
c	Variable capacitance in ultrasonic circuitry
$c_{ijk\ell}$, c_{ij}	Second order elastic constants
C	Phase velocity
C_1	Incident dilatational wave velocity
C_2	Refracted shear wave velocity
C_o	Capacitance of piezoelectric plate
C_R	Rayleigh wave velocity
C_S	Shear wave velocity
Cr_1, Cs_1	Hyperbolic parameters for solving wave equation
C^o	Unstressed wave velocity
CKH, CDT	Computational parameters
D(a,b)	Matrix elements for determinant of wave equation
E_1, E_2	Computational parameters for solving wave equation
f	$= \omega/2\pi$, frequency in Hz
f_{re}, f_{rm}	Electrical and mechanical resonant frequency of piezoelectric plates, respectively
h	Thickness of metal specimen

Symbol	Definition
H	Thickness of layer one
k	= ω/C, wave number
h, k, ℓ	Miller indices
i	= 1, upper layer one; = 2, underlying structure
i, j, k, ℓ	Indices in crystal elasticity
ℓ_ℓ, ℓ_j	Direction cosines
L	Length of indenter
L	Inductance in ultrasonic circuit
M	Ratio of shear moduli in layers one and two
M	Mass of transducer material
M_{21}	Sezawa or first shear mode
P_1, P_2	Computational parameters for solving wave equation
r	Variable resistance in ultrasonic circuit (damping)
s	Mechanical stiffness of transducer material
Sr_1, Ss_1	Hyperbolic parameters for solving wave equation
SV	Shear wave with particle motion in the vertical direction
t_R	Arrival times for Rayleigh waves
t_S	Arrival times for shear waves
T	= 1/f, Wave period
T_1, T_2, T_3, T_4, T_5, T_6	Computational parameters for solving wave equation

LIST OF SYMBOLS (CONT'D)

Symbol	Definition
u	Particle velocity in the horizontal direction
U	Group velocity
U_s	High voltage electrical spike in ultrasonic circuitry
v	Phase velocity
v	Particle velocity in the vertical direction
v_0	Velocity of indenter in cold working
v_1	Velocity of particle moving out of the worked zone during deformation
v_1	Velocity of a pure longitudinal mode having particle motion in the direction of the wave-front normal
v_2, v_3	Velocities of pure transverse modes having particle motions perpendicular to the wave normal and also mutually perpendicular
δ	Angle of deviation between wave normal and direction of energy flux
δ_{ik}	Kronecker delta
Δ	= h/L, Cold working parameter
ϵ	Strain
θ	Angle between rolling direction and direction of wave propagation
θ_1, θ_2	Excitation and refraction angles at the interface
λ_{ik}	$= c_{ijk\ell}\ell_\ell\ell_j$, Elasticity parameter
λ, μ	Lamé parameters
λ_1, λ_2 μ_1, μ_2	Lamé parameters for layers one and two, respectively

LIST OF SYMBOLS (CONT'D)

Symbol	Definition
ν_1, ν_2	Poisson's ratio for layers one and two, respectively
ρ	Density
ρ_1, ρ_2	Density for layers one and two, respectively
ω	Frequency in radians per second
$(hk\ell)$	Crystallographic plane
$[hk\ell]$	Crystallographic direction
$\{hk\ell\}$	Crystallographic "planes of the form"
$\langle hk\ell \rangle$	Crystallographic "directions of the form"
$(hk\ell)[hk\ell]$	Crystallographic texture with $(hk\ell)$ plane parallel to rolling plane and $[hk\ell]$ aligned parallel to rolling direction

ULTRASONIC PULSE PROPAGATION IN THE COLD-WORKED LAYER OF RAILROAD RAIL

CHAPTER I

INTRODUCTION

The distinguishing characteristic of railway transportation is the flanged steel wheel rolling over a steel rail. This simple feature provides the advantages of guidance and mechanical efficiency which make railways uniquely suited for the movement of a large portion of the goods and people transported in the United States and the rest of the world.

The advantages in energy consumption of the high mechanical efficiency of railway movement have been well documented in the recent literature. For examples of this see Ref. [1,2]. It is reasonable to expect that more prudent use of our natural resources will force an increase in the traffic carried by the world's railways. Also, more efficient railway operations, such as an increased emphasis on unit container trains which bypass switching yards [3],

could attract an even greater amount of goods traffic. A similar situation exists for passenger traffic where, in the future, high-population-density corridors will most likely see an increase in travel by rail vehicle [2].

An increase in the travel speed and in the utilization of rail vehicles must occur if the rail systems are to accommodate this projected increase in rail traffic. At the present time the fastest passenger train speed in the United States is nearly 161 km/hr (100 mi/hr) for the Metroliners operating between Washington and New York. Speeds approaching and possibly exceeding the 210 km/hr (130.5 mi/hr) speed of the Japanese National Railway's Shinkansen operation are likely to occur in the United States. Better freight car utilization as well as the integral-train concept previously mentioned can greatly increase the freight capacity of United States railways. At the present time, the average United States freight car spends only about twelve percent (12%) of its time moving in trains. The rest of the time is spent in being loaded or unloaded, in terminal movements, in classification operation, or in standing still [4]. The potential for handling increased traffic through greater car utilization is obvious.

The average load of a typical rail freight car has dramatically increased in recent years. In 1955 this load was $38.5(10)^3$ kg (42.4 tons). By 1974 it had risen to approximately $52.6\ (10)^3$ kg (58 tons), representing an increase

of nearly thirty-seven percent (37%).

The parameter which most directly indicates the useful work output of freight railways is the revenue ton-mile. This increased from 623.6 billion in 1965 to 853.9 billion in 1974, also representing an increase of approximately thirty-seven percent (37%). The similarity of this increase and that for car loads alone indicates that in the past the increased productivity has come about primarily because of the heavier loading of cars.

In most mechanical systems, increased loadings can be accommodated through design changes. This is partially true, also, for the freight car. Track, however, cannot be quickly upgraded in order to handle the increased forces brought about by the heavier cars. Much of the main-line rail in use today was installed before 1955 and, thus, was not specifically designed to carry the greater loads of today's cars.

There is reason to believe that the increased load has had a significant effect of railway accidents, as indicated in Ref. [5]. More specifically, the two components that are engaged in rolling contact, the wheel and rail, showed the highest correlation between changes in the annual rate of accidents and ton-miles.

It has been postulated that these increased loadings have led to a greater tendency for rail failure to occur due to shelling. Shelling in rail is a result of extreme plastic

flow and cold working of material in the upper layer of the rail head. The research discussed in this dissertation is the result of an investigation of the ultrasonic-wave-propagation characteristics of the cold-worked layer on the head of used rail.

The current interest in the worked zone originated with an earlier study of the wave-propagation characteristics of the head and web of full-sized rail [6]. In the earlier study, surface waves were sent and received along the surface of the head of the rail by identical transducer assemblies.

Fig. 1 shows the arrangement of the laboratory equipment used in the original study. Although more detail regarding the equipment has been given in Chapter III, some general comments will be useful at this time. The sending and receiving surface wave probes shown in the center of the photograph are clamped on top of one of the several rails used in the study. The sending transducer, located on the right, was connected with a coaxial cable to the pulsing unit on the right. A box for adding a separate tuning coil to the circuit is shown in front of the pulser. The ultrasonic pulse, travelling essentially along the top of the rail, was detected by the receiving transducer shown on the left. This received signal was then displayed on the oscilloscope shown on the left. This apparatus is discussed in more detail in

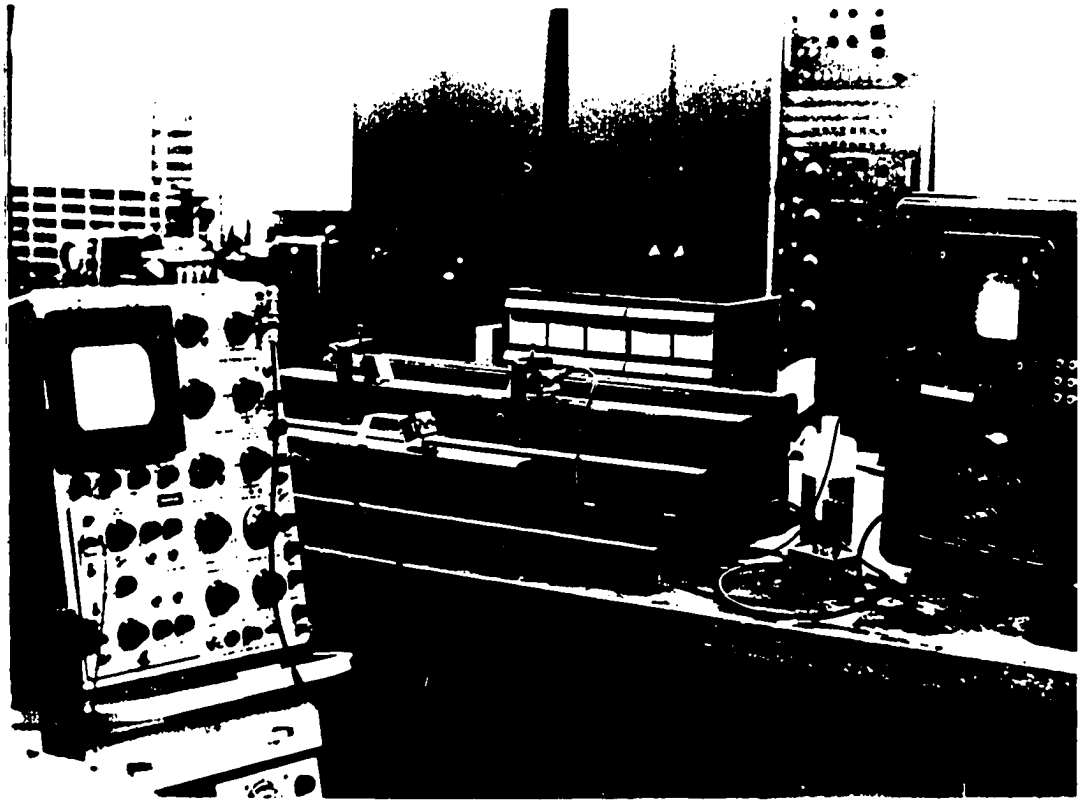

Figure 1. Apparatus for Surface Wave Measurements on Full-Sized Rail [6]

Chapter III (see Figs. 12 and 13 and related discussion). The shape of the source pulse is discussed in greater detail in Appendix A.

When the surface waves were propagated along the head of used rail at certain frequencies, an unexpected event occurred. An individual wave appeared which could be related to the presence of the cold-worked zone on the top of the rail head. The behavior of this wave was such that, for high frequencies (approximately 1.0-2.0 MHz) in most of the used rail, it appeared quite distinctly just ahead of the expected surface wave arrival. Figs. 2a and 2b show the smaller early arrival just ahead of the larger Rayleigh (surface) wave arrival at a pulse frequency of 1.7 MHz. Pulse arrivals are shown at transducer spacings starting at 100 mm and increasing in 100 mm increments from the top trace to the lower. Fig. 2b is an expansion of the arrivals shown in Fig. 2a. At high frequencies in new rail (Figs. 2c and 2d) and at lower frequencies in used rail (Figs. 3a and 3b), the early arrival was hardly noticeable, if at all. Since the occurrence of the wave and its velocity appeared to be frequency related, it could not be explained as a simple, bulk shear wave.

Chapter II, which follows, presents a discussion of the stress distribution and the cold-worked area in the rail head. This includes material on the mechanism of cold working of metals through small contact areas. Chapter III presents the development of a model, based on seismology,

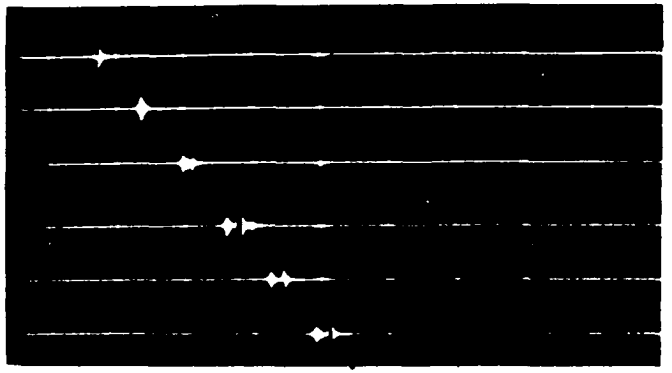

Figure 2a. Pulse Arrivals at 100 mm Increments, Rail No. 7, 119 lb. Used Rail, Freq. 1.7 MHz, Time Base 50 μs/div. [6]

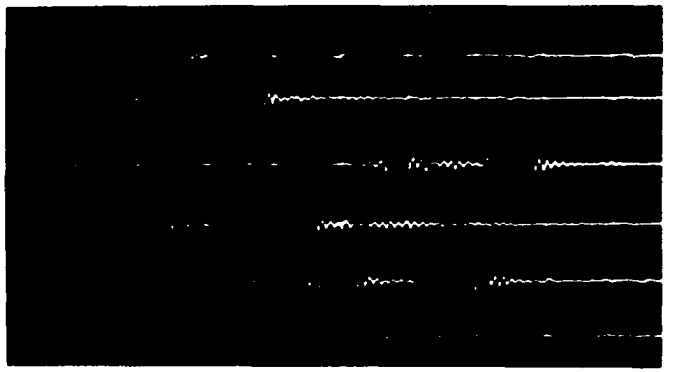

Figure 2b. Pulse Arrivals at 100 mm Increments, Rail No. 7, 119 lb Used Rail, Freq. 1.7 MHz, Time Base 5 μs/div. [6]

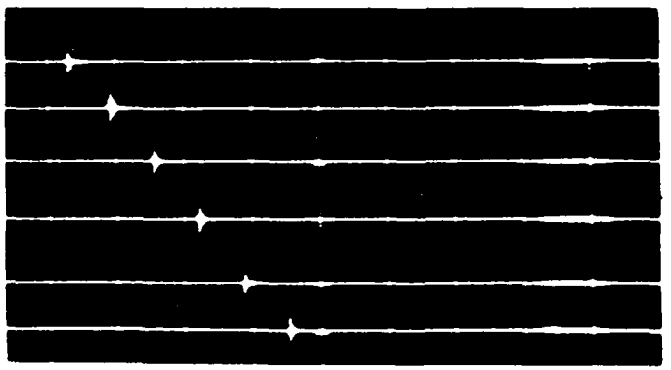

Figure 2c. Pulse Arrivals at 100 mm Increments. Rail No. 8, 115 lb. New Rail, Freq. 1.7 MHz, Time Base 50 μs/div. [6]

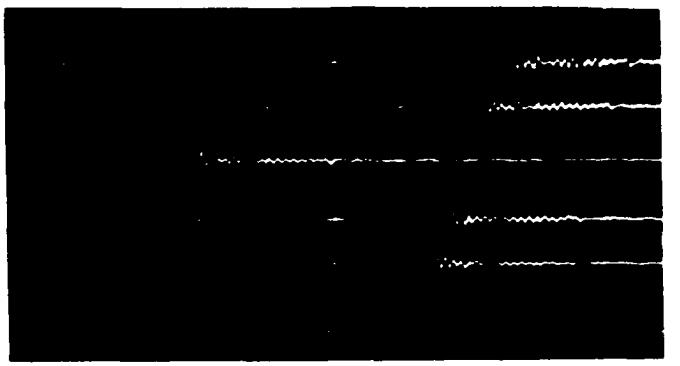

Figure 2d. Pulse Arrivals at 100 mm Increments, Rail No. 8, 115 lb. New Rail, Freq. 1.7 MHz, Time Base 5 μs/div. [6]

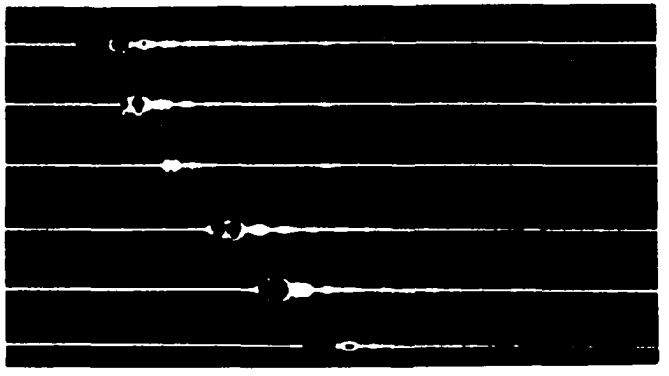

Figure 3a. Pulse Arrivals at 100 mm Increments, Rail No. 7, 119 lb. Used Rail, Freq. 0.5 MHz, Time Base 50 μs/div. [6]

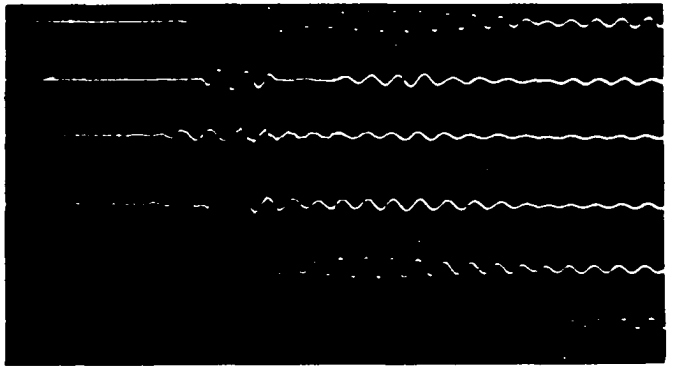

Figure 3b. Pulse Arrivals at 100 mm Increments, Rail No. 7, 119 lb. Used Rail, Freq. 0.5 MHz, Time Base 5 μs/div. [6]

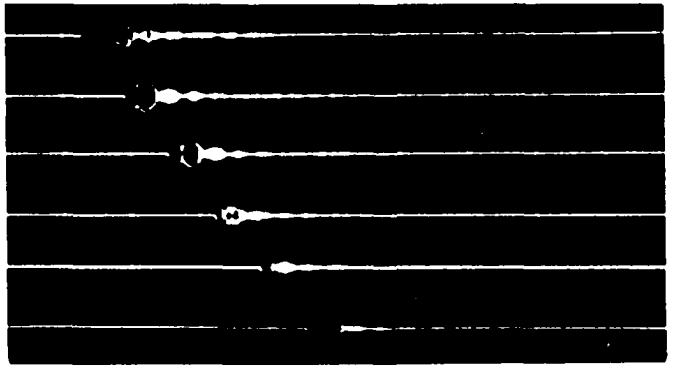

Figure 3c. Pulse Arrivals at 100 mm Increments, Rail No. 8, 115 lb. New Rail, Freq. 0.5 MHz, Time Base 50 μs/div. [6]

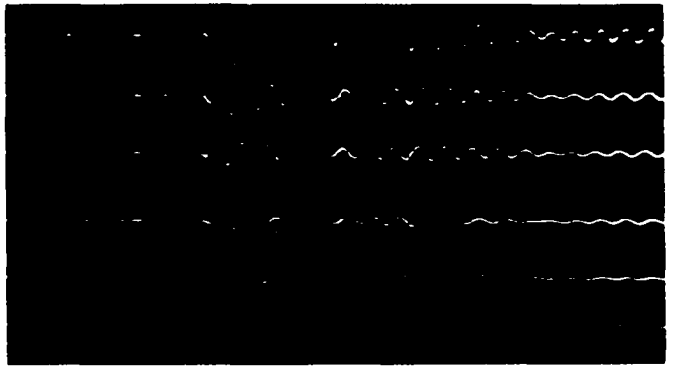

Figure 3d. Pulse Arrivals at 100 mm Increments, Rail No. 8, 115 lb. New Rail, Freq. 0.5 MHz, Time Base 5 μs/div. [6]

which attempts to identify and explain the wave-propagation patterns observed in the earlier study [6]. Following that, Chapter IV discusses residual stress and material texture (preferred orientation) resulting from the cold rolling of the rail surface to show how the observed wave speed changes could occur. The results are summarized in Chapter V.

CHAPTER II

THE RAIL HEAD AND THE COLD-WORKED LAYER

The early period of railroading saw the appearance of a number of proposed rail shapes [7]. These included a flat plate, one resembling a conventional angle iron lying on its side, and the tee-rail. The tee-rail began to resemble modern rails in the middle of the 1800's. By 1947 the typical shape shown in Fig. 4 had become standard in the United States.

In standard practice, the particular rail section is identified by the source of the specification and the nominal weight per yard. For example, the section shown in Fig. 4, AREA 115, is a 57.0 kg/m (115 lb/yard) rail as specified by the American Railway Engineering Association (AREA).

Rails most commonly used range in weight from 39.5 kg/m (80 lb/yard) to 69.5 kg/m (140 lb/yard). The lighter rail is typically used for branch and switching-line service while the heavier sections (e.g., 49.6 kg/m (100 lb/yard and over)) go in main-line track. Rail height is the most significant

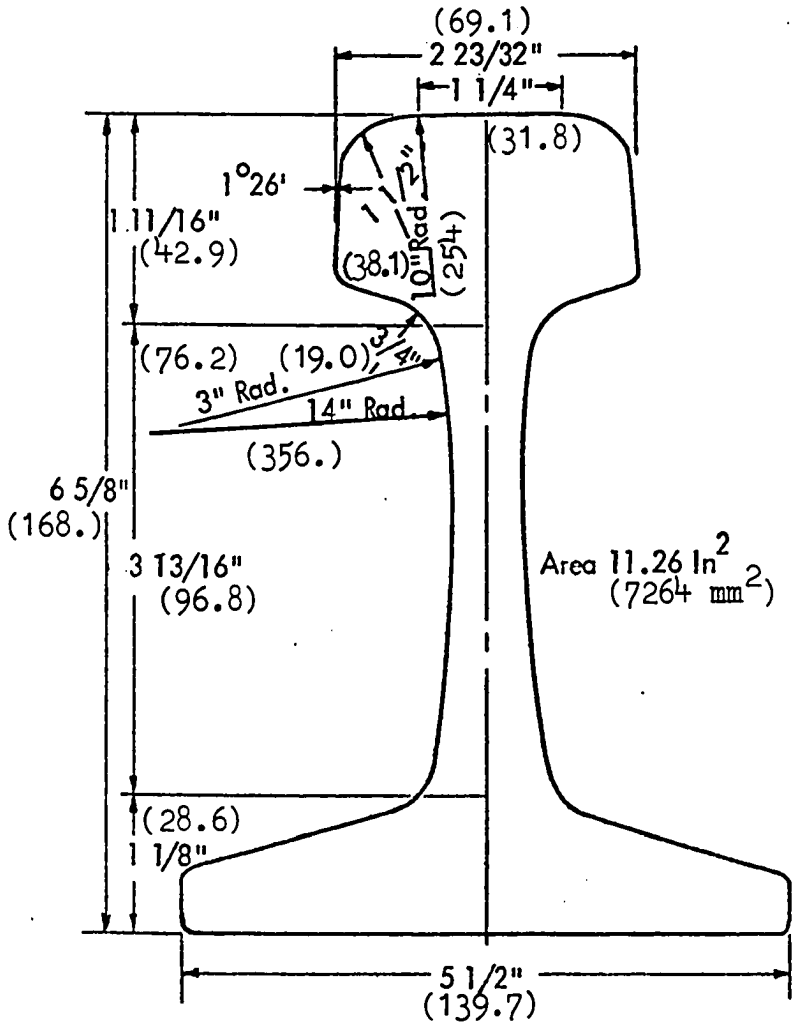

Figure 4. Cross-Section of 57.0 kg/m (115 lb/yard) Rail (Dimensions in millimeters are shown in parenthesis) [6]

difference in the various sections, since this greatly affects the section modulus and, hence, the strength in bending. The head width varies from 63.5 mm (2.5 in) for the 39.7 kg/m (80 lb/yard) rail to 76.2 mm (3.0 in) for the 140 lb/yard section. Similarly, the head height varies from 38.1 mm (1.5 in) to 52.4 mm (2.062 in) for these two sections.

The chemical composition of rail steel is shown in Table I. Table II shows typical mechanical properties of the steel used for conventional rail in the United States [8].

Rail manufacturing processes , as reviewed in Ref. [6], can affect the material properties. The cooling process and the resulting residual stress patterns are most pertinent to this work and will be briefly summarized here. One of the most significant changes in rail-making technology in recent years was the adoption of the controlled-cooling process. This process, which came into common use around 1937, virtually eliminated failure because of "shatter cracks." These defects, which are minute cracks caused by rapid or uneven cooling during manufacture, had been a serious threat to railroad safety.

The residual stress pattern in the control-cooled rail is much more favorable than that of the non-control-cooled type [9,10]. The controlled-cooling process begins shortly after the forged rails have been cut to length. They lie on a "hot bed" until their temperature falls approximately between 538° C to 386° C (1000° F to 725° F). Then the rails are placed in special rail cars used as controlled-cooling

Table I. Chemical Composition of Rail Steel [7]

Constituents (Percent)	Nominal Weight in Kilograms per Meter (Pounds per Yard)			
	34.7/39.7 (70/80)	40.2/44.6 (81/90)	45.1/59.5 (91/120)	60.0 and over (121 and over)
Carbon	0.55-0.68	0.64-0.77	0.67-0.80	0.69-0.82
Manganese	0.60-0.90	0.60-0.90	0.70-1.00	0.70-1.00
Phosphorous, Max.	0.04	0.04	0.04	0.04
Sulphur, Max.	0.05	0.05	0.05	0.05
Silicon	0.10-0.25	0.10-0.25	0.10-0.25	0.10-0.25

Table II. Typical Mechanical Properties of Control-Cooled Rail Steel [8]

Yield Strength	503.32 MN/m^2 (73,000 psi)
Tensile Strength	937.69 MN/m^2 (136,000 psi)
Elongation in 1 in. (25.4mm)	12.5%
Reduction of Area	24.5%

bins. A minimum of ten (10) hours is required for the rails to reach a maximum discharge temperature of approximately 149° C (300° F).

After emerging from the cooling bins, the rails are checked for straightness. If straightening is required, this is accomplished by a series of blows by a drop hammer.

The final residual stress pattern is a result of both the cooling and the straightening processes. The build-up of residual stresses from cooling can be visualized by noting that both the web and base of the rail are thinner than the head. As a result, the web and base cool quicker and achieve higher strength levels while the still hot head will readily yield. As the head cools, however, no yielding can take place in the rest of the rail, and tensile stresses due to shrinkage occur in the head. A typical pattern for longitudinal stresses in newly manufactured rail is shown by line A in Fig. 5 [11].

Cold Working of the Rail Head During Service

The contact area between the wheel and rail in railway operations has been represented as being an ellipse with a major diameter in the direction of travel of 14.33 mm (0.564 in) and a minor diameter of 11.99 mm (0.472 in). The resulting contact area is approximately 135 mm^2 (0.209 in^2). A typical static force of 117.4 kN (26,400 lbs) acts on this area [12]. The average contact stress is 870 MN/m^2 (126 ksi). This is a typical Hertzian contact stress problem, and

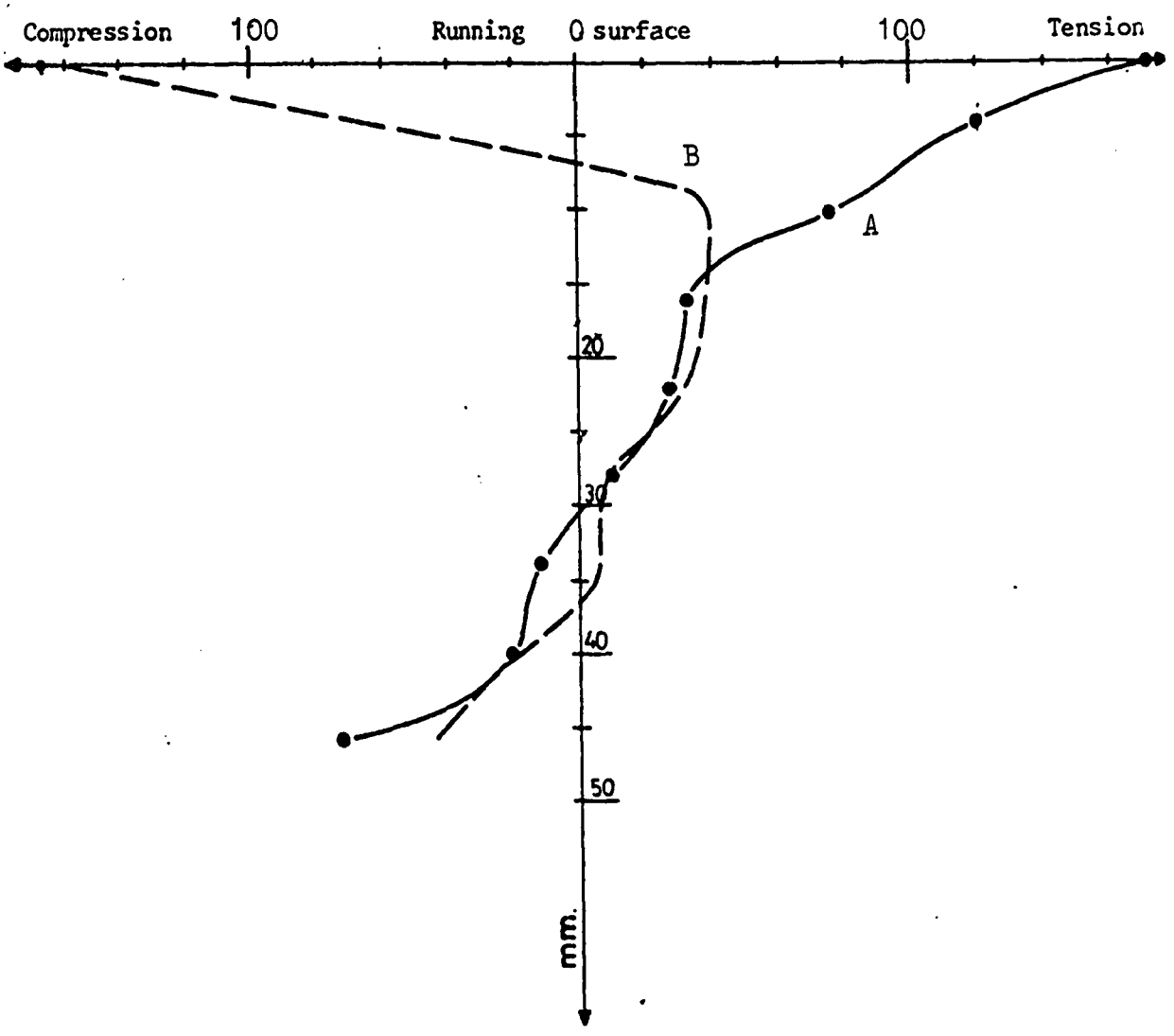

A - New rail made of standard-grade steel

B - Work-hardened rail made of standard-grade steel

Figure 5. Variation in the Longitudinal Residual Stress Pattern in New and Used Rail (MN/m^2) (With the permission of the ORE [11])

cold working results in both the wheel and rail.

Cold working of metals through small contact areas is a well known process in mechanical metallurgy. For discussion of the deformation zone geometry, Backofen defined the following terms [13]. The metal thickness (h) and the length of the indenter (L) are related by the expression $\Delta = h/L$. A value of Δ greater than one (1) is known to cause cold working of a layer near to the surface of the material. The higher the value for Δ, the closer the area of maximum cold work approaches to the surface.

Fig. 6 shows the plane-strain compression field for Δ equal to 5 [13]. In the illustration on the left, the field is considered to consist of four rigid masses. Recognizing the vertical symmetry, material movement follows two general paths. As indicated by the hodograph on the right, material moving at the velocity of the indenter, v_0, can flow at the respective velocities either across boundaries AB and AC or AB, BC and CD. Velocity discontinuities exist at each boundary. The resulting velocity of the departing material is v_1 where $v_1 = v_0/\Delta$.

Using the rail section shown in Fig. 4 as a typical example, a value of 37 mm (1.46 in) can be assumed for h. From the previous description of the contact zone, L can be assumed to be 12 mm resulting in a Δ of 3.08.

For that value of Δ, the contact pressure required to produce material motion is approximately three times the

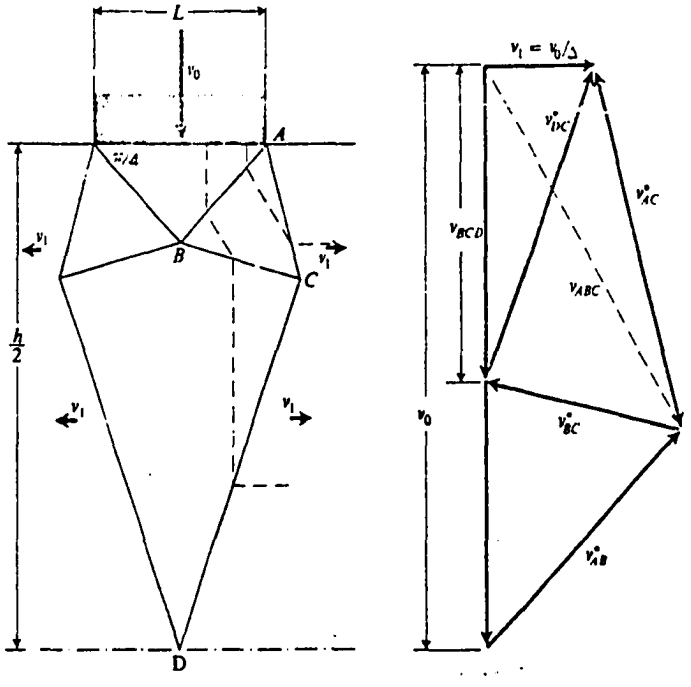

Figure 6. Plane-Strain Compression for $\Delta = 5$
(With Permission [13])

yield strength of the material in shear [13]. The compressive yield strength for a typical rail steel, as shown in Table II, is 503.32 MN/m^2 (73,000 psi). Considering yield strength in shear to be approximately one-half the compressive yield strength, the minimum contact pressure required for material movement is 754.98 MN/m^2 (109,500 psi). Using the earlier values for force and area, an estimate of a typical value of pressure caused by the wheel/rail contact is 870 MN/m^2 (126,315 psi). This exceeds the value required for material movement as calculated above.

Much of this analysis is not rigorous, mainly because exact wheel and rail geometry have been ignored, approximate values have been used, and dynamic forces have been neglected. It does serve, however, as a general description of the development of the worked zone on the rail head. A more complete discussion of these aspects of the rail/wheel contact problem has been given in Ref. [12], by Martin and Hay [14], Kalousek and Klein [15], and King and Kalousek [16]. Paul has recently presented a summary of past and present work in this area [17]. The argument presented here was felt to be most useful in demonstrating the process of cold working through small contact areas.

Microstructure of the Cold-Worked Zone

The microstructure of new and used rail has been studied by Block and reported in Ref. [6]. Fig. 7 is a

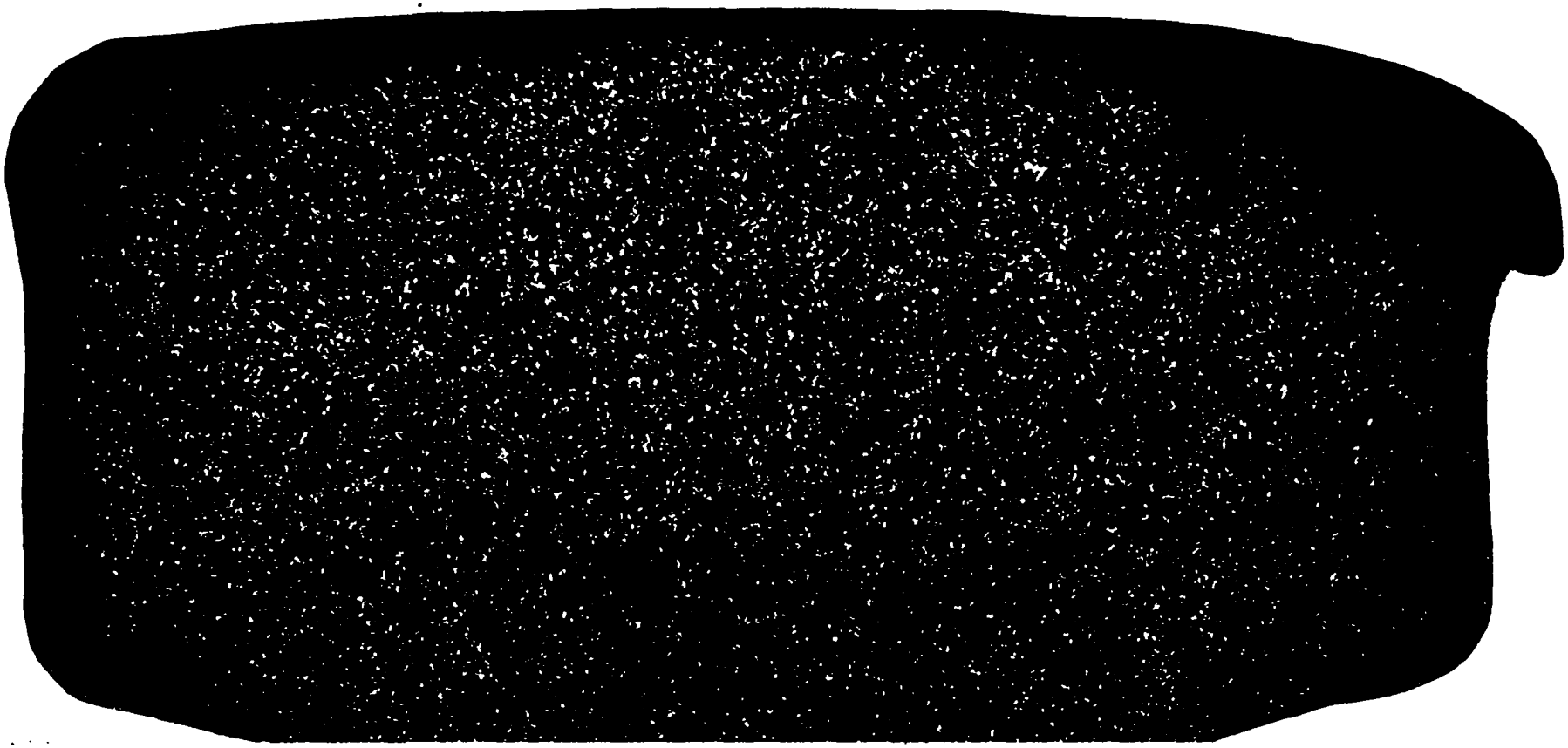

Figure 7. Overall View of a Used 119 lb. AREA Rail Head (3.3 X, Villa's Etch), Block [6]

microphotograph of rail number seven, a used 119 lb/yard rail. Records show that this rail had seen 293.6 $(10)^9$ kg (323.6 million gross tons) of main-line service. Its appearance indicates that it was probably installed as the low rail on a banked section of curved track. The change in microstructure is visible toward the top surface and toward the top corners. The upper 1.5 mm of the center portion of this rail is shown in Fig. 8. The depth of the very heavy distortions, distinguishable by unequal axes of the grains, ranges from approximately 1.5 mm at the center to 5 to 6 mm toward the corners. Lesser distortions appear at the center up to approximately 4 mm.

This estimate of the thickness of the cold-worked zone is in general agreement with previous work performed on the Pennsylvania Railroad [18]. In that study brass pins were placed in the head of new rail which was then installed in a track. After approximately ninety million gross tons of service, the flow of metal was found to extend from 5 mm to 10 mm (0.2 to 0.4 in) below the surface. The heavily worked zone was found to extend to a depth of 3 to 3.5 mm in a study of rail in the Soviet Union [19]. Similarly, the investigation into the cold-worked zone by the Office for Research and Experiments of the International Union of Railways has shown that the work hardening in European rail is large only up to a depth of 3 to 4 mm [20]. Some of the mechanical properties of the worked zone on Soviet rail have been given by Lempitskii, et al. [21].

Figure 8. Section Through the Top of the Used Rail Head (100 X, Nital Etch), Block [6]

Effect of the Cold-Worked Zone on Crack Growth

Growth rings of a typical transverse fracture of a rail also illustrate the presence of this cold-worked zone (Fig. 9). Here, a defect has been assumed to be located at the center of band number 1. Since the neutral axis during elastic action of the rail section is typically a few inches below the flaw growth area, one would expect higher stress magnitudes and, hence, faster flaw growth in the area above the origin. The effect of the compressive residual stresses resulting from the cold working in the upper layer is clearly illustrated by the fact that crack growth is arrested as it progresses toward the top of the rail. This arrested crack growth is also illustrated by the failed rail section shown in Fig. 10. A broken rail section similar to that shown in Fig. 10 has been observed, and the depth from the top of the rail to the top of the fatigue crack was measured to be 3.5 mm.

Texture of Cold-Worked Steel (Preferred Orientation)

Texture development during the cold-working process has been shown by many investigators to affect the ultrasonic wave propagation. This has been reviewed by Green [22]. Texture occurs in material when the grains develop a preferred rather than a random orientation. This can be caused by some external process such as cold working. Typically, steel plates and bars subjected to cold rolling processes

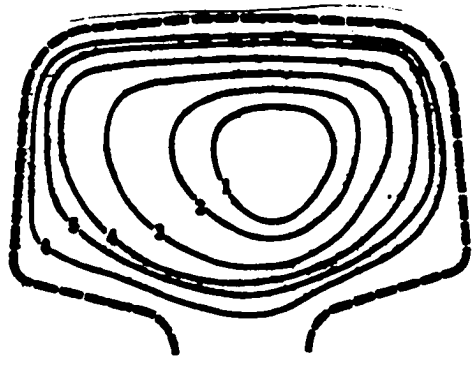

Figure 9. Growth Rings for Transverse Fracture in Rail (Courtesy Sperry Rail Service)

Figure 10. Transverse Fracture in Rail (Courtesy Sperry Rail Service)

develop a texture in which the {100} planes tend to orient themselves parallel to the plane of rolling, and the ⟨110⟩ directions approach within a few degrees of the direction of rolling [13,23]. These results have usually been obtained with low to medium carbon steels (0.08 to 0.35% C and 0.35 to 0.50% C, respectively).

Backofen reported work by Mathur which showed that the deformation texture is affected by the value of Δ and the amount of cold working [13]. The results were reported for drawn material, rather than rolled, but they are useful in this presentation. The intensity of X-ray reflections from (100) planes parallel to the surface was seen to increase in a nearly uniform manner as the amount of cold working was increased. This change in intensity for values of Δ ranging from one to four was grouped somewhat together. For the (110) planes, the intensity decreased with cold working. In this case, however the decrease was considerably less for higher values of $\Delta(\Delta = 4)$ than for lower values. Intensities from the (111) planes behaved in a different manner. For $\Delta = 1$, the intensity increased linearly throughout the test. For $\Delta = 2$, this peak occurred at approximately a fifty percent reduction, and for $\Delta = 4$, it occurred at approximately a thirty-five percent reduction. In each case the intensities for the (111) planes were lower for the higher values of Δ.

Using a rolling machine simulating railway conditions, Krause and Scholten have stated that the (135) plane tends

to orient itself parallel to the rolling plane with the [313] direction parallel to the direction of rolling [24, 25]. These results were obtained using a medium-carbon (C 0.45%) steel. Roller-hardened, medium-carbon steel has also been studied by Blanter, et al. [26]. Their interest, however, was only in the separation of the (110) and (220) planes for stress studies.

As shown in Table I, rail steel has a carbon content ranging from 0.67% to 0.80% for the 119 lb. section used in this study. It is well known that for the higher carbon steels, the propensity for the development of preferred orientation (i.e., texture) decreases [27]. Ravitskaya, however, stated that the worked layer of the rail head is textured, although no specific data were given [19]. There is an important relationship of ultrasonic wave propagation to texture. This relationship will be discussed later, and the texture of the rolled surface on the rail head will be investigated.

Wave Velocities and Isotropic Poisson's Ratios for New and Used Rail

Two new and five used rail samples were used for much of the laboratory work reported in Ref. [6]. In order to gain insight into the properties of the various rails, several wave velocities were measured. These are listed in

Table III. Rail eleven had been installed in the same main-line track section as rail seven. It also appeared to have been a low rail on a banked section of curved track. The history of the other used rail is unknown.

The dilatational wave velocity, A_2, and the shear wave velocity, B_2, were determined by placing an appropriate ultrasonic transducer at the end of the rail and near to the center of the head. The velocity of a dilatational wave propagating near to the surface of the rail (P wave) was obtained using a wedge where the incident angle could be varied from 0° to 90°. This is denoted as velocity A_1. The SV velocity, B_1, is the velocity of a critically refracted shear wave, also obtained with a variable angle wedge. The primary differences in each rail are seen to occur in the shear wave velocities B_1 and B_2. Velocity B_2 is lower than B_1 in all cases except for rails seven and eleven. In contrast, A_1 and A_2 are nearly the same in each case. All of the arriving pulses were quite strong, and the velocities were obtained using the first arrivals of each pulse.

The isotropic Poisson's ratios, ν_1 and ν_2, can be calculated for the upper surface and the body of the rail head, respectively. Poisson's ratio is given by :

$$\nu_i = \frac{\left(\frac{A_i}{B_i}\right)^2 - 2}{\left[2\left(\frac{A_i}{B_i}\right)^2 - 1\right]} \qquad (2.1)$$

Table III. Wave Velocities and Isotropic Poisson's Ratios for the Rail Head

Rail	A_1 m/s	B_1 m/s	A_2 m/s	B_2 m/s	ν_1	ν_2	B_2/B_1	A_2/A_1	Remarks
1	5878	3361	5879	3205	0.257	0.288	0.954	1.000	NEW
2	5868	3224	5854	3212	0.284	0.285	0.996	0.998	USED
6	5851	3243	5854	3177	0.278	0.291	0.980	1.000	USED
7	5872	3120	5868	3195	0.303	0.289	1.024	0.999	USED
8	5880	3375	5875	3202	0.254	0.289	0.949	0.999	NEW
10	5853	3217	5843	3205	0.284	0.285	0.996	0.998	USED
11	5890	3013	5855	3195	0.323	0.288	1.061	0.994	USED

where A_i and B_i are the respective dilatational and shear wave velocities. These results are also shown in Table III.

The uniformity of ν_2 in the range from 0.285 to 0.291 is readily observed. These are values typically used for steel. The range of ν_1 is not quite so uniform, however, going from 0.254 to 0.323. Even though the expected anisotropy of the worked layer is acknowledged, this range of ν_1 again indicates changes in material conditions at the surface of the rail. It should be noted that new rails one and eight show the lowest value for ν_1, while heavily worked rails seven and eleven show the greatest values.

Shear Wave Velocities and Critical Refraction Angles in the Cold-Worked Layer

The velocity of a shear wave (SV) propagating parallel to the rail surface along the length of the rail was discussed in the earlier report for new and used rail [6]. These waves were excited with a variable angle plastic wedge, and the angle of excitation was also recorded. A plot of the observed velocity and the sine of the excitation angle yield further useful observations about the cold-worked layer.

As indicated in Fig. 11, the reflection and refraction of ultrasonic waves is generally governed by Snell's law:

$$\frac{C_1}{\sin \theta_1} = \frac{C_2}{\sin \theta_2} \qquad (2.2)$$

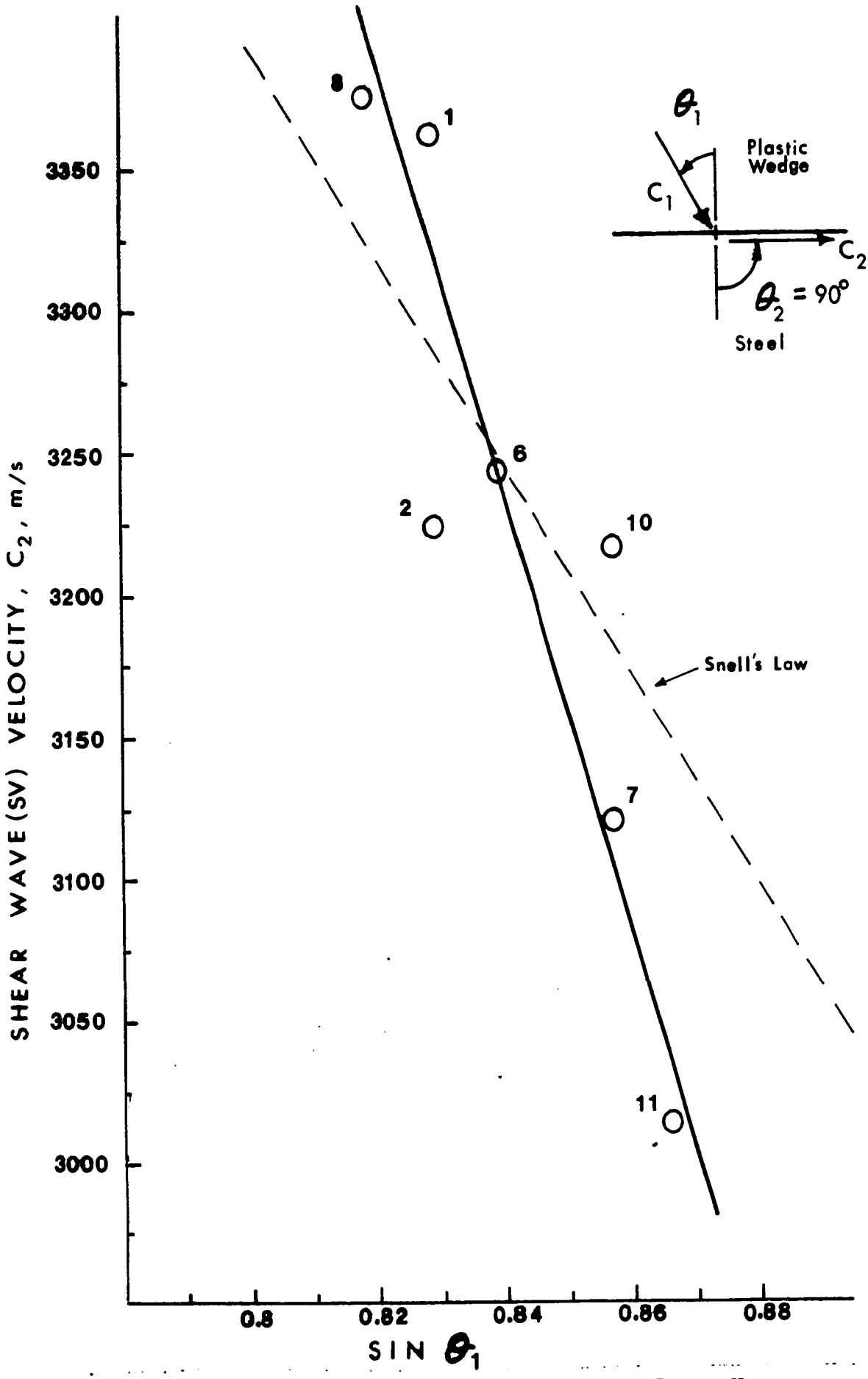

Figure 11. Shear Wave Velocity in Rail Top Layer Versus Sine of Excitation Angle in Plastic Wedge

Here, C_1 and C_2 are the wave velocities in the plastic wedge and the steel, respectively. Similarly, θ_1 and θ_2 are the incident and refracted angles of the beam. If θ_1 is the angle which excites the strongest SV pulse along the surface at $\theta_2 = 90^\circ$, the previous equation can be written simply as:

$$\sin \theta_1 = \frac{C_1}{C_2} \qquad (2.2a)$$

The dotted line is a plot of Eq. (2.2a) for a value of C_1 equal to 2730 m/s.

A plot of C_2 vs. $\sin \theta_1$, using values taken from Ref. [6], is shown by the circles in Fig. 11. As previously stated, rails one and eight are new, while the rest are used and have cold-worked layers on the upper surface. The decrease in the velocity of the SV wave near to the surface in used rail is clearly demonstrated.

The slope of the solid line drawn through the data is considerably different from the slope predicted by Snell's law. This behavior is most likely due to an anisotropic effect in the worked layer. Discussion to follow in Chapter IV will show that for anisotropic material the direction of energy flux can deviate from the direction of the wave normal [22]. Snell's law defines the relationship of the wave normal, and the data for θ_1 were obtained for maximum pulse energy.

The possibility exists that the variation in shear wave velocity in the upper portion of the head could account for some of the difficulty which occasionally occurs in the ultrasonic inspection of railroad rail [28, 29]. Conventional rail

flaw detectors excite a shear wave in the rail through a fixed plastic wedge or a liquid-filled wheel acting on the rail-head surface. The exact angle of incidence is fixed according to the desired refraction angle of the shear wave into the rail. Any number of fixed incident angles are possible, depending on the physical limitations of the carriage system. Shear wave refraction angles in the rail are usually in the range from 30° to 90°.

The likely effect of variations in shear wave (SV) velocity can be demonstrated with the extreme B_1 values from Table III. According to Ref. [29], the nominal 45° shear wave in the rail is excited with an incident angle of 35.8° in a plastic wedge. Using velocity B_1 for rails eight and eleven, it can be shown with Snell's law that at the 35.8° incident angle the refracted angle for those two rails will be 47.36° and 41.05°, respectively. However, since this beam quickly enters into the body of the rail head, a second refraction occurs because of the effect of velocity B_2. Using the angles just obtained as the new incident angles, and B_2 as the shear wave velocity in the body of the rail, it can be further shown that the entrance angles into the body of the rail are now approximately 44° for each rail. The result is not seriously different from the expected 45° angle.

Using the same analogy for the nominal 70° beam, the effect is shown to be larger. This beam would be excited with a 51° incident angle in the plastic wedge. For this

case, the immediate refraction angle would be 79.2° for rail eight and 61.3° for rail eleven. The change in the angle of the refracted wave could have a pronounced effect on the inspection, since at the higher refraction angle, this refracted beam would travel in the upper area of the rail during a large portion of its journey. Upon entering the body of the rail head, the refracted beam angles would be 68.9° for rail eight and 68.4° for rail eleven.

If a large number of probes at various angles near to 70° were used, the likelihood of not detecting a rail flaw because of this effect could be minimized. Since the head of a used rail is most likely highly anisotropic, it is felt that the overall effect on higher beam angles should be considered in designing rail flaw detection systems.

CHAPTER III

WAVE PROPAGATION IN THE COLD-WORKED LAYER

The previous study, which showed the presence of the "early arrivals" ahead of the surface wave, concentrated on the measurement of changes in the longitudinal rail stresses resulting from temperature fluctuations. Variations in Rayleigh wave velocities on the rail head, which were not entirely understood during that work, demonstrated that these waves could not be reliably used for that purpose. Data in that study were obtained mostly to demonstrate the Rayleigh wave velocities, and only brief attention was paid to the early arrivals. As a result, the data had not been closely analyzed to investigate the dispersion pattern for the early arrivals. Although the apparatus and techniques used for obtaining the data have been reported in Ref. [6], some of the information is repeated here for the sake of completeness.

The basic apparatus used for obtaining wave velocities in the head of full-sized rail is shown in the photograph in Fig. 1. The schematic is shown in Fig. 12. The pulse excitation circuit consisted of a modified Sperry UR Reflectoscope,

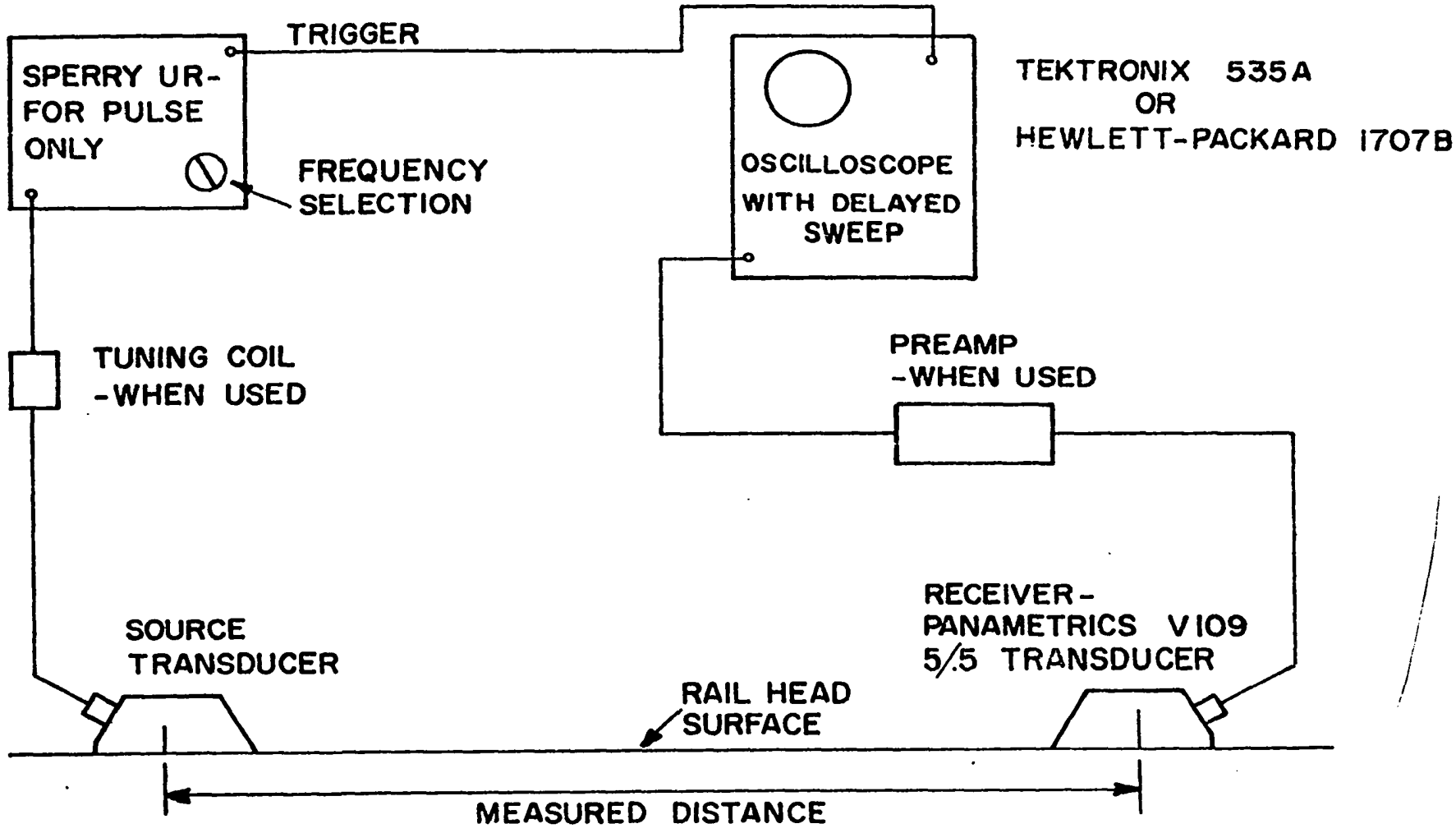

Figure 12. Schematic of Apparatus Used on Full-Sized Rail [6]

a separate probe tuning box and the source transducer. The primary transducer design was a 25.4 mm (1 in) square piezoelectric plate mounted on a plastic surface wave wedge as shown in Fig. 13. The lead-zirconate-titanate piezoelectric plates were made of HDT-31 material, purchased from Gulton Industries, and the plastic wedges were purchased from Comco. The incident beam angle was 64°. The piezoelectric plate was "air backed," i.e., it was not mounted with a highly damped backing material as is often the case. Some of the plates were bonded with epoxy to the plastic wedge. Most, however, were simply laid on a piece of thin aluminum foil. The acoustical coupling was provided by a layer of oil between the plate and the foil, and the foil and the plastic. A spring clamp held the plate in place and furnished the electrical connection. This mounting achieved a longer ringing time, which was desirable in this situation. With this design, the primary control of the excitation frequency was the thickness of the piezoelectric plate. Peak tuning was achieved by using either an appropriate internal tuning coil of the Reflectoscope or a separate external coil.

The receiving circuit, in most cases, consisted of a 12.7 mm (0.5 in) diameter Panametrics V109 transducer mounted on a plastic wedge identical to the one used at the sending transducer. This was a highly damped transducer having a very broad frequency response. When required, a pre-amplifier was used on the received signal. The signal was displayed on either a Tektronix Type 535A or a Hewlett-Packard 1707B

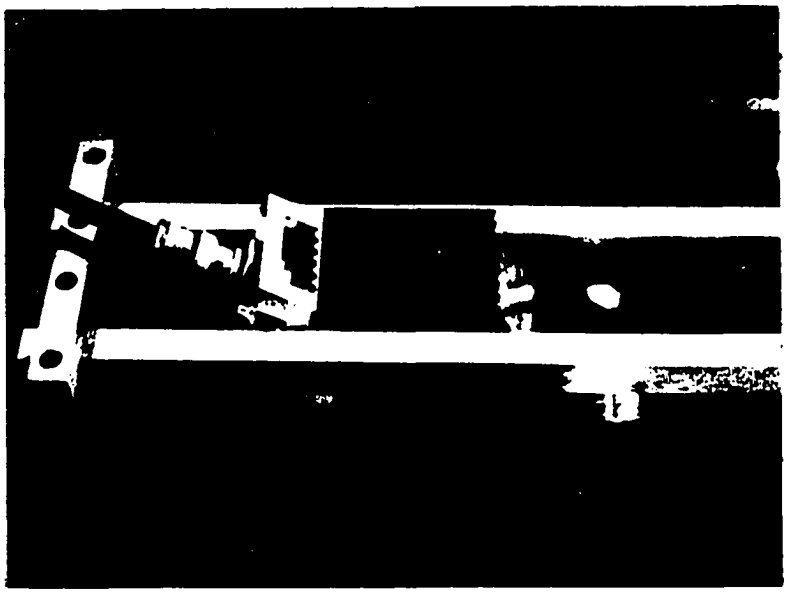

Figure 13. Probe and Guide Arrangement for Surface Wave Measurements [6]

oscilloscope, the oscilloscope trace being triggered by the source pulse of the Reflectoscope.

For the earlier study, wave transmission times were usually obtained by keeping the receiving transducer at a fixed location and situating the source transducer at six locations along the rail. These locations were 600 mm, 500 mm, 400 mm, 300 mm, 200mm, and 100 mm from the receiver. An aluminum distance and alignment frame was constructed with 100 mm increments inscribed thereon. This is not shown in Fig. 1, but it is partially shown in Fig. 13. A velocity averaging technique was used to obtain surface wave velocities in the previous study. This method was not used to obtain the velocities herein reported.

Since most of the data to be used in this study existed in the form of photographs, as shown in Figs. 2a and 3a, the required velocities were extracted directly from them. This sacrificed some accuracy, but the information obtained was still quite satisfactory. It was necessary to adopt this method of velocity determination in order that all data would be obtained in a similar manner. Appendix A furnishes more detail on the shape of the source pulse used in these experiments. The methodology used for determining the arrival times is described in Appendix B.

In the photographs shown in Figs. 2 and 3, the top and lower arrivals are those obtained at transducer spacings of 100 mm and 600 mm, respectively. In the top record, i.e, at

100 mm, the early arrival and the surface waves are indistinguishable. This was assumed to be the zero reference time. Travel times from the 100 mm to the 600 mm stations were obtained merely by using a scale and measuring the distance between the 100 mm arrival and those at 600 mm.

In order to minimize error, each photograph was placed on a drafting table, and the distances were carefully marked. Some error possibility exists in the photograph itself because of the space existing between the face of the cathode-ray tube showing the pulse arrivals and the graticule of the oscilloscope. Error could also occur in reading the distance with the scale. The combined error of the measurement was believed not to exceed ±1.5 μs, or approximately ±1% of the transmission time.

The distance of the transducer spacing was determined from the marks on the aluminum alignment frame, and these were believed to be accurate to one-half of a millimeter. For the 500 mm distance, this could represent a possible error of ±0.1%. As will be demonstrated later, this error did not seriously affect the results.

A summary of the travel times obtained from four of the used rail samples is shown in Table IV. The nominal frequency was obtained directly from the expanded pulse display, as shown in Fig. 3b for rail number seven. Dispersion was evident to some extent in all pulses which could induce some error in the value used for frequency. This was not

Table IV. Wave Arrival Times and Velocities

Rail No.	Freq. (MHz)	t_R (μs)	C_R (m/s)	t_S (μs)	C_S (m/s)
7	0.5	167	2994	-	-
	0.7	168	2976	-	-
	1.0	166	3012	148	3378
	1.7	168	2976	156	3205
	2.0	169	2958	157	3185
9	1.5	172	2906	156*	3205
	2.0	166	3012	150	3333
10	0.5	170	2941	-	-
	1.7	169	2958	151	3311
	2.0	166	3012	151	3311
11	0.5	169	2958	**	-
	0.7	168	2976	-	-
	1.0	168	2976	152	3289
	1.7	171	2924	160	3125
	2.0	170	2941	160	3125

* This arrival was followed by others at 160 μs and 171 μs besides the surface wave.

** A very faint arrival was noted at 155 μs.

felt to be significant, however. In each case, t_R is the travel time for the surface wave, and t_S is that of the early arrival. The values for C_R and C_S are the resulting velocities.

The original data were somewhat incomplete in that a full set of data for a wide range of frequencies had not been obtained. To supplement this, additional data at 0.7 MHz and 1.0 MHz were taken for rails seven and eleven.

The series of photographs shown in Fig. 14 demonstrate the behavior of the arrivals for several frequencies for rail eleven. Each trace shows the arrival at 600 mm and was cut from a separate photograph. The left end of each trace has been cut off at the zero time base established by the 100 mm arrival in the original photograph. The slightly wider spacing between the Rayleigh wave arrival and the early arrival is evident at 1.0 MHz when compared to the traces shown for both 1.7 MHz and 2.0 MHz. This difference in arrival time was estimated to be approximately 8 μs, as shown in Table IV.

The relative decrease in C_R with increasing frequency can be readily observed for rails seven and eleven. The values for C_S behave similarly. In the case of rails nine and ten, C_R can be seen to grow larger with increasing frequency. Although more discussion on this is to follow, the fact that B_2/B_1 in Table III is greater than one for rails seven and eleven and less than one for rail ten would indicate

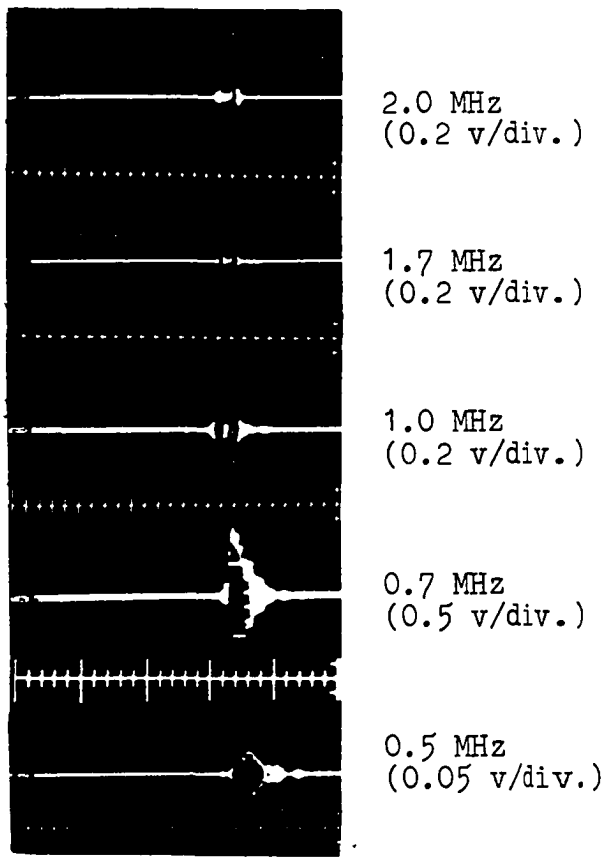

Figure 14. First Shear and Fundamental Rayleigh Mode Arrivals in Rail 11 at 0.5 MHz, 0.7 MHz, 1.0 MHz, 1.7 MHz, and 2.0 MHz, Time Base 50 μs/div. (Retouched Composite)

that the change in shear wave velocity through the rail section might be related to this observed behavior in the surface waves. Unfortunately, no shear wave data were obtained for rail nine.

The arrivals between t_S and t_R for the 1.5 MHz data for rail nine and the very weak early arrival at 0.5 MHz for rail eleven are most likely due to other modes which were not identified.

Wave Propagation in Layered Media

The discovery of seismic waves travelling in the earth's crust brought the attention of some of the more notable pioneers in wave propagation to bear on the problem of waves in layered media. First among these were Love [30] and Lamb [31]. Stoneley [32] and Sezawa [33] also made early and important contributions to the study of this problem. In more recent years, Tolstoy and Usdin [34] presented solutions to the equations of motion for a variety of layered combinations. Much of this early work has been reviewed by Ewing, Jardetzky and Press [35].

Large-scale usage of computers was a major event in the investigation of this very complex pattern of wave propagation. This permitted the solution of the equations of motion for a large number of material property combinations.

In the work reported in Ref. [6], the dependence of the early arriving wave upon the existence of the cold-worked

layer was felt to be quite conclusive. The exact identity of the wave and the material properties governing its appearance remained undetermined. An investigation into the possibility that they might be Stoneley waves showed that this was unlikely because of the particular set of material properties required for the existence of Stoneley waves. The conclusion that these were shear waves was reached in Ref. [6], but no proof was given.

The work which was of greatest importance in correctly identifying these early arrivals was that of Bolt and Butcher [36] and Mooney and Bolt [37, 38]. Using the work of Sezawa [33] as their source, Bolt and Butcher showed that solutions to the equations of motion for Rayleigh surface waves exist for a single surface layer when $k \geq 0$, $C < B_1 < B_2$ and $B_1 < C \leq B_2$. No restriction applies to A_1 or A_2 other than the requirement that Poisson's ratio must lie between 0 and 0.5. The parameters are defined as follows for the equations of motion and for the structure shown in Fig. 15:

$$k = \frac{\omega}{C}$$

C = phase velocity

$$A_i = \left[\frac{(\lambda_i + 2\mu_i)}{\rho_i}\right]^{\frac{1}{2}} = \text{dilatational wave velocity in layer i}$$

$$B_i = \left[\frac{\mu_i}{\rho_i}\right]^{\frac{1}{2}} = \text{shear wave (SV) velocity in layer i}$$

ρ_i = density in layer i

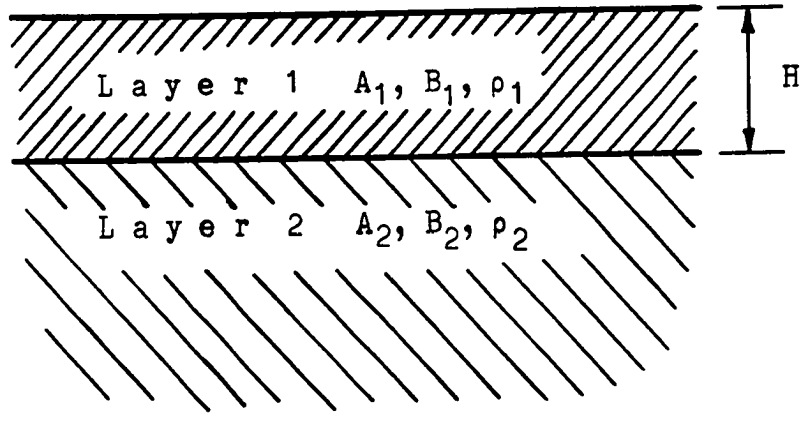

Figure 15. Structural Model for Layered Wave Propagation Studies

λ_i, μ_i = Lame' parameters in layer i

i = 1 for upper layer, = 2 for underlying structure

H = thickness of layer 1

The solution demands that the determinant defined by the following matrix elements must equal zero. Following the general definitions used by Bolt and Butcher, these elements are:

$$D(1,1) = T_1 Sr_1/(T_2)^{\frac{1}{2}} + T_1 Cr_1/(T_3)^{\frac{1}{2}} - 2(T_4)^{\frac{1}{2}} Ss_1 - 2Cs_1/(T_3)^{\frac{1}{2}}$$

$$D(1,2) = 2Cr_1 + 2(T_2)^{\frac{1}{2}} Sr_1/(T_3)^{\frac{1}{2}} - T_1 Cs_1 - T_1 Ss_1/\left[2(T_3)^{\frac{1}{2}}(T_4)^{\frac{1}{2}}\right]$$

$$D(1,3) = \left[(T_5)^{\frac{1}{2}}(T_3)^{\frac{1}{2}} - 1\right]/(T_3)^{\frac{1}{2}}$$

$$D(2,1) = 2\,T_1(1 - M)\,Cr_1 + \left[2M - 2 + P_1/E_1\right] Cs_1 \qquad (3.1)$$

$$D(2,2) = 4(T_2)^{\frac{1}{2}}(1 - M)Sr_1 + T_1(2M - 2 + P_1/E_1)Ss_1/(T_4)^{\frac{1}{2}}$$

$$D(2,3) = (MP_2)/E_2$$

$$D(3,1) = (T_1)^2 Sr_1/(T_2)^{\frac{1}{2}} + MT_1T_6Cr_1/(T_3)^{\frac{1}{2}} - 4$$
$$(T_4)^{\frac{1}{2}} Ss_1 - 2MT_6Cs_1/(T_3)^{\frac{1}{2}}$$

$$D(3,2) = 2T_1(Cr_1 - Cs_1) + 2MT_6(T_2)^{\frac{1}{2}} Sr_1/(T_3)^{\frac{1}{2}} -$$
$$MT_6T_1Ss_1/\left[(T_3)^{\frac{1}{2}}(T_4)^{\frac{1}{2}}\right]$$

$$D(3,3) = M\left[(T_5)^{\frac{1}{2}} - T_6/(T_3)^{\frac{1}{2}}\right] .$$

Computational and material parameters for this equation are defined as follows:

$$P_1 = C^2/A_1^2$$

$$P_2 = C^2/A_2^2$$

$$E_1 = B_1^2/A_1^2$$

$$E_2 = B_2^2/A_2^2$$

$$Cr_1 = \text{Cosh}[kH(1 - P_1)]$$

$$Sr_1 = \text{Sinh}\ [kH(1 - P_1)]$$

$$Cs_1 = \text{Cosh}[kH(1 - P_1/E_1)]$$

$$Ss_1 = \text{Sinh}[kH(1 - P_1/E_1)]$$

$$T_1 = 2 - P_1/E_1$$

$$T_2 = 1 - P_1$$

$$T_3 = 1 - P_2$$

$$T_4 = 1 - P_1/E_1$$

$$T_5 = 1 - P_2/E_2$$

$$T_6 = 2 - P_2/E_2$$

$$M = \mu_2/\mu_1 = (B_2^2\rho_2)/(B_1^2\rho_1) \quad .$$

As stated by Bolt and Butcher, the value of the determinant remains real for all of the previously defined conditions. Where $B_1 < C < B_2$, Cs_1 is real, but Ss_1 is imaginary. Since Ss_1 always occurs in the determinant in conjunction with $(T_4)^{\frac{1}{2}}$, and both expressions will be simultaneously imaginary when $C > B_1$, the result is a real value for the determinant for the whole range of conditions previously stated. A limiting case exists when $C = B_1$, which results in $T_4 = 0$.

There are several possible solutions to this determinant. Those of interest to this investigation are the fundamental Rayleigh mode and the first shear mode. The latter is often identified as the M_{21} or Sezawa mode.

It is clear from the foregoing that any pairing of two materials can be completely defined by the respective values for A_i, B_i and ρ_i. Solutions for C within the bounds previously given exist for a range of values for kH greater than zero. There is a minimum value of kH for the first

shear mode above which solutions of C exist for the equations of motion.

A Fortran IV computer program was written using the Newton-Raphson iteration process to find solutions for both modes for a full range of values for kH and C. Complex double precision computations were used. In order to start the iteration, initial solutions of C at small values of kH were required. For the fundamental mode, initial values of kH were 0.01 and 0.1, and in each case C was incremented in small values from a starting point of $0.9B_1$. The search for C was terminated when either the successive values of C were in agreement to seven significant figures or the value of the determinant became less than $(10)^{-3}$.

Once these two initial solutions were found, the Newton-Raphson process was activated to find a solution for C at succeedingly larger values of kH. For each iteration at a constant kH_n, the new value of C was determined by:

$$C_{m+1} = C_m - \frac{D_m}{\frac{\partial D}{\partial C_m}} \tag{3.2}$$

where C_{m+1} = new estimate of C

C_m = previous estimate of C

D_m = value of the determinant at C_m and kH_n

$$\frac{\partial D}{\partial C_m} = \frac{D_m - D_{m-1}}{C_m - C_{m-1}}$$

m = iteration integer = 1,2,3, . . .

n = root integer = 1,2,3, ...

The evaluation of D_m was performed in a subroutine separate from the main program. Iterations continued until successive values of C were in agreement to eight significant figures.

Group velocities were calculated by first writing the equation:

$$\frac{\partial D}{\partial C} dC + \frac{\partial D}{\partial kH} d(kH) = 0 \qquad (3.3)$$

This equation, as given by Mooney and Bolt [38], is merely the result of chain-rule differentiation of the original determinant for the equation of motion when written in the form:

$$D(C, kH) = 0 \qquad (3.4)$$

Eq. (3.3) can be rewritten as:

$$\frac{dC}{d(kH)} = - \frac{\left(\frac{\partial D}{\partial kH}\right) C}{\left(\frac{\partial D}{\partial C}\right)_{kH}} \qquad .(3.3a)$$

The evaluation of the partial derivatives was carried out in the following manner. For the numerator, D_j is the value of the determinant at the value of C_{m+1} just found to be a root at KH_n. The following parameters are defined:

$$C_j = C_{j-1} = C_{m+1} = C_n$$

$$kH_j = kH_n \qquad (3.5)$$

$$kH_{j-1} = kH_n - CKH$$

where CKH is a suitable decrementing constant. The numerator can now be written:

$$\left(\frac{\partial D}{\partial kH}\right)_C = \frac{D_j - D_{j-1}}{kH_j - kH_{j-1}} \qquad (3.6)$$

A similar procedure is followed for the denominator where

$$kH_k = kH_{k-1} = kH_n$$

$$C_k = C_{m+1}$$

$$C_{k-1} = C_{m+1} + CDT$$

and CDT is a suitable incrementing constant. The denominator in Eq. (3.3a) can now be written:

$$\left(\frac{\partial D}{\partial C}\right)_{kH} = \frac{D_k - D_{k-1}}{C_k - C_{k-1}} \qquad (3.7)$$

The usual expression for the group velocity (U) is

$$U = C + k\,\frac{dC}{dk} \qquad (3.8)$$

Multiplying the numerator and denominator of the derivative by the constant H yields

$$U = C + (kH)\frac{dC}{d(kH)} \tag{3.8a}$$

and substituting the expression from Eqs. (3-3a), (3.6) and (3.7) gives

$$U_n = C_n - (kH_n)\left[\frac{\dfrac{D_j - D_{j-1}}{kH_j - kH_{j-1}}}{\dfrac{D_k - D_{k-1}}{C_k - C_{k-1}}}\right] \tag{3.8b}$$

As noted by Mooney and Bolt [38], this method of computing the group velocity produces much greater accuracy in regions of rapid change in phase velocity, near the cutoff points of the higher modes and near the beginning and end of the range of computation. The uniformity of the change in group velocity can be greatly affected by the choices for CKH and CDT. These were determined by trial-and-error.

The results of a more recent investigation into the layered wave problem has been given by Munasinghe [39]. Using a finite difference formulation, he showed the results for an aluminum layer over fused quartz. Phase velocity curves for the fundamental Rayleigh mode and the first shear mode followed a form similar to those of Bolt and Butcher and Mooney and Bolt. Amplitude coefficients and energy transmission fractions were developed for the fundamental Rayleigh mode for the aluminum and quartz model.

Computation of Phase and Group Velocities for the Fundamental and First Shear Mode (Geophysical and Rail Models)

The first computational effort was to duplicate the results for one of the models of Mooney and Bolt [37,38]. For this, the values shown in Table V were used. These correspond to case 4487 in Ref. [37] and model 2 in Ref. [38]. Dispersion curves calculated for this model are shown in Fig. 16. Values for CKH and CDT used in calculating the group velocities for this model were 0.01 and 1.0, respectively.

Several notable characteristics exist for these dispersion curves. First, considering the fundamental mode, the ratio of phase velocity to the shear wave (SV) velocity, (C/B_1), in the upper layer is seen to approach 1.8388 for the lower frequencies, i.e., B_1T/H greater than ten. Here, B_1 and H are as previously defined and T is the period. This represents a value of C/B_2 of 0.9194, which corresponds to the velocity of Rayleigh waves which would be expected in medium two without the layer. As the frequency is increased and the wave length becomes shorter, C/B_1 approaches 0.9194 which corresponds to the expected Rayleigh wave velocity in a half-space having the properties of layer one. The group velocity curve is seen to have a minimum at $B_1T/H = 2.3$. This dispersion curve for the fundamental mode would also exist but would be inverted for the case $B_1 > B_2$.

Table V. Computational Parameters for Geophysical and Rail Models

	Mooney and Bolt Case 4487 [36]	Rail Number 7	7A	11	11A
A_1(m/s)	6235	5872	6255	5890	6134
B_1(m/s)	3600	3120	3185	3012	3125
ν_1	0.250	0.303	0.325	0.323	0.325
A_2(m/s)	12,471	5868	6319	5855	6153
B_2(m/s)	7200	3195	3378	3195	3289
ν_2	0.250	0.289	0.300	0.288	0.300
B_2/B_1	2.0	1.024	1.06	1.061	1.052
A_2/A_1	2.0	0.9993	1.01	0.994	1.003
ρ_2/ρ_1	1.5	1.0	1.0	1.0	1.0

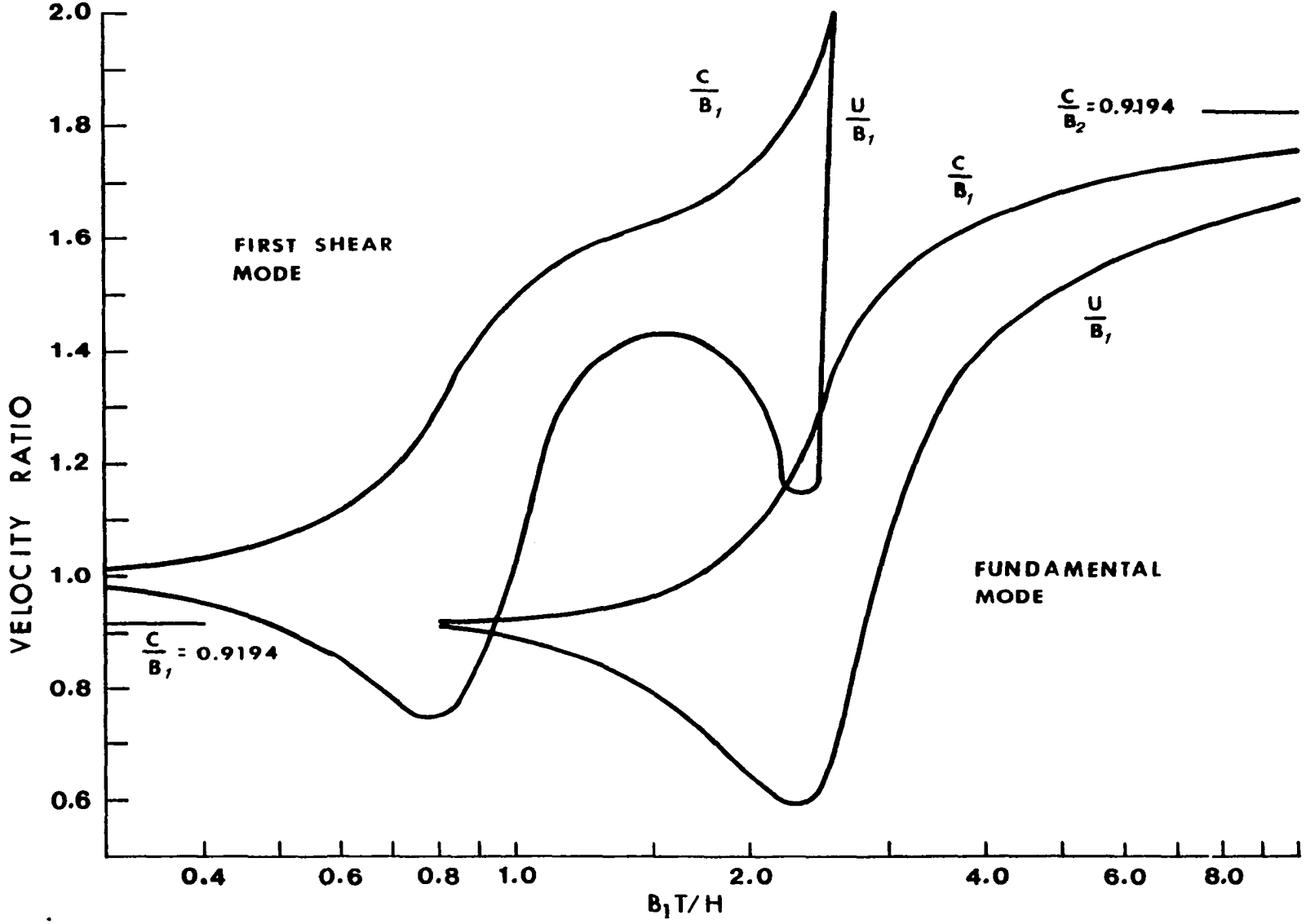

Figure 16. Phase and Group Velocities for Fundamental Rayleigh and First Shear Modes for Geophysical Model

There is a "cutoff" level shown for the first shear mode. For B_1T/H greater than a certain value, no energy propagates in this mode. This "cutoff" is established for the value of B_1T/H which gives a value of C/B_1 equal to B_2/B_1. That is to say that no shear wave energy can propagate in this first mode at a velocity higher than B_2. An analysis of Snell's law for shear waves reflecting at the interface can demonstrate the correctness of this behavior. As the frequency of the pulse is increased, and consequently B_1T/H is decreased, the phase velocity for the indicated curve decreases until it approaches $C/B_1 = 1$ in the limit. The phase velocity curve is seen to have several changes in slope which result in a group velocity curve having two minima and one maximum between the limits. The first minimum occurs slightly below the cutoff, and the second near to $B_1T/H = 0.8$. The maximum occurs near to $B_1T/H = 1.55$.

The dispersion patterns shown by these curves and the exact numerical values obtained with this program showed precise agreement with the results of Mooney and Bolt [37,38]. From the appearance of these two curves one can easily associate the fundamental and first shear modes with the behavior of the surface waves and the early arrivals seen in the case of the used rail.

An analysis of particle displacements at different depths and wave lengths can aid in the further understanding of the behavior of these two waves. Kanai has calculated

these displacements in a continuation of the investigations of Sezawa [40]. Kanai's model assumed elastic constants which yield $A_2/A_1 = B_2/B_1 = 2.83$ and $\rho_2/\rho_1 = 1$. Figure 17 shows an approximate representation of the displacements calculated by Kanai at a wave-length-to-thickness ratio corresponding to $B_1T/H \approx 2.5$. In this figure, u and v represent horizontal and vertical displacements, respectively. The solid lines show the fundamental Rayleigh mode while the dashed lines show the first shear (Sezawa) mode.

At approximately one-half the layer depth, the horizontal displacement of the first shear mode is at a maximum and nearly nine times greater than the corresponding horizontal displacement of the fundamental Rayleigh mode. These displacements are in phase. The vertical displacements behave differently. Not only are they in opposing phase, the displacement of the fundamental Rayleigh mode is nearly five times as large as that of the first shear mode.

At the boundary, the displacements of the fundamental Rayleigh mode are quite small. For the first shear mode, the horizontal displacement is less than at the surface but still four times as great as the horizontal displacement of the fundamental Rayleigh mode. They are still in phase. The vertical displacement of the first shear mode reaches a maximum just above the boundary, is out of phase with the vertical displacement of the fundamental Rayleigh mode and is approximately eight times greater in magnitude. Below

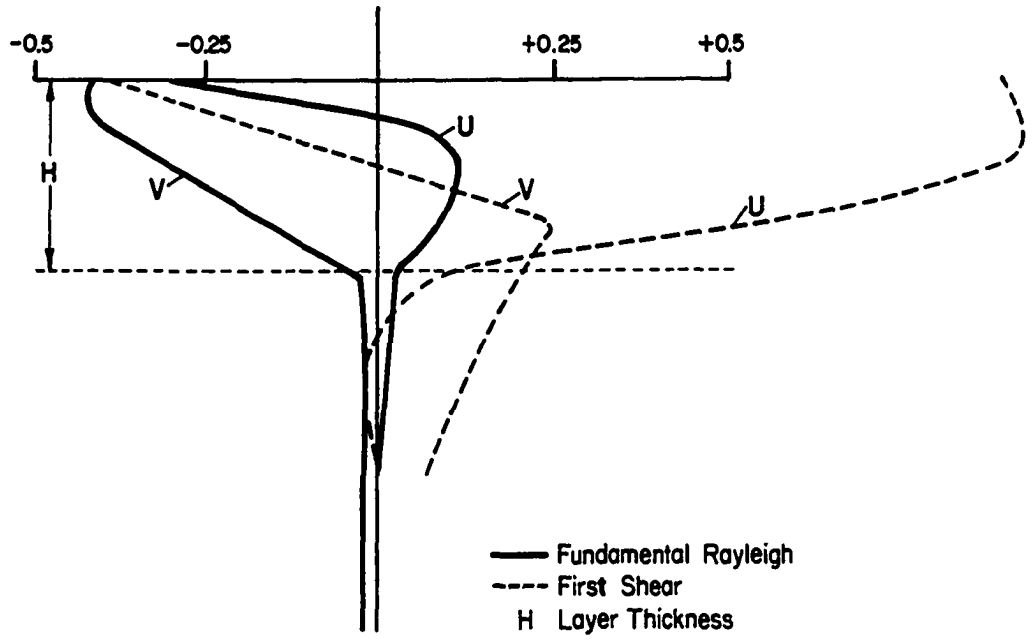

Figure 17. Displacements for the Fundamental Rayleigh and First Shear (Sezawa) Modes for $B_1T/H = 2.5$ [40]

the boundary, the amplitudes become quite small for all displacements except the vertical component of the first shear mode.

Although no discussion is given in Ref. [40] for shorter wave lengths, it seems reasonable to assume that the displacements of the fundamental Rayleigh mode become nearly independent of the underlying structure as the wave length is decreased further. The displacements of the first shear mode at shorter wave lengths were illustrated in an earlier paper [41]. They become less affected by the underlying structure but never completely free from its effects.

For the first attempt at correlating the observed surface wave arrivals in the rail with the behavior predicted by the analysis of Mooney and Bolt, values for A_1, B_1, A_2, B_2 and ρ_2/ρ_1 shown in Table V were assumed for rails seven and eleven. The density ratio was measured and reported in Ref. [6] to be near to 1.0 which is consistent with the statement by Deiter that cold working of metals decreases the density on the order of 0.1% [23]. The curves shown in Figs. 18a and 18b are the predicted dispersion curves based on these assumed velocity and density values.

The very low ratios of B_2/B_1 for the rails, as compared to that of the geophysical model, should be noted, since the range of solutions is very greatly affected by this ratio. For the geophysical case, the range of velocity ratios, from the minimum group velocity point for the fundamental to the cutoff point for the first shear mode, is approximately

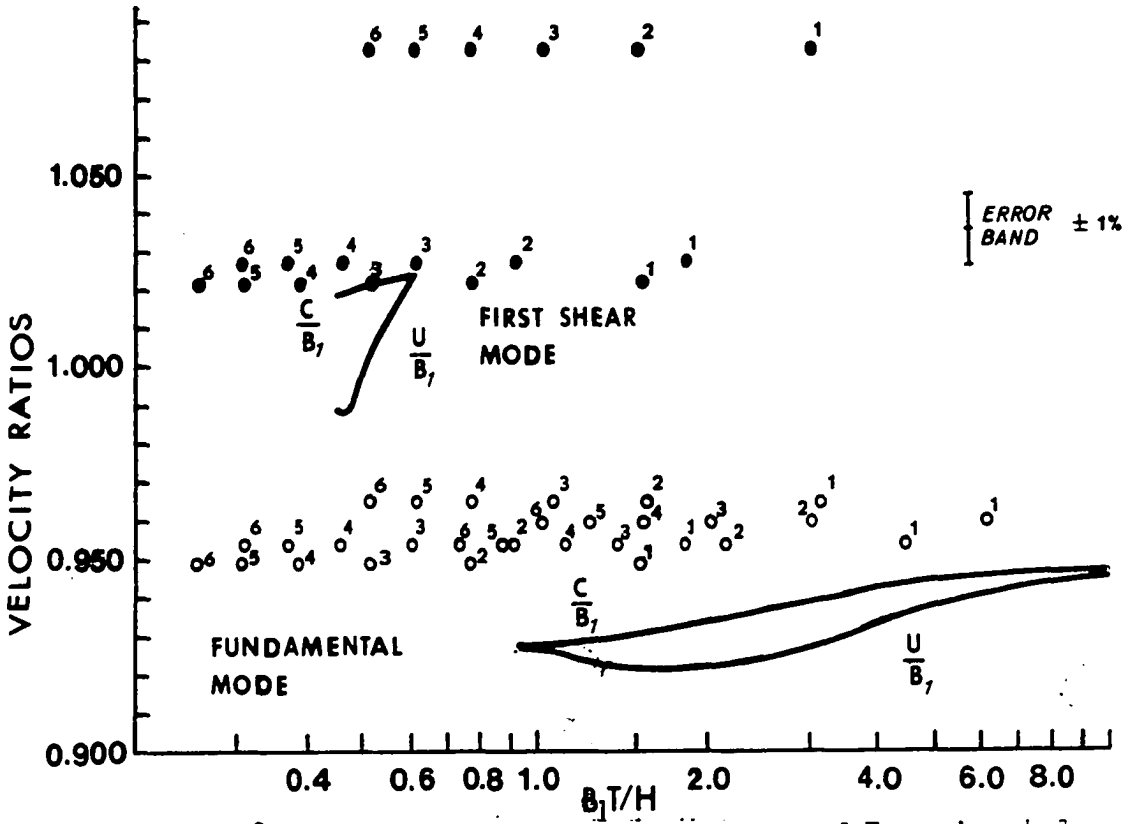

Figure 18a. Phase and Group Velocities and Experimental Data for Rail Seven

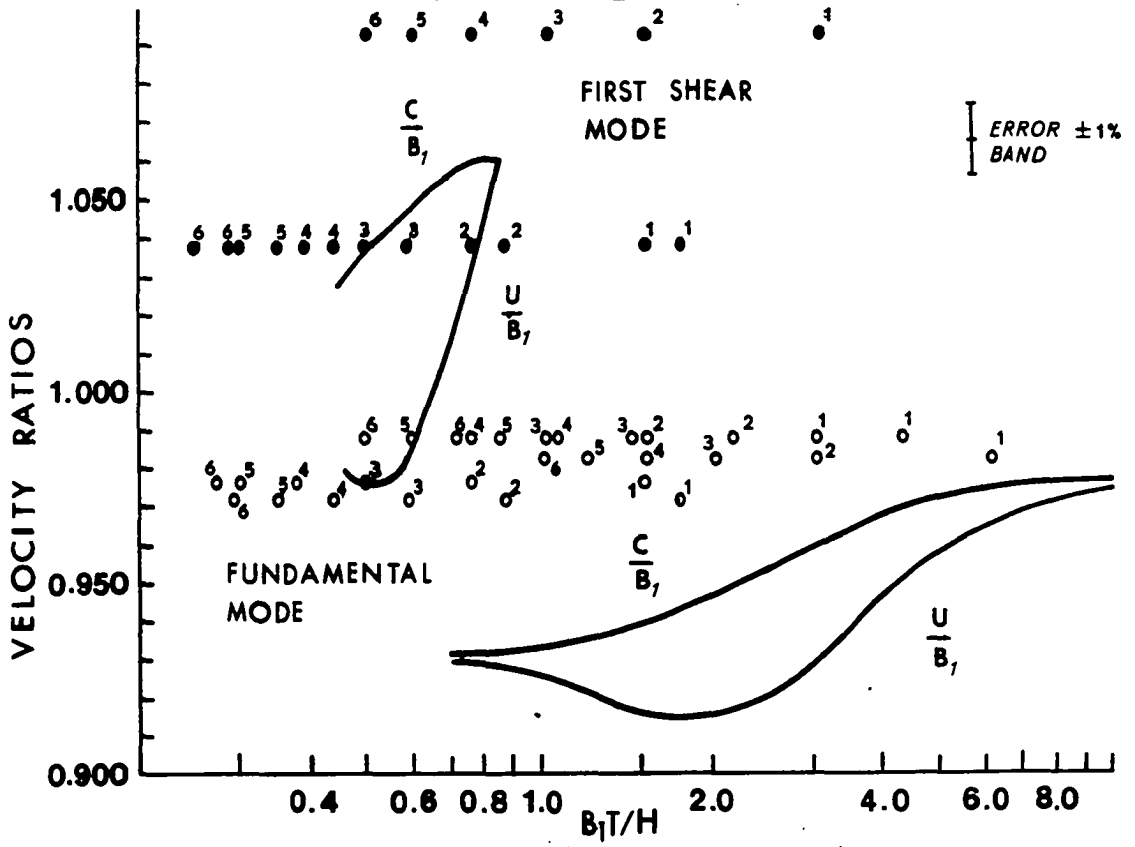

Figure 18b. Phase and Group Velocities and Experimental Data for Rail Eleven

1.4. The range is considerably less in the rail case, namely 0.146, or about one-tenth of the geophysical range. This caused some computational difficulty which was partly overcome by using incrementing and decrementing values that were different from those used for the geophysical model. Even with these modifications a full solution of the first shear mode toward lower values of B_1T/H was not obtained. This does not seriously affect the results of the investigation.

The experimental data previously given in Table IV have been converted to velocity ratios C_R/B_1 and C_S/B_1 for rails seven and eleven and are shown in Table VI. In order to plot these data versus the parameter B_1T/H, as shown on the graphs in Figs. 18a and 18b, a layer thickness, H, must be assumed. The velocity, B_1, and the period, T, are available from the data. Estimates of the depth of the worked zone on the rail head range from 1.5 mm to 10 mm or greater. Most of the estimates tend to be concentrated in the range from 3 to 5 mm. Table VI lists B_1T/H calculated for the B_1 and frequency values from Tables V and IV, respectively, and a range of layer thicknesses from 1 mm to 6 mm.

Open circles shown in Figs. 18a and 18b are experimental data for the fundamental mode, and the solid circles are experimental data for the early arrival. The small number near each circle represents the assumed layer thickness in millimeters for that point. For a particular frequency, values for C_R/B_1, C_S/B_1, and B_1T/H are obtained from Table VI. Using 1.0 MHz and rail seven as an example, Table VI lists values of

Table VI. $\frac{B_1T}{H}$, $\frac{C_R}{B_1}$, and $\frac{C_S}{B_1}$ for Rails Seven and Eleven

Rail 7 $B_1 = 3120$ m/s

Freq. (MHz)	$\frac{B_1T}{H}$ Layer Thickness (mm)						$\frac{C_R}{B_1}$	$\frac{C_S}{B_1}$
	1	2	3	4	5	6		
0.5	6.24	3.12	2.08	1.56	1.25	1.04	0.960	-
0.7	4.46	2.23	1.48	1.11	0.89	0.74	0.954	-
1.0	3.12	1.56	1.04	0.78	0.62	0.52	0.965	1.083
1.7	1.84	0.92	0.61	0.46	0.37	0.31	0.954	1.027
2.0	1.56	0.78	0.52	0.39	0.31	0.26	0.948	1.021

Rail 11 $B_1 = 3012$ m/s

Freq. (MHz)	$\frac{B_1T}{H}$ Layer Thickness (mm)						$\frac{C_R}{B_1}$	$\frac{C_S}{B_1}$
	1	2	3	4	5	6		
0.5	6.04	3.02	2.01	1.51	1.21	1.01	0.982	**
0.7	4.31	2.16	1.44	1.08	0.86	0.72	0.988	--
1.0	3.02	1.51	1.01	0.76	0.60	0.50	0.988	1.092
1.7	1.77	0.88	0.59	0.44	0.35	0.29	0.971	1.038
2.0	1.51	0.76	0.50	0.38	0.30	0.25	0.976	1.038

** A very faint arrival was noted at 155 μs.

B_1T/H ranging from 3.12 for an assumed H of 1 mm to 0.52 for H = 6 mm. Each frequency was plotted in this manner for both rails. The error band (±1%) was described earlier in this chapter.

In all cases, the observed data fall considerably above the predicted values for both rails. It appears that some agreement could be attained if the predicted values for the fundamental and first shear mode could be merely shifted upward by the same amount. The slopes of lines which could be drawn through the points for the assumed layer thickness seem to be in general agreement with the slopes of the predicted velocity changes.

A closer evaluation of the compatibility of the strict geophysical velocity definitions and the real case for the rail, and further use of the discussion of Mooney and Bolt [38], gave hints as to where adjustments could be made to the assumed values that would bring the predicted values more in line with the experimental data. Parameters A_1, B_1, A_2 and B_2 in the geophysical case were assumed to be uniform in their particular structure and to be truly "bulk" velocities. In the rail case, A_1 and B_1 are unlikely to be true bulk velocities since their wave lengths are not short compared to the assumed range of layer thickness. Ref. [6] gives nominal wave lengths of 4.7 mm and 2.4 mm for these values of A_1 and B_1, respectively. Because of wave-guide effects, one could expect the true bulk value of A_1 to be considerably greater than the

value which has been used here. The same could be said for B_1, although not to the same extent because of its shorter wave length. An increase in B_1 would have the double benefit of raising the predicted curves and lowering the velocity ratios for the experimental data.

The values for A_2 and B_2 were obtained at the center of the rail head. It might be reasonable to expect that the values of A_2 and B_2 just below the worked zone could be different from those obtained near to the center. This would be consistent with the changes in yield point and ultimate stress values found through the rail cross section by the researchers at the ORE [20].

Several variations of the velocities were used in an attempt to bring about closer agreement. The best fit was obtained by concentrating on the behavior of the first shear mode. As previously discussed for the geophysical case, the velocity of this wave would be expected to range from being equal to B_2 at the cutoff point and equal to B_1 at very high frequencies. Therefore, B_1 for each rail was assumed to be the observed velocity at the highest frequency used, namely 2.0 MHz. Similarly, B_2 was assumed to be the observed velocity at the lowest frequency where the early arrival was detected. These values were taken from Table IV and are listed for rails 7A and 11A in Table V. The new ratios of B_2/B_1 are not greatly different from the original values.

The remaining values to be estimated are A_1 and A_2. Since A_i and B_i are related to the isotropic Poisson's ratio, ν_i, as given by Eq. (2.3), several models were constructed based on assumed values of ν_i. The original data showed calculated values of ν_1 to be considerably higher than ν_2 for both rails seven and eleven. The technical literature generally gives a range of 0.283 to 0.300 for acceptable values of Poisson's ratio for isotropic steel [42,43]. Bradfield has shown that ν in cold-worked metal can be higher than in the isotropic case due to a significant decrease in the rigidity modulus [44]. The bulk modulus he notes is not measurably changed by cold-working.

The best agreements between experimental and predicted results in this study were obtained by using assumed values of $\nu_1 = 0.325$ and $\nu_2 = 0.300$. With these, new values for A_1 and A_2 are 6255 m/s and 6319 m/s for rail seven and 6134 m/s and 6153 m/s for rail eleven. In both cases A_2/A_1 is greater than one but still near to the ratios obtained from the original data. As noted by Mooney and Bolt, changes in A_1 and, hence, ν_1, have a very great effect on the results while changes in A_2 affect the results only slightly [38].

The parameters C_R/B_1, C_S/B_1 and B_1T/H must be recalculated for these new values of B_1. They are listed in Table VII.

Plots of the computer results for models 7A and 11A are shown in Figs. 19a and 19b. Also shown are the experimental

Table VII. $\frac{B_1T}{H}$, $\frac{C_R}{B_1}$, and $\frac{C_S}{B_1}$ for New Values of B_1

Rail 7A $B_1 = 3185$ m/s

$\frac{B_1T}{H}$

Freq. (MHz)	Layer Thickness (mm)						$\frac{C_R}{B_1}$	$\frac{C_S}{B_1}$
	1	2	3	4	5	6		
0.5	6.37	3.18	2.12	1.59	1.27	1.06	0.940	--
0.7	4.55	2.27	1.52	1.14	0.91	0.76	0.934	--
1.0	3.18	1.59	1.06	0.80	0.64	0.53	0.946	1.060
1.7	1.87	0.94	0.62	0.47	0.37	0.31	0.934	1.006
2.0	1.59	0.80	0.53	0.40	0.32	0.27	0.929	1.000

Rail 11A $B_1 = 3125$ m/s

$\frac{B_1T}{H}$

Freq. (MHz)	Layer Thickness (mm)						$\frac{C_R}{B_1}$	$\frac{C_S}{B_1}$
	1	2	3	4	5	6		
0.5	6.25	3.12	2.08	1.56	1.25	1.04	0.946	**
0.7	4.46	2.20	1.49	1.12	0.89	0.74	0.952	--
1.0	3.13	1.56	1.04	0.78	0.63	0.52	0.952	1.05
1.7	1.84	0.92	0.61	0.46	0.37	0.31	0.936	1.000
2.0	1.56	0.78	0.52	0.39	0.31	0.26	0.941	1.000

** See note, Table IV.

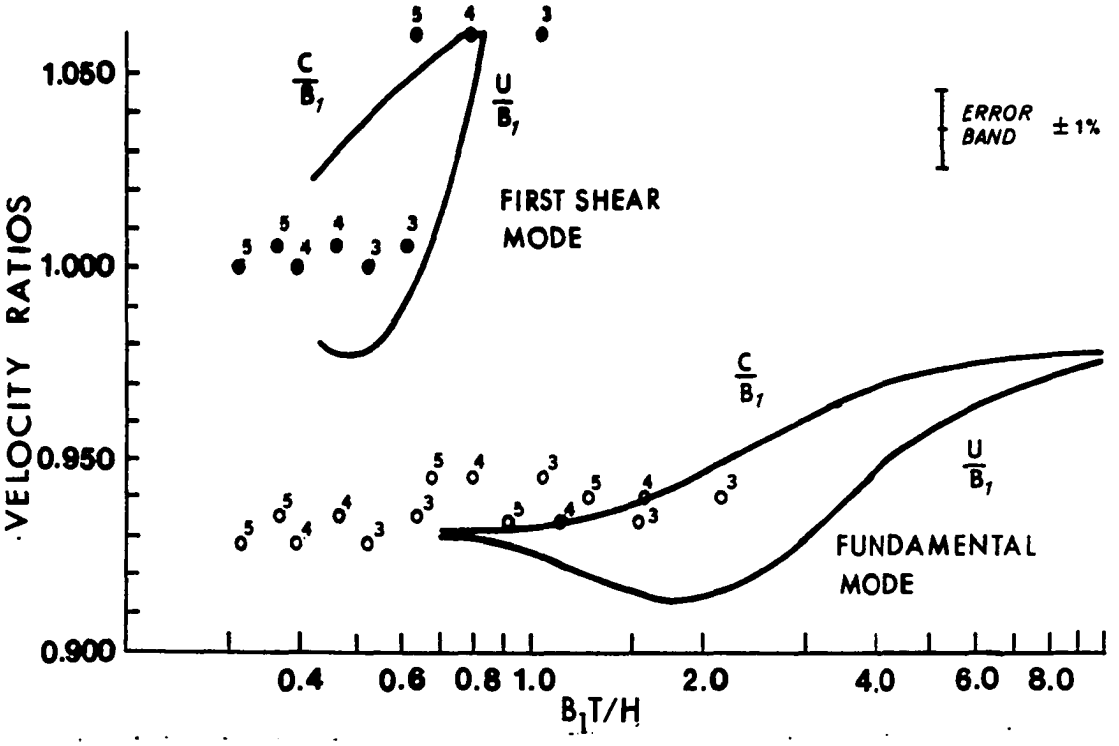

Figure 19a. Phase and Group Velocities and Experimental Data for Rail Model 7A

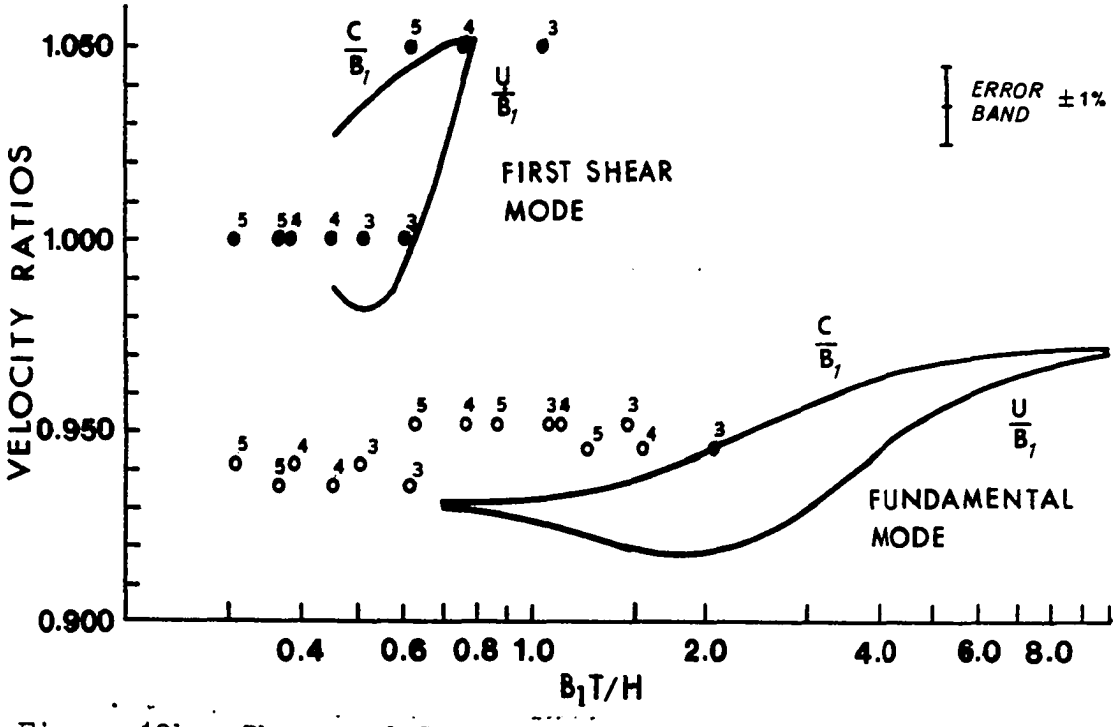

Figure 19b. Phase and Group Velocities and Experimental Data for Rail Model 11A

values obtained for C_R/B_1 and C_S/B_1, based on the new assumed value of B_1. Only experimental values for layer thicknesses of 3 mm, 4 mm, and 5 mm are shown in these figures.

In both models 7A and 11A, the early arrivals for an assumed 4-mm layer thickness are seen to be in good general agreement with the predicted velocity ratios. The lowest frequency arrival that would be expected from a 3-mm thickness falls somewhat above the cutoff value for B_1T/H but still in the general area. The lowest frequency arrival that would be expected from a 5-mm layer is near to the predicted phase velocity curve for the first shear mode. The highest frequency arrivals for a 5-mm layer fall close to the expected phase velocity curve while the 3-mm points are nearer to the group velocity curve. Considering experimental error, a layer in the range of 3-5 mm would produce results quite agreeable with the predicted velocity ratios. This discussion regarding the first shear mode is equally valid for either model 7A or 11A.

Some slight differences exist in the fundamental mode patterns for the two rail models. With the exception of one point, the experimental data for either a 3-mm or 4-mm layer produce a very good fit to the phase velocity curve predicted for model 7A. The lower error limit for the outlying points is very close to the predicted phase velocity curve so that no contradiction appears to exist. This data

point was in the supplemental set obtained almost eighteen months after the original data, and this could account for part of the error. Most of the fundamental mode data for rail eleven fall above the predicted velocity curves. A 3-mm layer appears to provide the best fit. The slope of a line drawn approximately through the experimental velocity data for the fundamental mode in both models is reasonably consistent with the slope of the predicted velocity change.

These slight disagreements between observed and predicted velocities for the fundamental Rayleigh mode could derive from several sources. First, the assumed value of B_1 is possibly still lower than it is in the true case. There is also the possibility that the assumed values for A_1 and B_2 are not strictly correct. These disagreements do not present a contradiction to the method of analysis but, rather, suggest that the true wave velocity values in the upper layer are still higher than the assumed values.

An additional error source could be the assumption of a well defined boundary between the upper layer and the underlying structure. Previous discussion relative to particle displacements has shown that the first shear mode remains affected by the underlying structure even at high frequencies. If the property changes take place over a finite thickness, say a half of a millimeter or greater, then the effect on the first shear mode would be different than for the abrupt, discontinuous change assumed by the geophysical

model. Thus, the choice of B_2 used in the model might not exactly agree with the one required to obtain a more proper fit for the fundamental Rayleigh mode.

It is interesting to note that the slopes of the experimental data calculated for the fundamental Rayleigh mode at fixed layer thicknesses appear to be increasing for larger thicknesses. The relationship of these slopes and the layer thicknesses can be demonstrated by visualizing two lines drawn through two of the 1-mm and 6-mm data points shown in Fig. 18b. The slopes of these two lines may be expressed as

$$\text{Slope}_{H=1mm} = \left[\frac{\left(\frac{C}{B_1}\right)_{0.5MHz} - \left(\frac{C}{B_1}\right)_{2.0MHz}}{\left(\frac{B_1T}{H}\right)_{0.5MHz} - \left(\frac{B_1T}{H}\right)_{2.0MHz}} \right]_{H=1mm}$$

and (3.9)

$$\text{Slope}_{H=6mm} = \left[\frac{\left(\frac{C}{B_1}\right)_{0.5MHz} - \left(\frac{C}{B_1}\right)_{2.0MHz}}{\left(\frac{B_1T}{H}\right)_{0.5MHz} - \left(\frac{B_1T}{H}\right)_{2.0MHz}} \right]_{H=6mm} .$$

Using values from Table VI, the ratio of these slopes is:

$$\frac{\text{Slope}(H=6\text{ mm})}{\text{Slope}(H=1\text{ mm})} = \frac{6.04 - 1.51}{1.01 - 0.25} = 5.96 \quad . \quad (3.10)$$

Thus, the ratio of the slopes of the lines is approximately equal to the ratios of the thicknesses.

The predicted values are based on the dimensionless parameter B_1T/H which can also be written λ/H. Since actual values of H do not enter into the solution of the wave equation, the fit of the slope of the predicted values and the slope of the actual data appear to have a significant meaning. The slopes of assumed 3 mm - 4 mm thicknesses show a very good fit to that of the phase velocity curve.

Fundamental Rayleigh wave velocities are dominated at high frequencies by the value of B_1. One of the more important observations of this chapter is the reasonably good agreement obtained between the experimental and predicted velocities of this fundamental mode at high frequencies when the assumed value of B_1 is taken from the velocity data of the highest frequency early arrivals.

No attempt was made in the previous discussion to correlate the observed arrivals with group velocity curves as distinguished from phase velocity curves. The number of data points was too limited, and the frequency determination was too imprecise to permit this distinction to be made to any significant degree. Dispersive pulses are normally considered to propagate according to the group velocity. However, pulse trains containing many oscillations of nearly constant period may be observed at arrival times more closely correlated with the phase velocity. The method used for determining

the arrival times largely determines whether the phase velocity or the group velocity is measured. Brune, Nafe and Oliver have proposed a technique for determining the phase velocity in dispersive pulses [45]. In order to apply this, wave forms must be obtained at closely spaced stations so that the dispersion can be continuously observed.

Excellent agreement between observed Rayleigh wave arrivals and the predicted group velocities have been obtained for a layered structure by Gregson [46]. In this experiment, a 0.3-inch (7.62 mm) copper layer was attached to a 6-inch radius (152.4 mm) steel sphere by an electroforming process. Pulses were generated by an impacting ball bearing swinging on a string. The resulting pulses were of the broad-band type and, therefore, highly dispersive. Group velocity curves similar in shape to those shown in Figs. 16, 18 and 19 were calculated for the model. The velocity minimum predicted for a wave-length-to-layer thickness ratio slightly less than two was very clearly shown in their data. Data at other wave-length-to-layer thickness ratios also fitted quite well with their group velocity curve. The higher order shear modes were not seen in their experiment.

It would be of interest to further investigate the propagation characteristics of the pulses used in obtaining the rail data. Since the primary concern of this analysis was to correctly identify the early arrival, further work to distinguish between group and phase velocities was considered to be beyond the scope of the present investigation.

Summary and Conclusion

The primary conclusion of this chapter is that the identity of and the properties affecting the observed early arrival in used rail have been definitely established. Assuming that cold working of the upper layer of the rail is a gradual process with time, and that the shear wave (SV) velocity is affected by this cold working, one should be able to predict the appearance of this first shear mode. This should occur when the ratio of B_2/B_1 approaches a value of 1.05 to 1.06 for a work-hardened layer thickness of 3 to 5 mm. In the next chapter, the cause for this velocity change in the upper layer will be discussed.

CHAPTER IV

WAVE VELOCITY CHANGES IN COLD-WORKED MATERIAL

Wave velocities are usually considered to be constant in any given material, and this assumption is adequate for most situations. A material which has the same velocity for a particular wave type in any direction is isotropic with respect to wave propagation.

Two particular exceptions to the isotropic assumption occur when a material is stressed or mechanically worked. Stresses may result from the application of an external force field. In this case, the wave speeds may change with the application of the external force but, in general, will return to the original value if the elastic limit is not exceeded. This relationship of applied stress and wave speed change is known as the acoustoelastic effect and has been discussed by numerous authors. A review of recent work in this field has been given in Ref. [6]. The acoustoelastic and third order elastic constants for rail steel have been given in Ref.[47].

Mechanically working a material may affect the wave velocities in several ways. Two of the primary ways are through changes in the residual stress and texture patterns. Residual stresses may be developed in the working process which can cause the wave velocities to vary according to the acoustoelastic effect. Also, material texture (preferred orientation) may occur in the material, and this can also cause wave velocity changes. A combination of these two effects may occur. The remainder of this chapter will show the possible effects of both residual stress and preferred orientation.

Effect of Residual Stress on Velocity Change in the Cold-Worked Layer

Figure 5 shows the change in the longitudinal residual stress through the section of a used, work-hardened rail [11]. The maximum stress differential occurs in a depth range of 8 mm to 20 mm and upwards toward the top of the rail. In the 8 mm to 20 mm area, the stress is shown to be tensile and measuring approximately 40 MN/m^2(5.8 ksi). The stress change is nearly linear from 10 mm to the top surface, where it was measured to be -160 MN/m^2(-23.2 ksi). The resulting total stress change would be -200 MN/m^2(29.0 ksi). The equivalent strain difference (ϵ) between these two locations can be

calculated. This is

$$\epsilon = \frac{-200\ \mathrm{MN/m^2}}{200{,}000\ \mathrm{MN/m^2}} = -1000\ \mu\mathrm{m/m} \qquad (4.1)$$

where 200,000 MN/m^2 ($29(10)^6$ psi) is Young's modulus for rail steel as given by Ref. [20]. This calculation has assumed that Young's modulus is constant through the material. Although this is known to be incorrect, the induced error is not significant for this argument [44].

For the above strain, the wave velocity changes can be predicted for both the dilatational and the vertical shear (SV) waves when propagating along the rail axis [47]. The value of $\Delta C/C^o$ for a dilatational wave at 1000 $\mu m/m$ is $2.459(10)^{-3}$. For the vertical shear (SV) wave, $\Delta C/C^o$ would be $0.35(10)^{-3}$. Here, ΔC is the wave velocity change, and C^o is the original value.

If the values of A_2 and B_2 obtained at the middle of the rail head are compared to the expected velocities in the upper layer caused by residual stress (shown as A_1' and B_1'), the following values result

$$\frac{A_2}{A_1'} = \frac{1}{(1. + 2.45(10)^{-3})} = 0.9976 \qquad (4.2)$$

$$\frac{B_2}{B_1'} = \frac{1}{(1. + 0.35(10)^{-3})} = 0.9996 \qquad (4.3)$$

A comparison of these ratios with those shown in Table V for the original and modeled values for both rails seven and eleven shows that A_2/A_1' is not greatly different from A_2/A_1 for either rail. Thus, residual stress cannot be dismissed at this point as a contributor to the change in velocity of the dilatational wave. The shear wave velocity ratios, on the other hand, are higher than the ratio B_2/B_1' by nearly five percent for both the actual values and the modeled values. Moreover, the residual stress effect indicates an increase in the shear wave velocity in the upper layer, which is opposite to the observed occurrence. Since a B_2/B_1 value greater than one is required to excite the first shear mode, there must be some other explanation for the observed velocity changes in the upper layer.

The anticipated effect of vertical residual stresses in the work-hardened layer can also be calculated from Ref. [11, 47]. Vertical residual stress was reported in Ref.[11] for a vertical plane running along the length of the rail and located at the section center line. These data showed a negligible vertical stress level for the top five millimeters of new and used rail. Below the 5-mm level, the vertical stresses for new rail become increasingly compressive, reaching a maximum of -80 MN/m^2(11.6 ksi) at a depth of 23 mm. The character of the change for used rail is similar. From the approximate zero level at 5 mm, the residual stress becomes increasingly compressive until reaching a maximum of -140 MN/m^2(20.3 ksi) at a 15-mm depth.

The change in wave speed caused by these stress changes for a shear wave propagating along the axis of the rail and polarized in the vertical direction (SV wave) can be calculated in the same manner used to evaluate the effect of longitudinal stress. The equivalent strain difference between the upper and lower sections of the head of the used rail is:

$$\epsilon = \frac{-140\ MN/m^2}{200{,}000\ MN/m^2} = -700\ \mu m/m \quad . \qquad (4.4)$$

The relative velocity change for this level of strain is $\Delta C/C^o = 1.0(10)^{-3}$ resulting in a velocity ratio of

$$\frac{B_2}{B_1} = \frac{1}{(1.+\ 1.(10)^{-3})} = 0.999 \quad . \qquad (4.5)$$

This effect is negligible when compared to the observed velocity ratios shown in Table V.

If the combined effects of longitudinal and vertical stresses on the SV wave are considered, the velocity ratio would be:

$$\frac{B_2}{B_1} = \frac{1}{(1.+\ 1.35(10)^{-3})} = 0.9986 \quad . \qquad (4.6)$$

This is also small, and a stress difference can be dismissed as a contributor to the observed shear wave velocity change.

The effect of stress changes across the rail head can

be neglected since this has been shown to have a very small effect upon waves propagating in the manner of the SV wave [47].

Effect of Preferred Orientation (Texture) on the Velocity Change in the Cold-Worked Layer

Numerous authors have discussed propagation of waves and the general elastic properties of crystals. The summary presented by Green will be most useful for the present investigation [22].

The solutions for wave propagation in bulk, isotropic solids are recalled to be

$$v_1 = \left((\lambda + 2\mu)/\rho\right)^{\frac{1}{2}}$$

and

$$v_2 = v_3 = (\mu/\rho)^{\frac{1}{2}} \qquad (4.7)$$

where v_1 - velocity of a pure longitudinal mode having particle motion in the direction of the wave front normal

v_2, v_3 - velocities of pure transverse modes having particle motions perpendicular to the wave normal and also mutually perpendicular

λ, μ - Lamé constants

ρ - density

In all three cases, the energy front travels in the same direction as the wave normal.

A general expression for the equation governing the waves propagating in an anisotropic medium, given by Green, is:

$$\left| c_{ijk\ell} \ell_\ell \ell_j - \rho v^2 \delta_{ik} \right| = 0 \qquad (4.8)$$

where $c_{ijk\ell}$ = second order elastic constants

ℓ_ℓ, ℓ_j = direction cosines of the normal to the plane wave

v = velocity

and δ_{ik} = Kronecker delta .

Now, let

$$\lambda_{ik} = c_{ijk\ell} \ell_\ell \ell_j \qquad (4.9)$$

so that by changing from tensor notation to matrix notation for the elastic constants, assigning $\ell_1 = \ell$, $\ell_2 = m$ and $\ell_3 = n$ and recognizing certain characteristics of the crystals, one can obtain simplified expressions as follows.

For cubic crystals it has been shown that there are only twelve non-zero elastic constants c_{ij}, i.e.,

$$c_{11} = c_{22} = c_{33}$$

$$c_{12} = c_{21} = c_{13} = c_{31} = c_{23} = c_{32}$$

$$c_{44} = c_{55} = c_{66}$$

where all other c_{ij} are zero. Therefore, Eqs. (4.9) become:

$$\lambda_{11} = \ell^2 c_{11} + (m^2 + n^2)c_{44}$$

$$\lambda_{12} = \lambda_{21} = \ell m(c_{12} + c_{44})$$

$$\lambda_{13} = \lambda_{31} = n\ell(c_{12} + c_{44}) \qquad (4.9a)$$

$$\lambda_{23} = \lambda_{32} = mn(c_{12} + c_{44})$$

$$\lambda_{22} = (\ell^2 + n^2)c_{44} + m^2 c_{11}$$

$$\lambda_{33} = (\ell^2 + m^2)c_{44} + n^2 c_{11} \quad .$$

Also, by substituting Eqs. (4.9) into Eq. (4.8), one can write the following matrix equation:

$$\begin{vmatrix} \lambda_{11} - \rho v^2 & \lambda_{12} & \lambda_{13} \\ \lambda_{21} & \lambda_{22} - \rho v^2 & \lambda_{23} \\ \lambda_{31} & \lambda_{32} & \lambda_{33} - \rho v^2 \end{vmatrix} = 0 \qquad (4.10)$$

It can now be shown that the assumption of a set of direction cosines for the wave normal and elastic constants will result in solutions for the three wave velocities.

Consider the cubic crystal shown in Fig. 20. A plane wave propagating in the [100] direction will have direction cosines $\ell = 1$, $m = n = 0$.* Substituting these values

---

* The use of Miller indices is discussed in most basic metallurgical and materials texts. See Barrett and Massalski, for example [27].

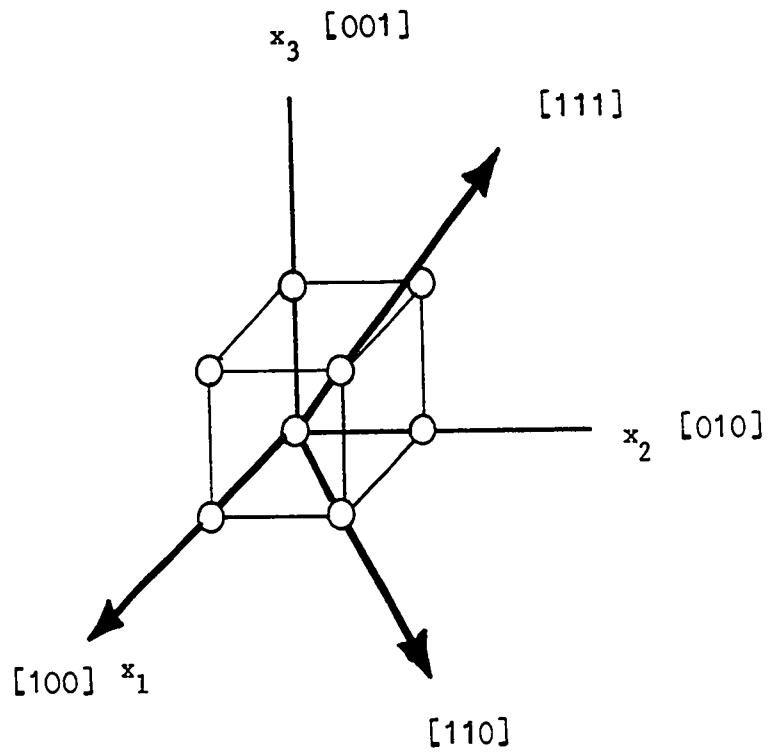

Figure 20. Cubic Crystal

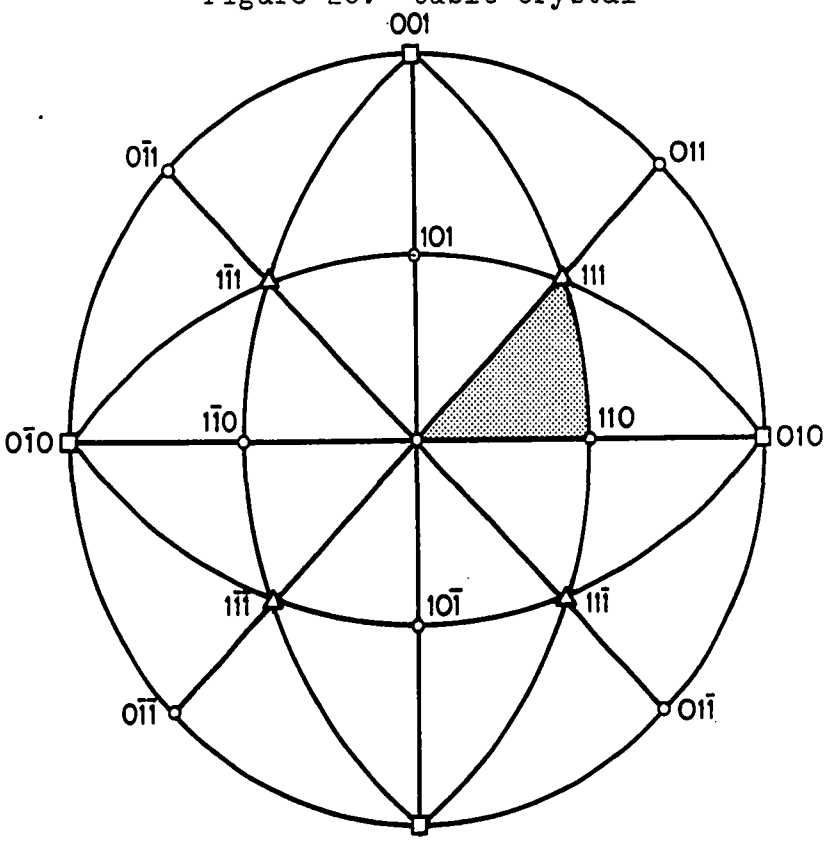

Figure 21. Stereographic Projection System Centered About [100]

into Eqs. (4.9a) and (4.10), one obtains the solutions:

$$(c_{11} - \rho v^2)(c_{44} - \rho v^2)(c_{44} - \rho v^2) = 0 \quad . \qquad (4.10a)$$

The resulting wave velocities in the [100] direction are therefore:

$$\begin{aligned} v_1 &= (c_{11}/\rho)^{\frac{1}{2}} \\ v_2 &= v_3 = (c_{44}/\rho)^{\frac{1}{2}} \end{aligned} \qquad . \qquad (4.11)$$

With the substitution of Eqs. (4.9a) into an equation for the direction cosines of the particle displacements (eigenvectors) and using direction cosines $\ell = 1$, $m = n = 0$, Green showed that the particle motions associated with the velocities in Eq. (4.11) are identical to those assumed for Eqs. (4.7). Here v_2 and v_3 are defined to have particle motions in the [010] and [001] directions, respectively. Also, the energy flux vector can be shown to be in the direction of the wave normal for this case.

For plane waves propagating in the [110] direction, the direction cosines will be $\ell = m = 1/\sqrt{2}$ and $n = 0$. The resulting velocities are:

$$\begin{aligned} v_1 &= [(c_{11} + c_{12} + 2c_{44})/2\rho]^{\frac{1}{2}} \\ v_2 &= [(c_{11} - c_{12})/2\rho]^{\frac{1}{2}} \\ v_3 &= (c_{44}/\rho)^{\frac{1}{2}} \end{aligned} \qquad . \qquad (4.12)$$

An analysis of particle displacements shows that v_1 again is a pure longitudinal mode, v_2 is a pure transverse mode with particle motion in the [110] direction, and v_3 is also a pure transverse mode but with particle motion in the [001] direction. Moreover, the energy flow is in the same direction as the wave normal.

In the [111] direction, the direction cosines of the wave normal are $\ell = m = n = 1/\sqrt{3}$ and the velocities are:

$$v_1 = \left[\frac{c_{11} + 2c_{12} + 4c_{44}}{3\rho}\right]^{\frac{1}{2}}$$

$$v_2 = v_3 = \left[\frac{c_{11} - c_{12} + c_{44}}{3\rho}\right]^{\frac{1}{2}} \quad . \tag{4.13}$$

Here again, v_1 is a pure longitudinal mode, and v_2 and v_3 are pure transverse modes. For the longitudinal mode, the energy flux is again in the direction of the wave normal, but for the transverse modes, Green showed that the energy flux deviates from the wave normal by an angle

$$\delta = \tan^{-1}\frac{c_{11} - c_{12} - 2c_{44}}{\sqrt{2}\,(c_{11} - c_{12} + c_{44})} \quad . \tag{4.14}$$

In order to fully discuss wave propagation in crystals at arbitrary directions, the stereographic projection is employed. Stereographic projections were described by Barrett and Massalski [27]. These are merely graphical presentations

of some geometric parameter of a crystal, velocity in this case. Green [22] and Gold [48] have used this technique in wave velocity calculation for various crystals.

A stereographic triangle for cubic crystal is shown in Fig. 21. In crystallographic notation, a line over an index indicates a negative direction. Following Green, the [100] direction is seen to come directly out of the paper while the [110] and [111] directions are at the other corners of the darkened triangle.

Wave velocities at various angles can be calculated from Eqs. (4.9a) and (4.10) once a set of direction cosines (ℓ, m and n) have been assumed. A computer program was written to obtain these solutions. Constant-velocity (isospeed) contours for the three types of waves in an iron crystal are shown in Figs. 22a, 22b and 22c. These results are similar to those given by Gold [48]. Table VIII lists the material constants used in these calculations.

Precise velocities are shown for v_1, v_2 and v_3 along each of the [100], [110] and [111] directions. The velocity of v_1 is seen to be different along each direction. The values for v_2 and v_3 are seen to be equal to each other on the [100] and [111] axis and unequal along the [110]. From the isospeed contours, v_3 is seen to be greater than v_2, except at the poles [100] and[111] where they are equal. Musgrave has plotted velocity contours for all three waves propagating in the [001] and [110] planes in an iron crystal [49].

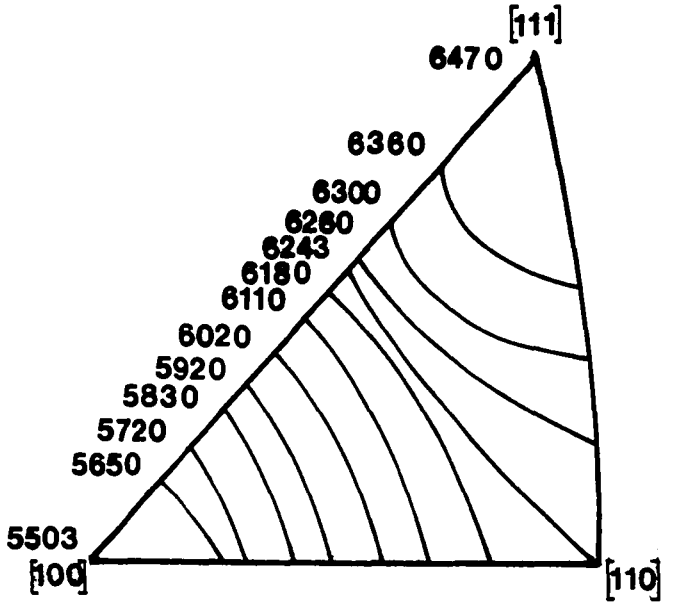

Figure 22a. Isospeed Contours for Longitudinal Waves in Iron [v_1(m/s)]

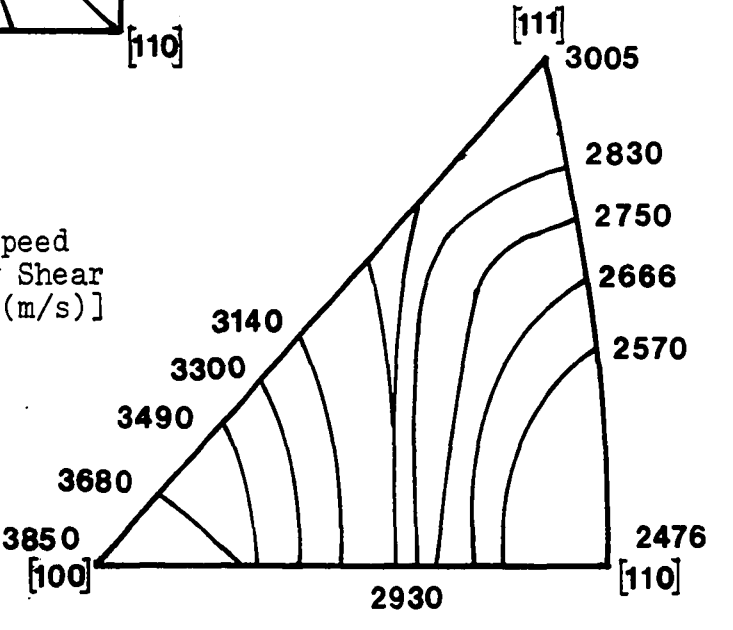

Figure 22b. Isospeed Contours for Slow Shear Waves in Iron [v_2(m/s)]

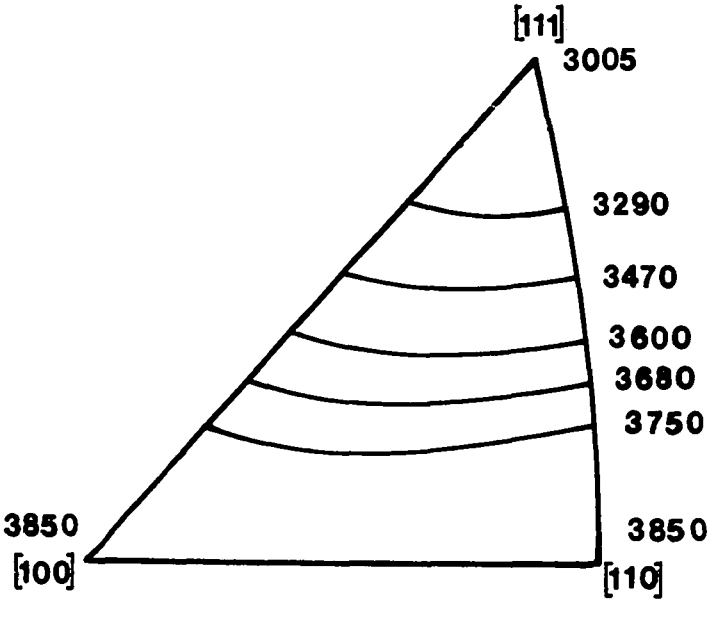

Figure 22c. Isospeed Contours for Fast Shear Waves in Iron [v_3(m/s)]

Table VIII. Material Constants for Iron

c_{11}	$23.7(10)^{10}$ N/m^2
c_{12}	$14.1(10)^{10}$ N/m^2
c_{44}	$11.6(10)^{10}$ N/m^2
ρ	$7.826(10)^{3}$ kg/m^3

Note: Density is for 0.9%C Steel

For a cubic crystal, symmetry demands that a complete description of wave velocities in the crystal can be obtained from the information in the triangle. That is to say that any direction found outside of the triangle has a counterpart which is crystallographically related to a direction within the triangle.

Sullivan and Papadakis, among others, have shown that the accurate measurement of ultrasonic velocities can be used to determine the existence of preferred orientation in rolled metals [50]. It was first observed that for a material structure having completely random orientation, the two transverse waves would have exactly the same velocity when passing through the thickness of the test specimen. On the other hand, if a rolled texture existed in the specimen, such as the one previously described for the rail, a difference in v_2 and v_3 would be noted at certain propagation directions. Pole figures for rolled iron have been produced, using this technique, by rotating the transducers through a vertical axis passing through the specimen thickness. Alers and Liu [51] and Tittman and Alers [52] have also reported results on the ultrasonic evaluation of material texture. Markham has reported ultrasonic wave velocities at orthogonal directions in several anisotropic materials including a sample of 0.9%C (pearlitic) steel [53].

Rayleigh-wave critical-angle reflectivity has been applied to determining the amount of cold work in metals. Using water as the coupling medium, Reimann and Cason showed

that for a piece of 316 stainless steel, the Rayleigh-wave critical angle increased from approximately 30.5^{o} to greater than 34^{o} as the percentage of cold work increased from 0 to 50 [54]. Becker and Richardson have developed an accurate mathematical model describing Rayleigh-wave critical-angle reflectivity using vibrations in solids and hysteresis between stress and strain to account for the behavior [55]. Later work showed the effect of material density and wave velocities on the critical angle [56].

Texture Models for Determining Preferred Orientation in Used Rail

Ultrasonic investigations into material texture are dependent upon knowing which textures are to be expected and what the velocity variations are for each. Table IX lists five textures which have been reported in worked steel. As before, the numbers in parentheses represent the plane parallel to the rolling plane, and the numbers in square brackets give the crystallographic directions which are aligned with the direction of rolling. The comparative X-ray intensities for textures I through IV are for cold-drawn mild-steel strip.

In the present case, the top surface of the rail head is considered to be the plane of rolling, and the longitudinal axis of the rail is considered to be the rolling direction. Case IV would be unlikely to occur in the rail

Table IX. Textures in Worked Steel

Case	Texture	Comparative X-ray Intensities from Reflecting Plane		Remarks	References
		High Δ	Large amount of material reduction		
I	(100)[001]	Increased	Increased	—	[13]
II	(100)[011]	Same as case I	Same as case I	Similar to case I but rotated 45° in rolling plane. Very common rolling texture.	[13], [27], [50]
III	(110)[001]	Increased	Decreased	—	[13]
IV	(111)[11$\bar{2}$]	Decreased	Decreased for High Δ	—	[13]
V	($\bar{5}$31)[112]	Increased	Increased	Approximation of (135)[313]	[24], [25]

case because of the decrease in X-ray intensities with higher values of Δ. All others could occur.

In order to experimentally investigate the texture of the cold-worked layer, velocity profiles were calculated for the rolling plane and for the vertical plane containing the rolling direction. This was done only for cases I, II, III, and V, and the results are plotted in Figs. 23 through 26, respectively. The top illustration shows the velocities of the longitudinal and the two transverse waves in the rolling plane. The same information is shown in the lower illustration for the vertical plane. In each case, the crystallographic direction which is expected to be aligned with the rolling direction is indicated to be downward.

The path of the end of the vector indicating the propagation direction is shown by the heavy line on the stereographic triangle at the right of the figure. Since a full 360° plot of the velocities involves directions out of the shaded triangle shown in Fig. 21, the notation of "directions of the form" has been adopted for the small triangle. This is indicated by the carets $\langle\rangle$ where, for example, the directions of the form $\langle 01\bar{1}\rangle$ have identical velocity properties. Typical $\langle 01\bar{1}\rangle$ directions are $[01\bar{1}]$, $[101]$, $[\bar{1}10]$, etc.

The velocity patterns in Fig. 23 for the (100)[001] texture show four-fold symmetry for directions in both the rolling plane and the vertical plane. In each case, the directions remain in a plane defined by $\langle 00\bar{1}\rangle$ and $\langle 01\bar{1}\rangle$.

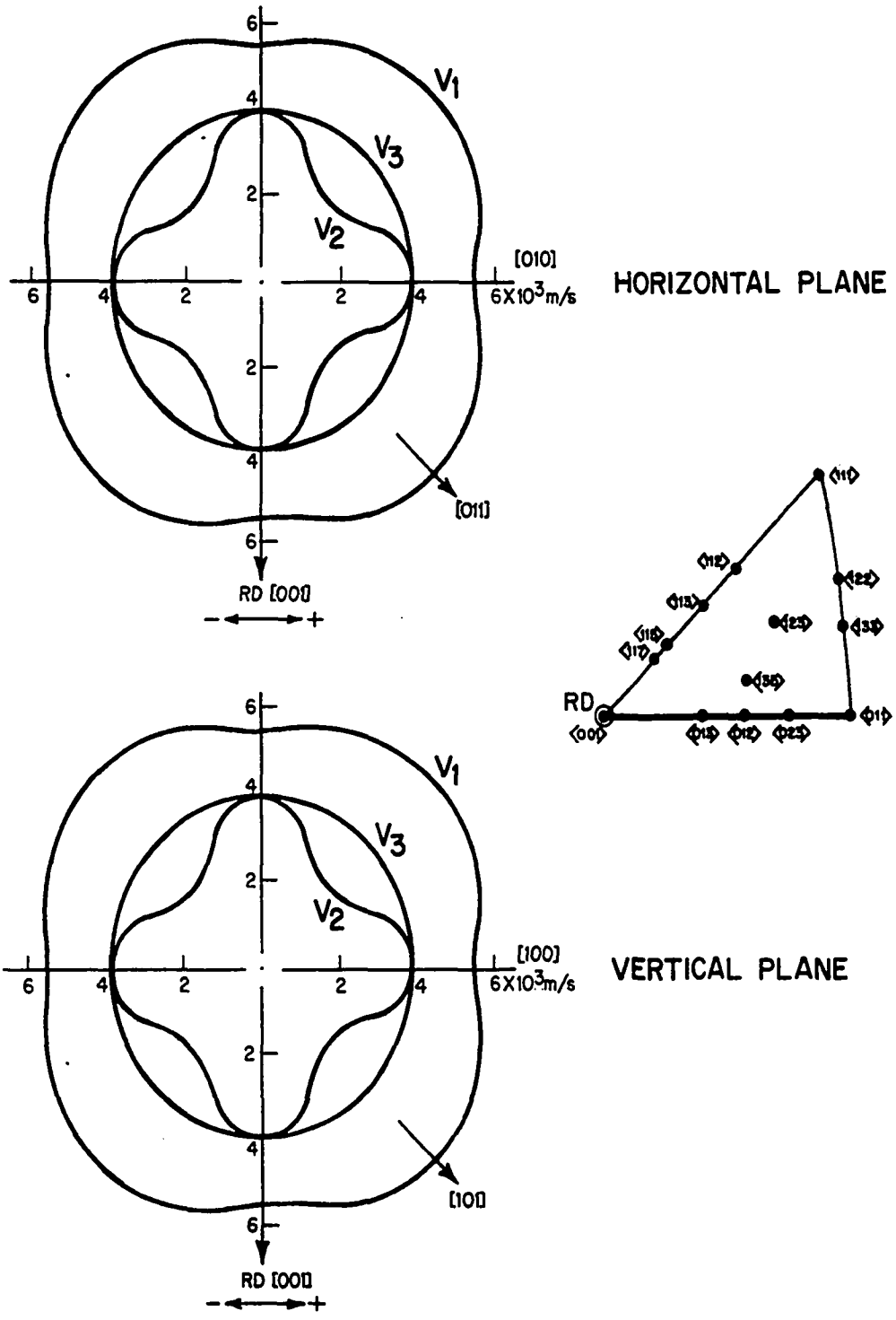

Figure 23. Velocities for (100)[001] Texture in Horizontal and Vertical Planes

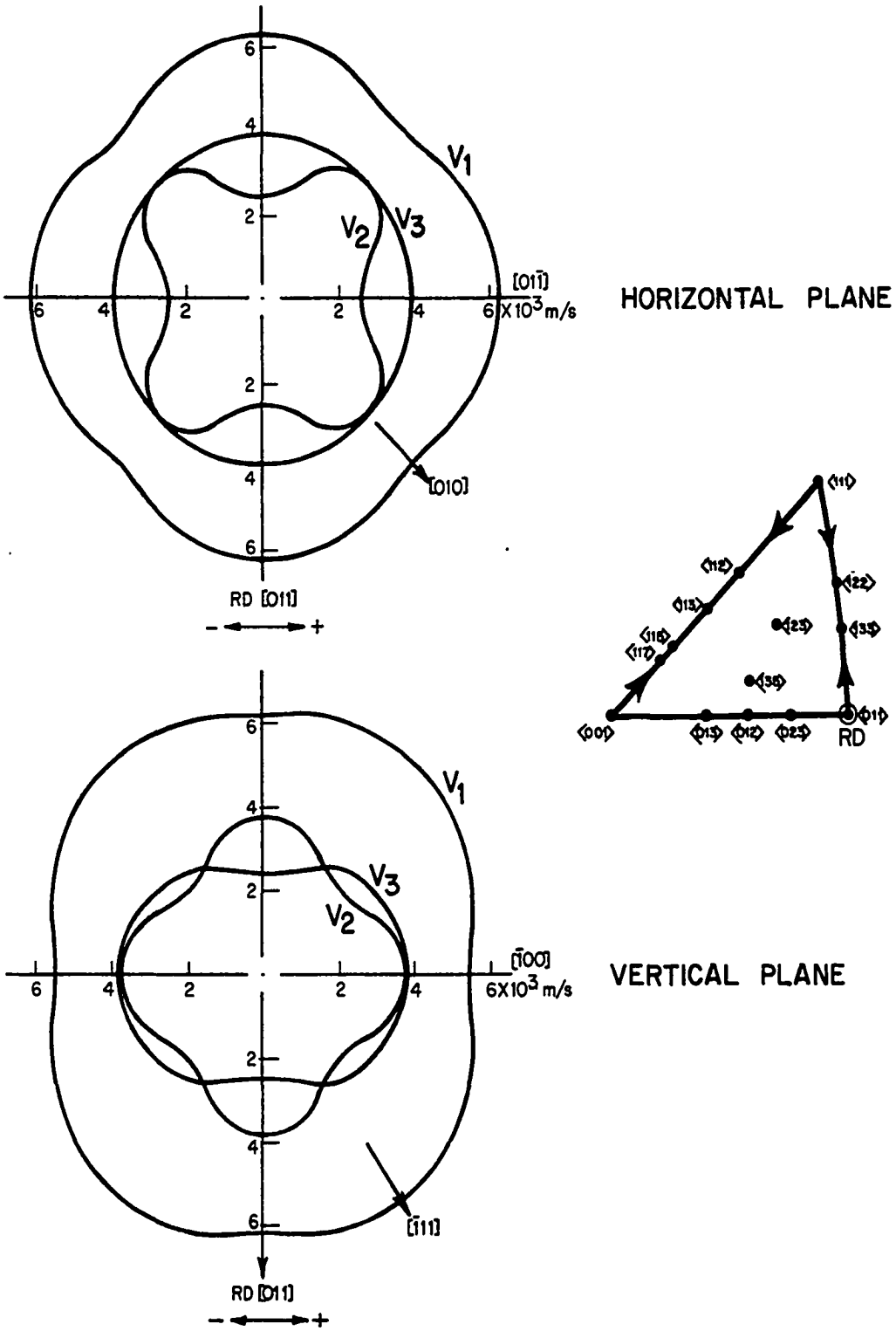

Figure 24. Velocities for (100)[011] Texture in Horizontal and Vertical Planes

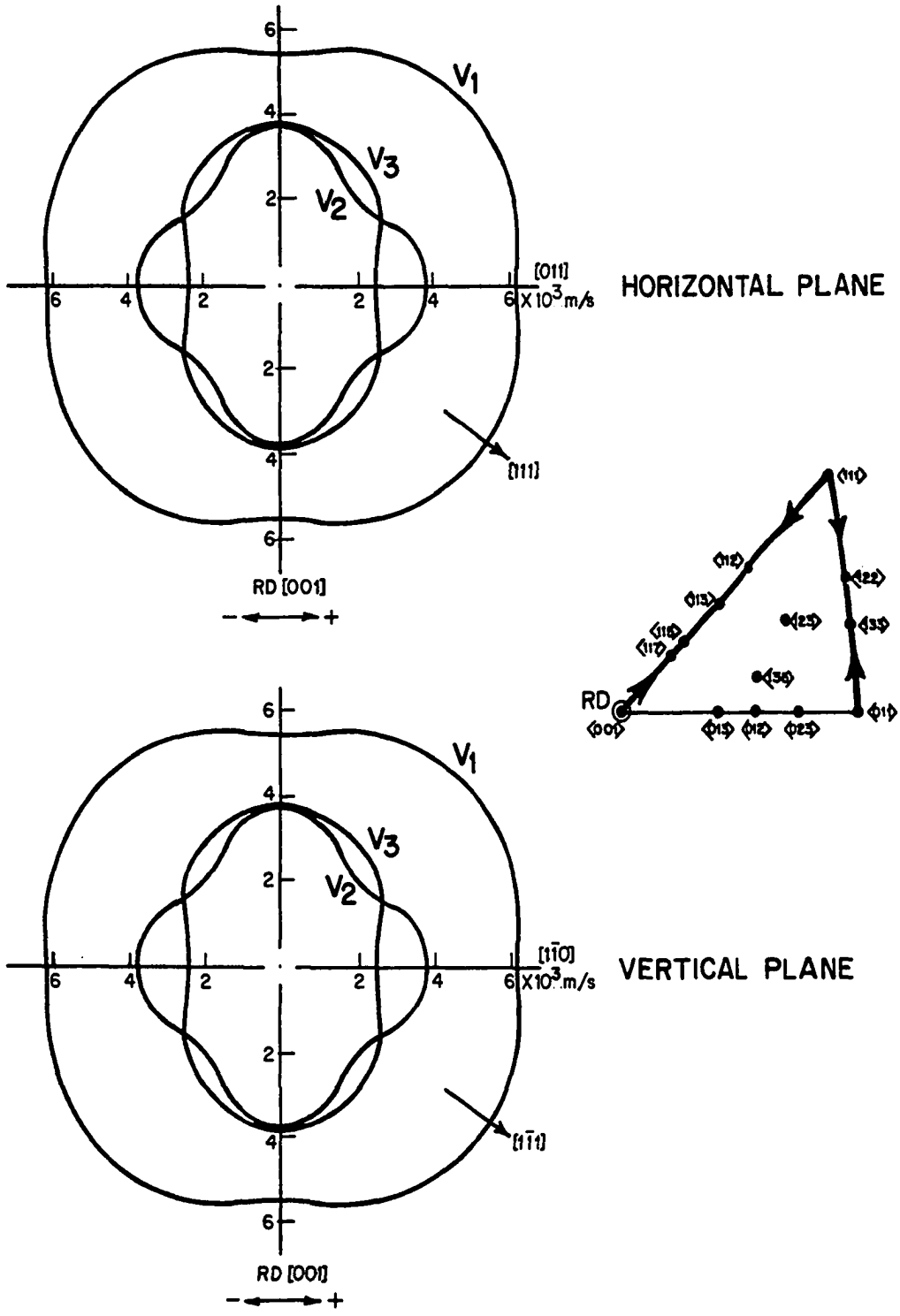

Figure 25. Velocities for (110)[001] Texture in Horizontal and Vertical Planes

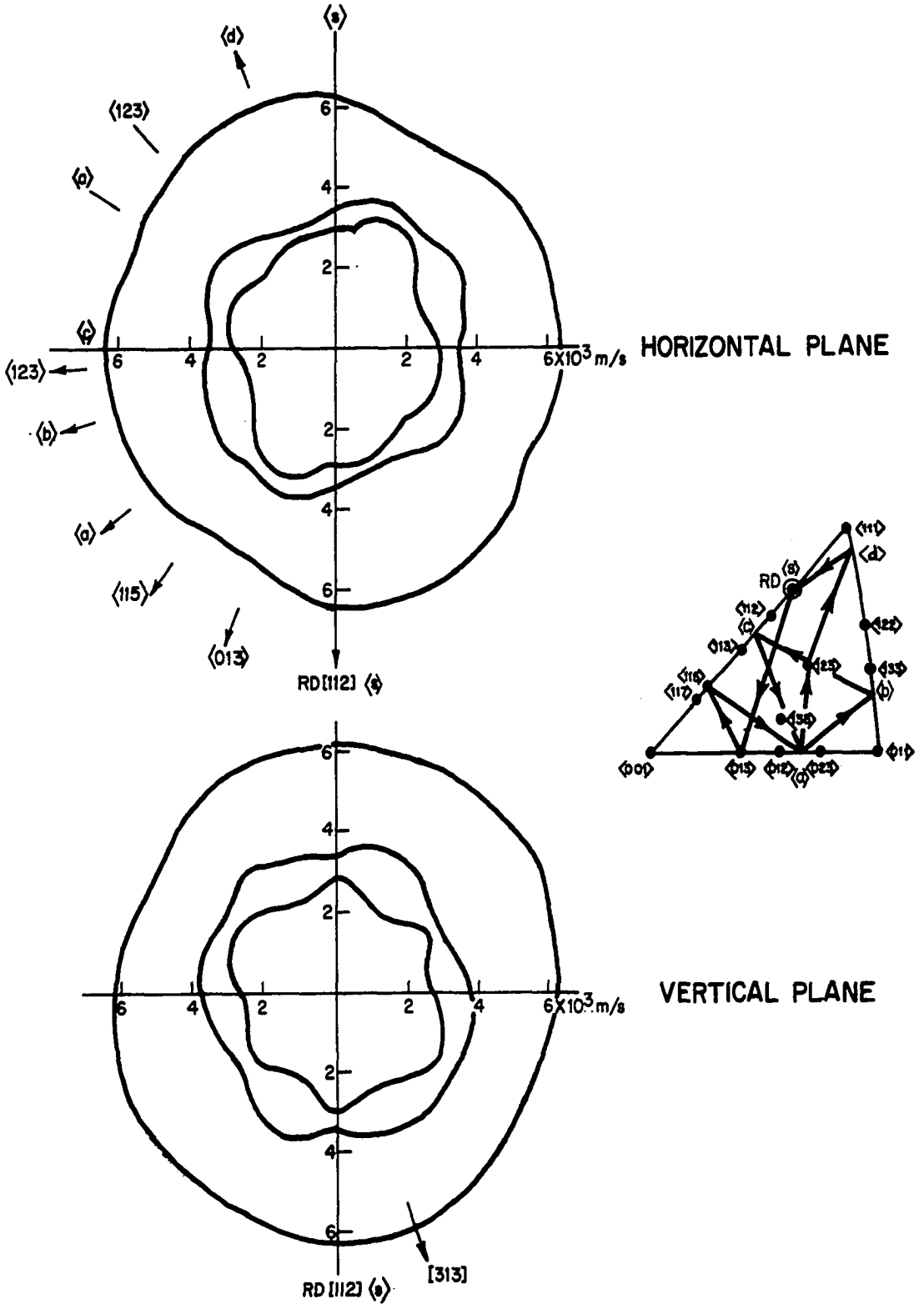

Figure 26. Velocities for $(\bar{5}31)[112]$ Texture in Horizontal and Vertical Planes

If velocity measurements for this texture were made in the rolling plane at directions 0°, 45° and 90° to the rolling direction, v_2 would be found to equal v_3 at the 0° and 90° directions. They would be unequal at 45°. Also, the longitudinal wave velocity would exhibit a maximum at 45° and have the same lower value at 0° and 90°. Identical behavior would be expected from measurements taken in the vertical plane. Solutions for velocities in each of these directions are tabulated in Table X for all cases. The expected velocity difference ($v_3 - v_2$) is also listed.

The velocity profile shown in Fig. 24 for the rolling plane of the (100) [011] texture is exactly the same as in the rolling plane of case I except for [011] now being in the rolling direction. As before, the path for the vector in this plane is between ⟨001⟩ and ⟨011⟩. The vertical plane behaves differently, since it is now in (011). This profile shows two-fold symmetry, and its propagation vector lies between ⟨011⟩ and ⟨111⟩. For velocities in the rolling plane, v_2 would be equal to v_3 at the 45° direction but unequal at the 0° and 90° directions. The longitudinal wave would indicate a maximum at 0° and 90° and a minimum at 45°. In the vertical plane, v_2 is equal to v_3 at 35.3° (corresponding to ⟨111⟩) and at 90°. A large difference exists between these two velocities at 0°. The longitudinal wave shows a maximum at 35.3°, a lower value at 0° and a minimum at 90°. These velocities are also tabulated in Table X. Barrett and

Table X. Predicted Velocities from Various Ideal Textures (m/s)

CASE I (100)[001]

	Horizontal Plane				Vertical Plane			
θ	v_1	v_2	v_3	(v_3-v_2)	v_1	v_2	v_3	(v_3-v_2)
0°	5503	3850	3850	0	5503	3850	3850	0
45°	6243	2476	3850	1374	6243	2476	3850	1374
90°	5503	3850	3850	0	5503	3850	3850	0

CASE II (100)[011]

	Horizontal Plane				Vertical Plane			
θ	v_1	v_2	v_3	(v_3-v_2)	v_1	v_2	v_3	(v_3-v_2)
0°	6243	2476	3850	1374	6243	2476	3850	1374
45°	5503	3850	3850	0	6410	2883	3242	359
90°	6243	2476	3850	1374	5503	3850	3850	0

CASE III (110)[001]

	Horizontal Plane				Vertical Plane			
θ	v_1	v_2	v_3	(v_3-v_2)	v_1	v_2	v_3	(v_3-v_2)
0°	5503	3850	3850	0	5503	3850	3850	0
45°	6410	2883	3242	359	6410	2883	3242	359
90°	6243	2476	3850	1374	6243	2476	3850	1374

Table X (continued)

CASE V $(\bar{5}31)[112]$

	Horizontal Plane				Vertical Plane			
θ	v_1	v_2	v_3	(v_3-v_2)	v_1	v_2	v_3	(v_3-v_2)
0°	6263	2899	3507	608	6263	2899	3507	608
$+45^\circ$	6274	2745	3609	864	6040	2936	3850	914
-45°	5944	3173	3805	632	6380	2664	3483	819
90°	6280	2818	3542	724	6180	2730	3779	1049

Massalski stated that this is the chief texture found in rolled steel. They further stated that deviations up to 55° can occur in the orientations. These variations are related to the amount of material reduction [27].

As was true for case I, the rolling plane and vertical plane show identical velocity profiles for case III, (110)[001]. This is shown in Fig. 25. Moreover, these profiles are the same as shown for the vertical plane in case II with the rotation of 90°. All propagation vectors lie in the path from ⟨001⟩ to ⟨11⟩ to ⟨01⟩. For this texture, v_2 equals v_3 at 0° and 54.7°, but v_3 is considerably greater than v_2 at 90°. The maximum longitudinal wave velocity occurs at 54.7°, and the minimum occurs at 0°. The value of v_1 at 90° is greater than the value found at 0°.

The profiles for case V are considerably more complicated than for the others. The path for a 180° rotation in the rolling plane (135) is shown in the stereographic triangle. The directions indicated by the lower case letters were not reduced to Miller indices but are provided as an aid in viewing the velocity profiles.

The $(\bar{5}31)[112]$ texture is slightly different from the (135)[313] reported by Krause [25]. The [313] direction is approximately sixteen degrees from the $(\bar{5}31)$ plane. The choice of [112] for the rolling direction slightly affects the velocity values, but the pattern for the rolling plane is similar to that expected from a rolling plane passing

through [313]. The vertical plane passing through [112] also passes through [313]. The [313] direction is approximately fourteen degrees from the [101] direction that is used in case II as a rolling direction. The normal to the $(\bar{5}31)$ plane lies 32.3° from the normal to the $(\bar{1}00)$ plane. The $(\bar{5}31)[112]$ texture has been shown by Alers and Liu to provide a reasonable fit to observed Young's modulus data for a cold-rolled copper-zinc bar [51]. Copper is a face-centered-cubic structure so that the correlation with body-centered-cubic structures, such as iron, is not exactly correct.

The most significant feature of this texture is that the two shear wave velocities are never equal. The minimum difference occurs at approximately 20° (counter-clockwise) and -160° (clockwise). The fast shear wave (v_3) reaches a maximum at six locations while the least value occurs only twice (+20° and -160°). The slow shear wave (v_2) shows a more irregular pattern, reaching a minimum at -70° and +110°. The greatest difference in the two values occurs at these locations. The longitudinal wave velocity shows a more regular pattern reaching a maximum at +20° and -160°. Velocity values shown in Table X are for 0°, +45°, -45°, and 90° in the rolling plane and 0°, +45°, -45° and 90° in the vertical plane.

Experimental Investigations of Velocities in Cold-Worked Samples

In order to gain some insight into the material structure in the cold-worked layer of used railroad rail, velocity measurements were made on several sections removed from the rail head. The location of each sample in the rail head is shown in Fig. 27, and a description of each is given in Table XI. Samples T1 and T2 were used to evaluate the experimental technique.

Shear wave velocity measurements were made using the ultrasonic goniometer shown in Fig. 28. Two Panametrics Type V222 normal incident shear-wave transducers were used for sending and receiving the pulse across the specimen. These were highly damped transducers with a nominal resonant frequency of 20 MHz. Information furnished by the manufacturer showed the two transducers to have peaks at 10 MHz and 15 MHz, respectively. The piezoelectric element was one-quarter of an inch (6.35 mm) in diameter. A 2.05 μs, quartz delay section was built into each transducer. The face of this section was in contact with the specimen.

Longitudinal wave velocities were obtained with two one-half inch (12.7 mm) diameter Panametrics V109 highly damped transducers. The nominal resonant frequency of these was 5.0 MHz.

Pulses were excited and received with a Panametrics 5052PR Pulser/Receiver having a bandwidth of 10 kHz to

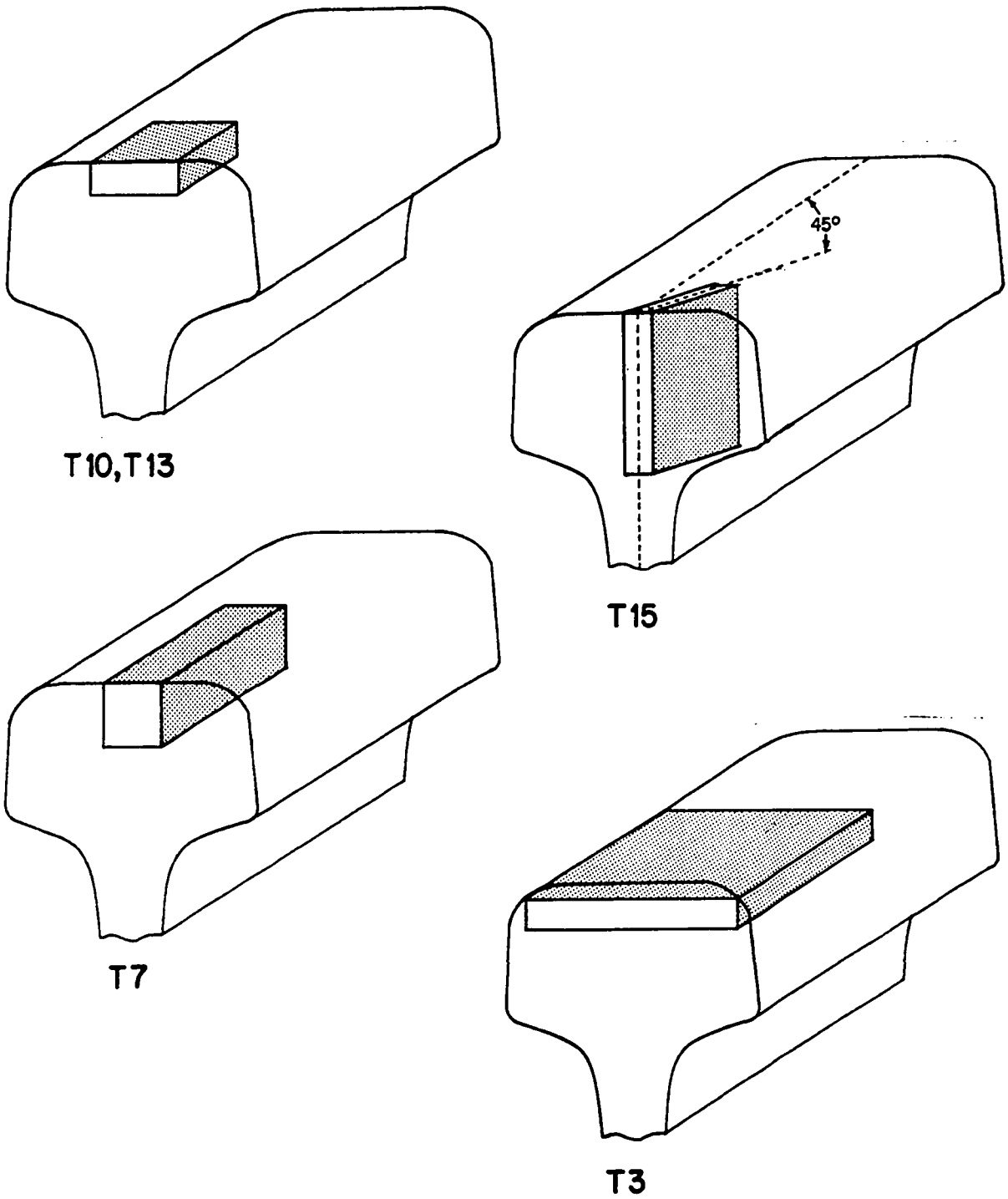

Figure 27. Specimens for Rail Texture Studies

Table XI. Description of Laboratory Samples Used in Texture Investigation

Sample	Thickness mm	Length mm	Width mm	Remarks
T1	9.496	75.0	65.0	Mild steel plate, annealed
T2	9.350	63.5	76.0	Cold-rolled 4140 steel bar
T3	8.255	45.7	54.0	Section of used rail just below cold-worked layer
T7	16.13	22.9	16.13	Middle of used rail with cold-worked layer at top
T10	4.712	23.0	20.0	Top layer of used rail
T13	4.712	23.0	20.0	Top layer of new rail
T15	2.527	31.7	19.0	45° section of used rail with cold-worked layer at top

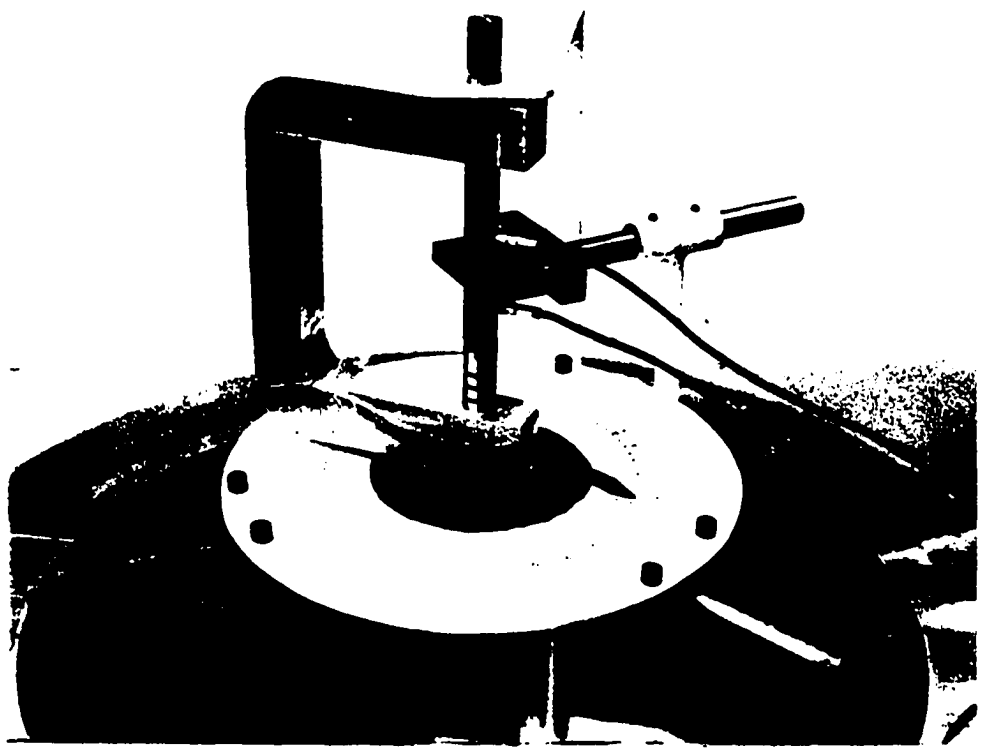

Figure 28. Ultrasonic Goniometer

30 MHz. A Tektronix 535A oscilloscope with a Type CA amplifier was used to display the received signals. The bandwidth of the oscilloscope was 2 Hz to 12 MHz. Velocities were determined from the arrival(s) at the receiving transducer in a through-transmission arrangement. Multiple echoes as seen by the receiver were used for greater accuracy when possible. Quite often the strong echoes arising within the transducer delay sections made it impossible to distinguish the multiple echoes occurring within the test specimen.

A coil spring was placed within the transducer holders and behind each transducer. The transducer holders were movable in the vertical direction and could be rotated for proper alignment. Shear-wave particle motion was in the direction indicated by the cable connections. A viscous shear-wave couplant was used between each transducer and the specimen. Each specimen was clamped between the transducers before the set screws on the specimen holding arm were secured. By doing this with care, no discernable misalignment occurred between the specimen and the transducer faces. Once the transducers and the specimen were fixed, the goniometer could be rotated freely. Angular position was marked at 5° intervals on the plate. Zero was at the position such that the shear-wave particle motion was parallel to the holding arm. A small section from +167 to -167° could not be reached because of goniometer and holding arm interference. If information was needed in this area, the specimen was rotated 90° in the holder.

The annealed specimen T1 was first checked in order to detect any bias resulting from the apparatus or from specimen misalignment. In a 167° scan, at 5° intervals, the lowest shear wave velocity (3219 m/s) was observed at 0° orientation, while a maximum of 3226 m/s was found at two locations, 75° and 160°. The average velocity was 3222.6 m/s with a standard deviation of 1.71 m/s. The piece was then rotated 90°, and a second 167° scan was made. In this case, the low velocity (3214 m/s) occurred at 80° which is equal to -10° at the original orientation. The velocity average for the piece rotated 90° was 3217 m/s with a standard deviation of 1.75 m/s. The general agreement of the location of the minimum velocity and the closeness of the two standard deviations indicated that the goniometer itself was not inflicting any serious bias on the measurement. The velocity averages differed by 0.17% (5.6 m/s). In general, the velocities with the piece rotated 90° were lower than those obtained at first. This could have been caused by a slight shift of the specimen as it was rotated or by a slight misalignment in the reclamping process. The maximum instrumentation error was felt to be ± 4 ns or 0.07%. It is unlikely that a uniform error would be made throughout one full series of tests, so the most logical cause of this error appears to be related to specimen shift or misalignment. Velocity variations within each set most likely resulted from an incomplete annealing of the sample.

A range of velocity variations to be expected in cold-rolled material was determined by the experiments on sample T2. The zero-degree location was along the direction of rolling, and the direction of propagation was along the vertical axis. Maximum velocities ranging from 3233 m/s to 3248 m/s were found to exist from -60° to $+45^{\circ}$ and $\pm 120^{\circ}$. Minima from 3203 m/s to 3211 m/s were found between the maxima. This produced a symmetric pattern with the axes roughly aligned with the rolling and transverse directions of the sample. The velocity variation from minimum to maximum was 45 m/s or 1.4%. These data were consistent with those of Firestone and Frederick for a cold-rolled steel plate [57]. With particle motion parallel and transverse to the rolling direction, they found velocities of 3243 m/s and 3114 m/s, respectively. This represents a velocity reduction of approximately 4%. With the agreement obtained between the results on the goniometer and those of Firstone and Frederick, and the significantly larger variations observed for the cold-rolled sample as compared to the annealed sample, it was felt that the usefulness of the goniometer had been well established.

Experimental Investigations of Velocity Variations in Rail Samples

Experimental investigations to attempt to determine the texture of the cold-worked zone consisted of taking

velocity data in the rolling plane (i.e. horizontal plane) at angles of 0°, 45° and 90° to the longitudinal rail axis. Velocity data in the vertical plane were taken at 0° and 90°. The 0° measurement in each plane would obviously be along the rolling direction and thus would be the same measurement.

The technique used to obtain these velocities was essentially the same as previously described for work with samples T1 and T2. To obtain the velocities v_2 and v_3, the goniometer was rotated until a definite minimum or maximum was found. They did occur at 90° to each other. Because of the smaller sizes and irregular shapes of some of the rail samples, the clamping method was modified. Samples T3, T10 and T13 could be fitted in the holder used for the earlier work. T7 and T15 were either taped or hand-held flush against the holder. Experimental velocities for all samples are reported in Table XII.

Data for the worked layer were obtained from specimens T7, T10 and T15. Sample T10 provided data for propagation in the vertical plane at 90° to the rolling direction. For data along the rolling direction and at 90° to the rolling direction in the horizontal plane, the probes were moved to the top of specimen T7 so that pulses were essentially propagating in the worked layer. A similar technique was used with T15 to obtain data in the horizontal plane at 45° to the rolling direction.

Table XII. Experimental Results of Velocity Measurements in Rail Samples (m/s)

TOP LAYER - USED RAIL

	Horizontal Plane				Vertical Plane			
θ	v_1	v_2	v_3	(v_3-v_2)	v_1	v_2	v_3	(v_3-v_2)
0°	5948	3142	3368	226	5948	3142	3368	226
45°	6097	3105	3347	242	--	--	--	--
90°	5908	2935	3202	267	6041	3173	3366	193

CENTER SECTION - USED RAIL

	Horizontal Plane				Vertical Plane			
θ	v_1	v_2	v_3	(v_3-v_2)	v_1	v_2	v_3	(v_3-v_2)
0°	5938	3237	3246	9	5938	3237	3246	9
45°	6068	3224	3240	16	--	--	--	--
90°	5908	3133	3158	25	6021	3190	3212	22

TOP LAYER - NEW RAIL

	Horizontal Plane				Vertical Plane			
θ	v_1	v_2	v_3	(v_3-v_2)	v_1	v_2	v_3	(v_3-v_2)
0°					--	--	--	--
45°	NOT OBSERVED				--	--	--	--
90°					5964	3318	3366	48

0.9%C (Pearlitic) Rolled Steel - Markham [53]

θ	v_1	v_2	v_3	(v_3-v_2)
0°	5943	3216	3216	0
90°	5928	3210	3218	8
90°	5933	3205	3216	9

The center section of the rail was investigated with specimens T3, T7, and T15. Velocities at 90° in the vertical plane were provided by T3. The velocities in the horizontal plane were obtained with the same method as used for the worked layer except that the probes were moved to the lower portion of each sample. The difference in arrivals in the center section and the worked layer were very obvious. Because of the relatively large diameter of the probes, it was not possible to establish the location of an exact boundary between the worked layer and the underlying layer.

A sample of the upper layer of a new rail (T13) is also included in the data. Only velocities in the vertical plane at 90° to the rolling direction were obtained with this sample.

Pulse arrivals through the various samples are shown in the photographs in Figs. 29, 30a, and 30b. An expanded display (time base 0.2 μs/cm) of pulses propagating in the horizontal plane and at 90° to the rolling direction are shown in Fig. 29. The lower trace shows the relatively undistorted first reflected pulse travelling through the center section, just below the worked layer. By moving the sample so that the pulse travels through the upper layer, the pulse becomes slightly distorted and moves ahead by just over 100 ns. This would be equivalent to approximately 70 ns for a single pass through the specimen and is the pulse arrival associated with v_3 in the horizontal plane at 90° in Table XII.

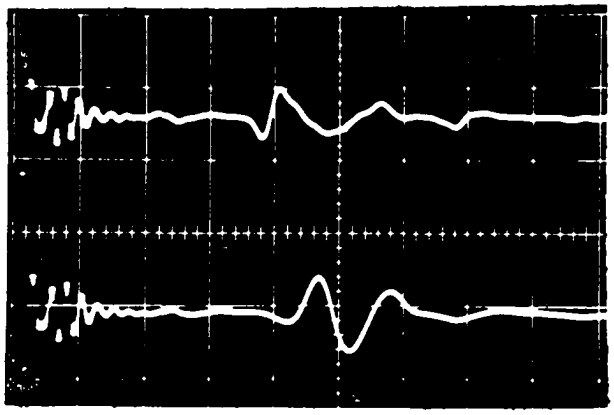

Figure 29. Fast Shear Wave Arrivals Propagating in the Horizontal Plane at 90° to the Rolling Direction. Top Trace-Propagation Through Worked Layer, Bottom Trace-Propagation Through Center Section. (Time Base 0.2 μs/div.)

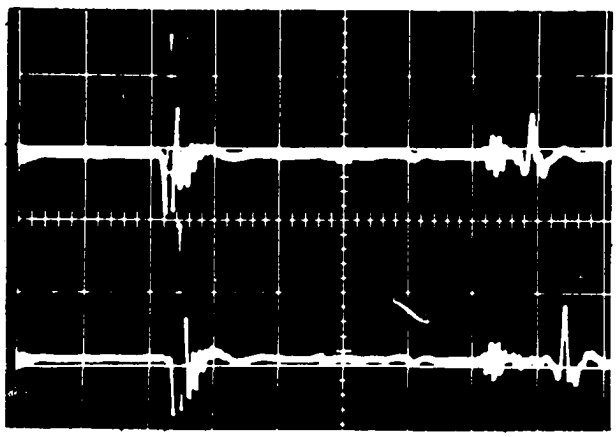

Figure 30a. Fast and Slow Shear Wave Arrivals Propagating Through the Worked Layer in the Vertical Plane and at 90° to the Rolling Direction (Specimen T10) Top Trace - 0° Polarization, Bottom Trace - 90° Polarization. (Time Base 0.5 μs/div.)

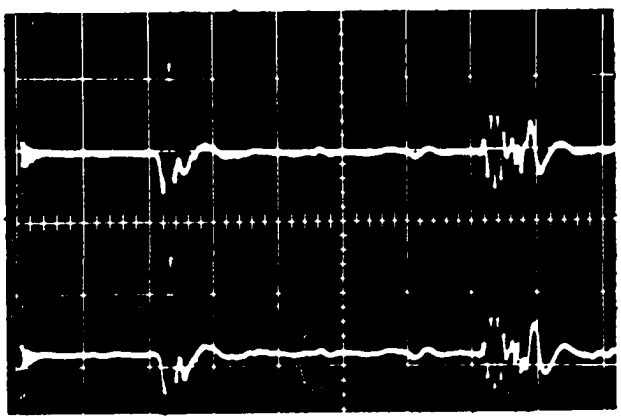

Figure 30b. Fast and Slow Shear Wave Arrivals Propagating through the Upper Layer of New Rail in the Vertical Plane and at 90° to the Rolling Direction (Specimen T13) Top Trace - 0° Polarization, Bottom Trace - 90° Polarization. Time Base 0.5 μs/div.)

The upper and lower traces in Figs. 30a and 30b show the fastest and slowest waves in samples T10 and T13, respectively. In these photographs the first arrival is the large signal at approximately 1.2 μs. The first reflected pulse is shown near to 4 μs, depending on the transducer rotation. The high frequency arrival ahead of the first reflection is the delay reflection in the transducer. In each case, the top trace is for a goniometer orientation of 0°, and the lower trace is for 90°. These are pulses propagating in the vertical plane at 90° to the rolling direction. Goniometer orientation at 0° is along the rolling direction. For piece T10, used rail, the significant decrease in velocity when the goniometer is rotated 90° is evident. This is shown in Fig. 30a. The pulse arrival is delayed by over 200 ns by the 90° rotation. The arrivals for the upper layer of the new rail, piece T13, are shown in Fig. 30b. A very small difference is seen between the 0° and 90° rotations.

A comparison of the data within Table XII shows the striking difference between the upper layer in used rail, the center section in used rail, and the upper portions of new rail. Most noticeable are the large values shown for $(v_3 - v_2)$ for the worked layer. This would most likely be a result of the amount of cold working in the upper layer as well as any texture differences. The values shown for the center section are those obtained by Markham for a high carbon rolled steel. These have been listed in Table XII, for

comparison purposes [53]. Two velocity sets are shown at 90° since he made no differentiation between a vertical and horizontal plane.

Any determination of material texture must be made by comparing the data shown in Table XII with the data in Table X and the pole figures shown in Figs. 23 through 25. For convenience, the experimental and predicted velocities in the horizontal plane have been plotted for a 90° rotation in Figs. 31 through 34. Only in a material where all crystals were perfectly aligned to create a particular texture would exact velocity agreements be expected. The differences (v_3-v_2) can yield some indication of a predominance of a specific texture. As previously cited by Barrett and Massalski, some variation around particular orientations is to be expected in most rolled material.

Considering the experimental data for the used rail, the small differences in the two shear wave velocities at each location in the center section are apparent. This is shown in both Table XII and Figs. 31 through 34. The velocities at 45° are slightly higher than those at 0°, and those at 90° are lowest of all. The same is true for the longitudinal wave velocities. The effect of rolling in the upper layer is to separate the two shear wave velocities. The velocity of the faster wave, associated with v_3, rises, and that of the slower velocity, associated with v_2, decreases. This is true for 0°, 45° and 90° locations. At 90°, the

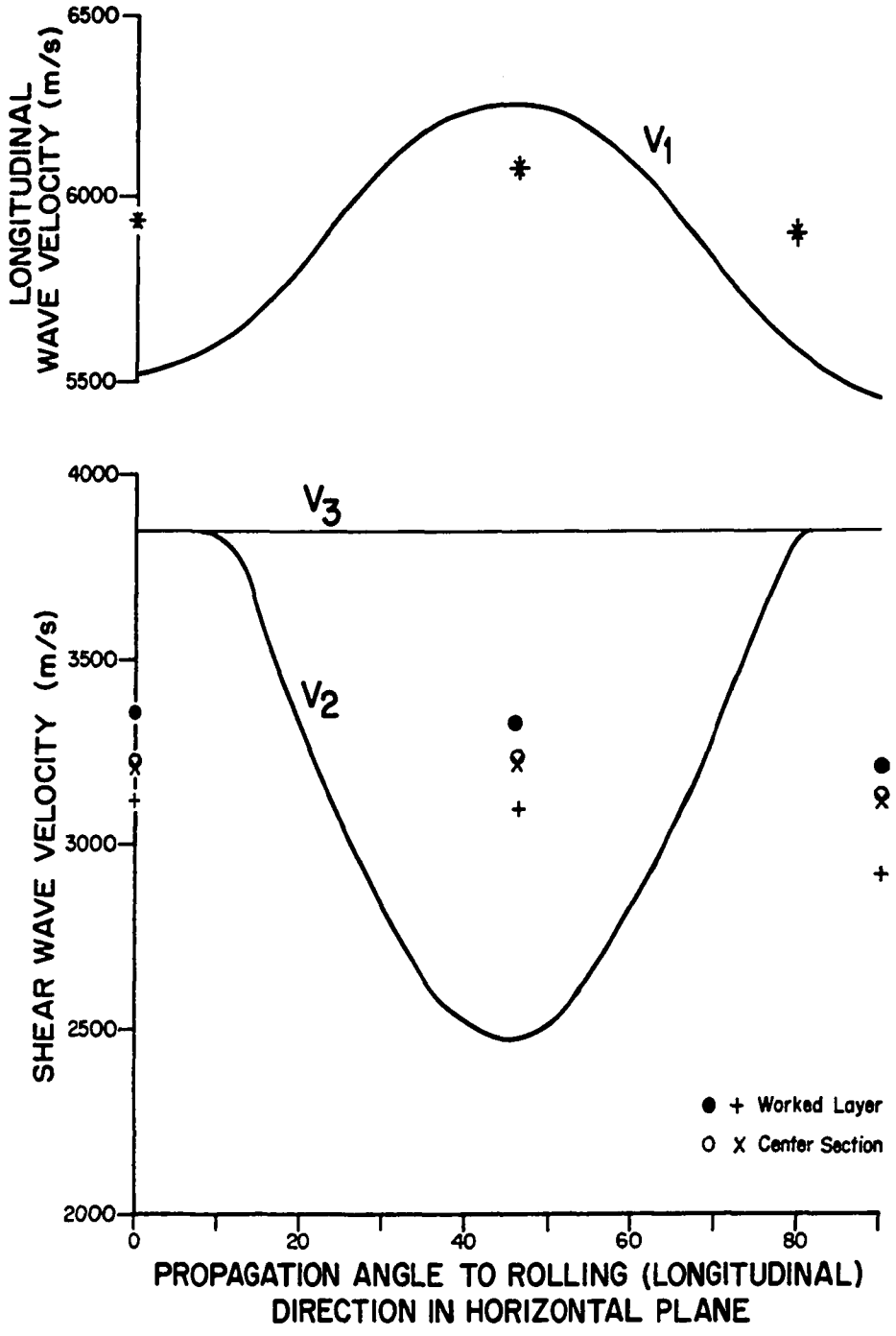

Figure 31. Experimental Data and Predicted Velocities for (100)[001] Texture

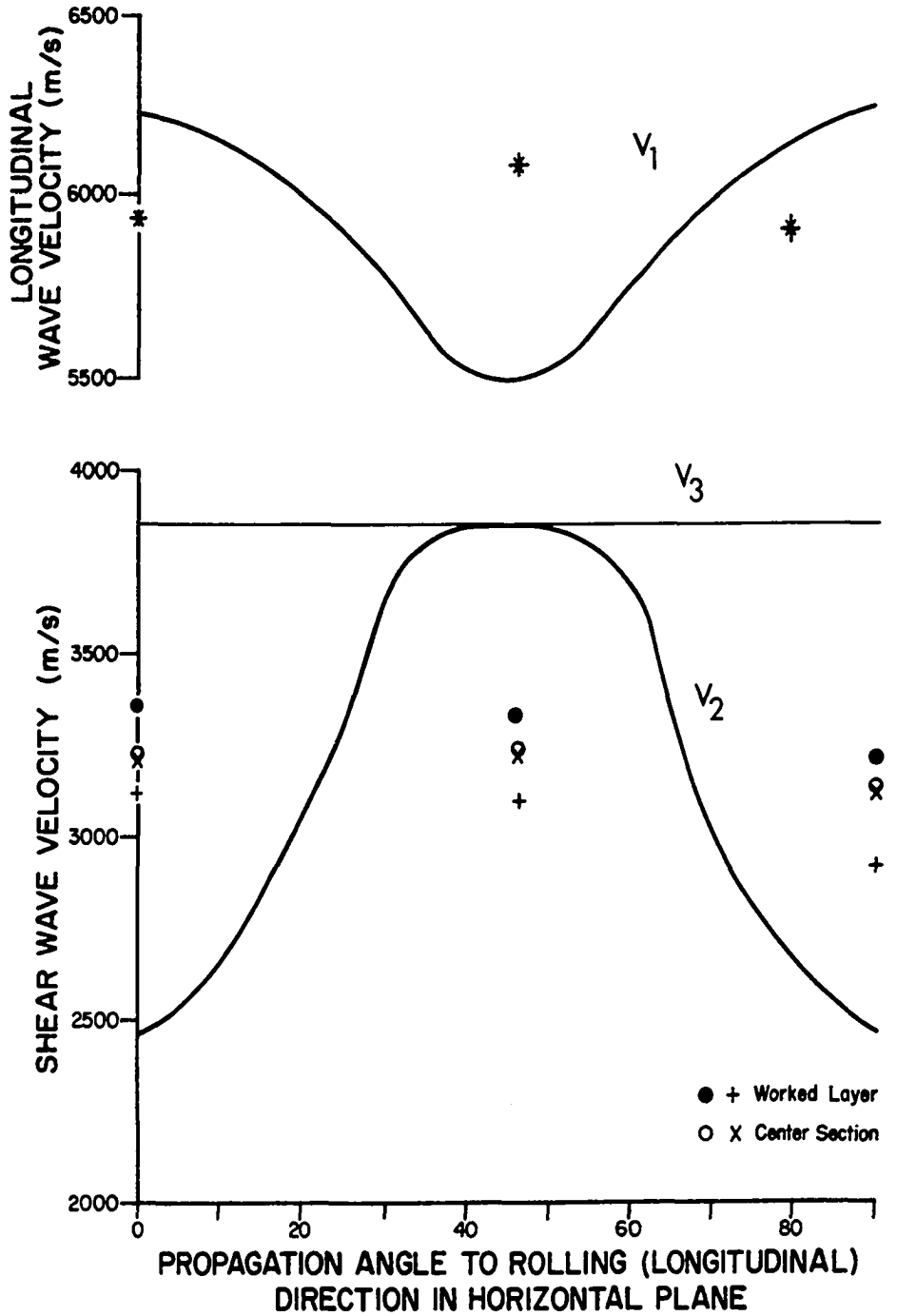

Figure 32. Experimental Data and Predicted Velocities for (100)[011] Texture

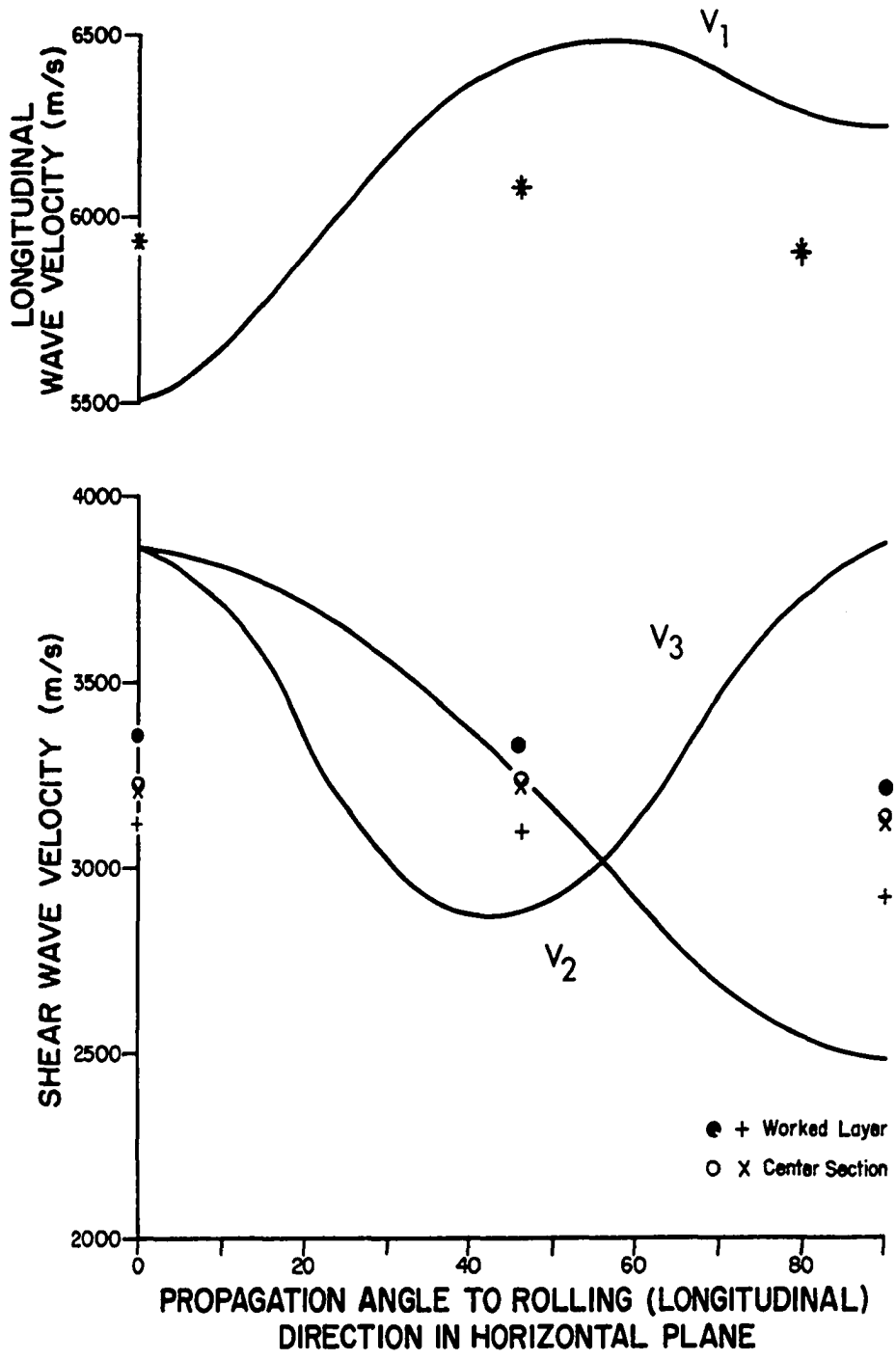

Figure 33. Experimental Data and Predicted Velocities for (110)[001] Texture

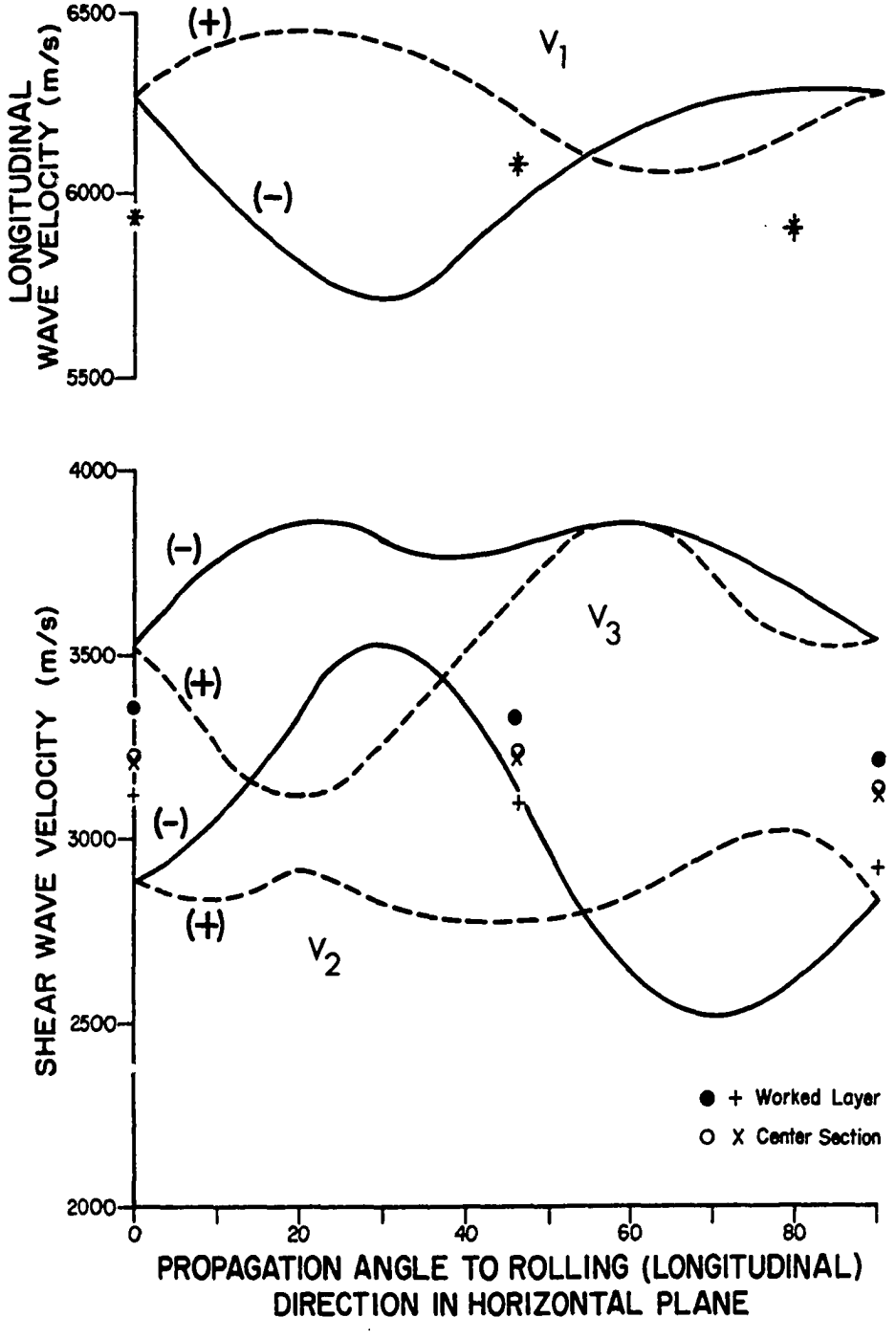

Figure 34. Experimental Data and Predicted Velocities for $(\bar{5}31)[112]$ Texture

v_3 velocity increases only slightly while the v_2 velocity decreases by a rather large amount. In the worked layer, v_3 decreases from 0° to 45° to 90°. The same thing occurs for v_2 except that the change from 0° to 45° is very slight. It is evident that the texture of case I does not predict the spreading of the two shear wave velocities at 0° and 90° locations. This removes this texture from consideration, despite the general agreement for shear wave velocity changes at 45° and all three longitudinal wave velocities.

Case II is the texture most commonly associated with rolled steel. This is shown in Fig. 32. Although the separation at 0° and 90° is predicted, that at 45° is not. Moreover, the predicted behavior of the longitudinal waves is opposite to that shown by the data. Therefore, this texture must be rejected for the cold-worked zone. It is possible that more accurate measurement techniques could confirm this texture in the center (or underlying) layer. This was not done since the primary purpose of these experiments was to investigate the cold-worked layer.

Case III (Fig. 33) shows the most serious disagreement between experimental and predicted velocity changes at 0° for the shear waves. It appears that the variation at 90° should be larger than that seen at 45°, but this does not occur in the experimental data. The longitudinal velocity should show a larger value at 90° than at 0°. This does not occur. The disagreement in shear wave velocities at 0°

is the primary reason for rejecting this texture from consideration.

The $(\bar{5}31)[112]$ texture shown in Fig 34 predicts the separation of shear wave velocities at the 0°, 45° and 90° locations. Two predicted velocities are shown for all waves because of the asymmetry of the velocities around the rolling texture. With these limited data, it is difficult to say whether better agreement exists with rotation in the positive or negative direction.

In a textured material, only a certain portion of the crystals will be perfectly aligned. The rest will be in varying stages of randomness along with a few other textures. As stated by Papadakis, the application of Waterman's single-crystal theory to an aggregate structure indicates that the observed shear wave velocities should lie between the limiting values found in the crystal [58,59]. Very accurate techniques, as described by Sullivan and Papadakis [50], can be used to determine the percentage of grains aligned in any particular texture. The multiple echoes that occurred in the delay sections of the probes used in this experiment prevented their techniques from being adopted. Nevertheless, the $(\bar{5}31)[112]$ texture does appear to provide the best agreement with the experimental data observed in the horizontal plane.

The shear-wave velocity difference at the 90° location in the vertical plane also shows a larger value in the

worked zone than in the center portion of the rail. The variations are comparable to those found in the horizontal plane. This is of interest since the upper portion used for sample T10 was necessarily taken from location on the rail different from where T7 was obtained. The spread of velocities in the worked layer also shows more consistency with the $(\bar{5}31)[112]$ texture than with the others.

The slowest shear-wave velocity observed along the rolling direction in the worked layer of sample T7 was 3142 m/s and was found at 22° from the vertical axis. The highest value, 3368 m/s, was found at 112°. Since this minimum was close to the vertical axis of the rail, it appears quite likely that the velocity reduction required for the existence of the observed early arrival in the surface wave studies was a result of a texture quite close to $(\bar{5}31)[112]$.

Summary and Conclusions

Residual stress and material texture have been investigated as probable causes of the shear-wave velocity reduction that occurs in the worked layer of used rail. In general, the changes predicted as a result of residual stress in the worked layer were quite small. Velocity changes predicted from an analysis of the texture of the worked layer were quite large and are the most likely cause of the appearance of the observed arrival just ahead of a Rayleigh wave propagating along the rail head.

CHAPTER V

SUMMARY, SUGGESTIONS FOR FURTHER WORK, AND CONCLUSIONS

There were two primary objectives of this investigation. One objective was to correctly identify the pulse arrivals that had been observed ahead of a Rayleigh wave propagating on the top surface of a used rail. The second objective was to investigate the possible causes of the shear-wave velocity change in the worked layer which was necessary to support the propagation of this early arriving pulse. The two investigations are independent, for the most part.

Chapter III, dealing with the propagation of waves in layered media, paid little attention to the properties of the worked layer and the underlying layer of the rail other than to assume certain velocity relationships of bulk longitudinal and shear waves propagating along the length of the rail. Chapter IV, on the other hand, delved into specific stress conditions and material property differences in the upper and lower portions of the used rail head.

The primary conclusion of Chapter III was that the early arriving pulses are comparable to the first shear mode, Sezawa waves, often observed in the propagation of seismic waves.

Both the early arriving pulses and the fundamental Rayleigh pulses were shown to be dispersive, i. e.,their velocities are frequency dependent over a certain range of frequency values. Moreover, early arrival was not observed at very low frequencies, in accordance with the theory.

The best agreement between the theoretical and the experimentally observed velocities was obtained by assuming velocities in the upper layer and the underlying structure which were slightly different from the initial values reported in Ref. [6]. The new assumptions, which were derived from experimental data related to the early arrival, were felt to be more compatable with the requirements of the geophysical model. Even with these new values, agreement between predicted and experimentally observed velocities was not exact, but it was felt to be sufficiently good to show that the early arrivals could be identified as the first shear mode.

In order for the first shear mode to exist in layered-media wave propagation, the shear wave velocity in the upper layer must be less than the shear wave velocity in the underlying structure. The most likely cause of this decrease in velocity in the work-hardened upper layer was felt to be either a differential in the residual stress, a change in the material texture or a combination of the two. Velocity changes resulting from stress differentials reported by other researchers were not of sufficient magnitude to explain the rather large (nearly 6%) decrease required to fit the experimental and

predicted velocities. The stress differential would also produce an increase in the shear wave velocity in the upper layer, opposite to the required change. Although the residual stress differential must be affecting the velocity, it was not felt to be the primary cause of the velocity change

Experimental investigations of shear and longitudinal wave velocities propagating at different directions in the worked layer and in the underlying layer indicated that large velocity changes could occur as a result of cold working of the material. The observed velocity patterns were compared with the velocity changes predicted by several ideal textures known to exist in rolled steel. The best agreement between observed and predicted velocity changes was found to exist for a $(\bar{5}31)[112]$ texture. This texture is not the one most commonly reported for rolled steel, but the amount of cold working found in the rail head is considerably greater than that found in most metal-working problems.

Since the wave propagation studies and the texture studies were performed separately, a comparison of the experimental results from each study is of interest. Table XIII shows velocity data which are comparable. Rail 7 has been used in this example, but a similar presentation could be made for rail 11. For rail 7 and rail model 7A, the values have been taken from Table V. Texture velocity data have been taken from Table XII.

Table XIII. Summary of Comparable Wave Velocities from Studies of Layered-Media Wave Propagation and Material Texture

	Rail 7	Rail Model 7A	Texture Data
A_1(m/s)	5872	6255	5948
B_1(m/s)	3120	3185	3142
A_2(m/s)	5868	6319	5938
B_2(m/s)	3195	3378	3237

Velocity values from the texture experiments taken at 0° to the rolling direction are felt to be comparable to the velocity definitions for A_1, B_1, A_2 and B_2 from the layered study, In the case of the shear wave, the lowest value (associated with v_2) is shown, since this occurred with a transducer orientation such that particle motion was near to the perpendicular to the rolling plane.

The shear wave velocities obtained in the texture investigations for both the worked layer and the underlying layer are higher than the values shown for rail 7. They are not as high as the values assumed for rail model 7A, however. In all cases, B_2 is greater than B_1. Similarly, the longitudinal wave velocities obtained in the texture studies are greater than the values for rail 7 but less than the values used in rail model 7A.

The fact that the values found in the texture studies are all higher than those originally found for rail 7 indicates that the assumption of higher velocities for rail models 7A and 11A was correct. The texture data were obtained using probes having a much higher frequency than those used to obtain any of the data used for the layered-media wave propagation studies. This is consistent with the observation in Chapter III that waveguide effects could account for the fact that the velocities originally observed were lower than the bulk velocities required for the geophysical model.

The lack of agreement between the assumed values for rail model 7A and the texture data could have several causes. The samples used in the texture studies were necessarily taken from a small section of the used rail. It is likely that the properties could vary along the length of the rail. The top surface of the used rails showed a slight wavy pattern most likely the result of uneven cold working (i.e. mild corrugations). The small pieces used in the texture study were also relatively stress-free because of the removal of the surrounding material. Nonetheless, the general agreement of the data was encouraging.

Suggestions for Further Work

Several new areas of investigation have been opened by this study. These are briefly outlined in the following paragraphs.

I. Experimental investigations of wave propagation in layers with slightly differing properties

An experimental investigation utilizing a large number of frequencies ranging from approximately 80 KHz to 5 MHz could more correctly establish the apparent thickness of the cold-worked layer. More precise frequency control and data gathering techniques should produce results which would very closely follow the predicted velocity curves. This investigation could also yield a more exact description of the boundary between the worked layer and the underlying structure.

II. Experimental investigation using a large number of rail samples to show the relationship of the appearance of the first shear mode and the degree of cold working in the upper layer

This investigation could be correlated with studies of rail shelling, corrugation and other fatigue and wear characteristics to see if the appearance of the first shear mode could be used in rail inspection as an indicator of the rail condition.

III. Experimental investigation of the texture of the cold-worked layer

The use of more precise velocity analysis techniques, as discussed in Chapter IV, could yield very accurate information concerning the texture of the cold-worked layer. By investigating the velocities in samples cut at smaller orientation intervals, e. g. 10°, and by using samples removed from rails having varying degrees of cold working, the gradual development of the final texture could be investigated.

This might have an important relationship to the onset of fatigue damage. X-ray diffraction studies of rail samples could assist in the texture investigation.

IV. Study of the relationship of rail fatigue and the gradual development of the cold-worked layer, in conjunction with paragraphs II and III

V. Investigation of the anisotropic effect of the cold-worked layer upon ultrasonic rail flaw detection

VI. Study of the cold-worked layer in wheels

Railway wheels experience cold working in a manner similar to the description given for rails. In some cases the carbon content of the wheels may be lower than for the rail. Most wheels experience large inputs of heat as a result of tread braking. The effect of this thermal input upon the character of the cold-worked layer and the resulting effect on wheel-tread fatigue damage could be investigated.

Conclusions

The investigations reported herein have shown that the cold-worked layer on heavily used rail is a reasonably well defined area. An ultrasonic pulse appears quite distinctly ahead of a Rayleigh wave propagating along the surface of the head of a used rail. The appearance of this pulse is frequency dependent. Texture in the cold-worked layer is the most reasonable explanation of why the early arriving pulse appears in used rail.

REFERENCES

1. Hirst, E., "Energy - Intensiveness of Transportation," Transportation Engineering Journal of American Society of Civil Engineers, Proceedings of the ASCE, 99, No. TE 1, 111-122 (February 1973).

2. "High Speed Ground Alternatives Study," U.S. Department of Transportation, Office of Systems Analysis and Information (January 1973).

3. Kneiling, J. G., Integral Train Systems, Kalmbach, Milwaukee, Wisc. (1969).

4. "Yearbook of Railroad Facts," Association of American Railroads, Economics and Finance Department, Washington, D.C. (1975).

5. Bray, D. E., "Railroad Accidents and Nondestructive Inspection," 1975 Proceedings of the Rail Transportation Division, American Society of Mechanical Engineers, New York, Paper No. 74-WA/RT-4 (1976).

6. Egle, D. M. and Bray, D. E., "Nondestructive Measurement of Longitudinal Rail Stresses," Federal Railroad Administration, Report FRA-75-40091 (June 1975).

7. "Steel Products Manual, Railway Track Materials," American Iron and Steel Institute, Washington, D. C. (October 1975).

8. "Railroad Facts, Technical Report No. 3," United States Steel Corporation (1968).

9. Johnston, J., "Time as a Factor in the Making and Treating of Steel," Transactions of AIMME, Iron and Steel Division, 150, 13-29 (1942).

10. Heindlhofer, K., Evaluation of Residual Stress, McGraw-Hill Book Co., New York (1948).

11. "Behavior of the Metal of Rails and Wheels in the Contact Zone, Composition of the Different Stress Conditions in the Wheel/Rail Contact Zone, Development of a New Fatigue Criterion," Office for Research and Experiments of the International Union of Railways, Utrecht, Report No. 7, C53/RP7/E (April 1972).

12. "Steel Products Manual, Wrought Steel Wheels and Forged Railway Axles," American Iron and Steel Institute, New York (1967).

13. Backofen, W. A., Deformation Processing, Addison-Wesley, Reading, Mass. (1972).

14. Martin, G. C. and Hay, W. W., "The Influence of Wheel-Rail Contact Forces on the Formation of Rail Shells," American Society of Mechanical Engineers, Paper No. 72-WA/RT-8 (1972).

15. Kalousek, J. and Klein, R., "Investigation into Causes of Rail Corrugations," American Railway Engineering Association-Bulletin, 77, No. 656, 429-448 (Jan.-Feb. 1976).

16. King, F. E. and Kalousek, J. "Rail Wear and Corrugation Studies," American Railway Engineering Association-Bulletin, 77, No. 658, 601-620 (June-July 1976).

17. Paul, B., "A Review of Rail-Wheel Contact Stress Problems," Federal Railroad Administration, Report FRA-OR&D 76-141 (April 1975).

18. "Report of Pennsylvania Railroad M. of W. Test No. 591, Determination of the Plastic Flow in Rail Head," Proceedings of the Fifty-Seventh Annual Meeting of the American Railway Engineering Association, Appendix 8-b, Report of Committee 4-Rail, Report on Assignment 8, Chicago, 59, 962-975 (1958).

19. Ravitskaya, T. M., "Features of the Initiation and Development of Internal Fatigue Cracks Considered on the Examples of Rail Failure," Problemy Prochnosti, Strength of Materials (Soviet), No. 11, 77-82 (November 1974).

20. "Behavior of the Metal of Rails and Wheels in the Contact Zone, Residual Stresses in the Rail (Continued) Study of the Work Hardened Zone," Office for Research and Experiments of the International Union of Railways, Utrecht, Report No. 6, C53/RP6/E (October 1970).

21. Lempitskii, V. V., Kazarnovskii, D. S. and Shnaperman, L. Ya., "Effect of the Strength of Railroad Rails on the Formation of Contact-Fatigue Damage Under Service Conditions," Problemy Prochnosti, Strength of Materials (Soviet), No. 9, 13-17 (September 1975).

22. Green, R. E., Jr., Treatise on Materials Science and and Technology: Ultrasonic Investigation of Mechanical Properties, Vol 3, Academic Press, New York (1973).

23. Dieter, G. E., Jr., Mechanical Metallurgy, Second Edition, McGraw-Hill Book Co., New York (1976)

24. Krause, H. and Scholten, J., "Factors Influencing the Frictional and Wear Behavior of the Wheel/Rail System," Proceedings of the Fifth International Wheelsets Congress, Tokyo, Japan, Paper No. I-7, 1-24 (October 1975).

25. Krause, H., Private communication in letter dated December 1, 1975.

26. Blanter, M. E., Gasanou, M. C., and Gulraeva, N. O., "Fine Crystal Structure of the Surface Layer of Steel Hardened with Rollers," Metal Science and Heat Treatment (Soviet), No. 3-4, 188-190 (March-April 1966).

27. Barrett, C. S., and Massalski, T. B., Structure of Metals, Third Edition, McGraw-Hill Book Co., New York (1966).

28. Gurvich, A. K., et al., Flaw Detection in Rails, Transport Publishing House, Moscow (1971). English translation in preparation.

29. Kaiser, W. D., et al., "Rail Inspection Systems Analysis and Technology Survey," Federal Railroad Administration, Washington, D.C., Report DOT-TSC-979-1 (May 1976).

30. Love, A. E. H., Some Problems in Geodynamics, Dover Press, New York (1967). Originally published by Cambridge University Press, 1911.

31. Lamb, H., "On Waves in an Elastic Plate," Proceedings of the Royal Society of London, Series A, 93, 114-128 (1917).

32. Stoneley, R., "Elastic Waves at the Surface of Separation of Two Solids," Proceedings of the Royal Society of London, Series A, 106, 416-428 (December 1924).

33. Sezawa, K., "Dispersion of Elastic Waves Propagating on the Surface of Stratified Bodies and on Curved Surfaces," Bulletin Earthquake Research Institute, Tokyo University, 3, 1-18 (1927).

34. Tolstoy, I., and Usdin, E., "Dispersive Properties of Stratified Elastic and Liquid Media: a Ray Theory," Geophysics, 18, No. 4, 844-870 (October 1953).

35. Ewing, W., Jardetzky, W., and Press, F., Elastic Waves in Layered Media, McGraw-Hill Book Co., New York (1957).

36. Bolt, B. A., and Butcher, J. C., "Rayleigh Wave Dispersion for a Single Layer on an Elastic Half Space," Australian Journal of Physics, 13, No. 3, 498-504 (September 1960).

37. Mooney, H. and Bolt, B., "Dispersion Tables for Rayleigh Waves on a Single Surface Layer," National Technical Information Service, Springfield, Va., Report No. AD 473 363 (October 1965).

38. Mooney, H. and Bolt, B., "Dispersive Characteristics of the First Three Rayleigh Modes for a Single Surface Layer," Bulletin of the Seismological Society of America, 56, No. 1, 43-67 (Feb. 1966).

39. Munasinghe, M., "Numerical Solutions for Acoustic Rayleigh Wave Problems in Anisotropic Layered Media," Ultrasonics, 14, No. 1, 9-14 (January 1976).

40. Kanai, K., "On the M_2 - waves (Sezawa - waves)," Bulletin of the Earthquake Research Institute, Tokyo University, 22, 39-48 (1951).

41. Sezawa, K. and Kanai, K., "The M_2 Seismic Waves," Bulletin of the Earthquake Research Institute, Tokyo University, 13, 471-475 (1935).

42. Baumeister, T., ed., Mechanical Engineers' Handbook, Sixth Edition, McGraw-Hill Book Co., New York (1958).

43. Timoshenko, S., and Goodier, J. N., Theory of Elasticity, Second Edition, McGraw-Hill Book Co., New York (1951).

44. Bradfield, G., "Strength, Elasticity, and Ultrasonics," Ultrasonics, 10, No. 4, 166-172 (July 1972).

45. Brune, J., Nafe, J, and Oliver, J., "A Simplified Method for the Analysis and Synthesis of Dispersed Wave Trains," Journal of Geophysical Research, 65, No. 1, 287-304 (January 1960).

46. Gregson, V., Jr., "A Model Study of Elastic Waves in a Layered Sphere," Bulletin of the Seismological Society of America, 57, No. 5, 959-981 (October 1967).

47. Egle, D. M., and Bray, D. E., "Measurement of Acoustoelastic and Third-Order Elastic Constants for Rail Steel," The Journal of the Acoustical Society of America, 60, No.3, 741-744 (1976).

48. Gold, L., "Compilation of Body Wave Velocity Data for Cubic and Hexagonal Crystals," Journal of Applied Physics, 21, 541-546 (1950).

49. Musgrave, M. J. P., Crystal Acoustics, Holden-Day, San Francisco (1970).

50. Sullivan, P. F. and Papadakis, E. P., "Ultrasonic Double Refraction in Worked Metals," The Journal of the Acoustical Society of America, 33, No. 1, 1622-1624 (November 1961).

51. Alers, G. A., and Liu, Y. C., "Calculation of Elastic Anisotropy in Rolled Sheet," Transactions of the Metallurgical Society of AIME, 236, 482-489 (April 1966).

52. Tittman, B. R., and G. A. Alers, "An Acoustic Surface Wave Method for Rapid, Nondestructive Texture Evaluation," Metallurgical Transactions, 3, 1307-1308 (May 1972).

53. Markham, M. F., "Measurement of Elastic Constants by the Ultrasonic Pulse Method," British Journal of Applied Physics. Supplement No. 6, 556-563 (1957).

54. Reimann, K. J. and Cason, N. J., "Ultrasonic Measurements of Cold-Work Percentages in Type 316 Stainless Steel," Materials Evaluation, 31, No. 7 128-144 (July 1973).

55. Becker, F. L., and Richardson, R. L., "Ultrasonic Critical-Angle Reflectivity," Research Techniques in Nondestructive Testing, R. S. Sharp, Ed., Academic Press, Ch. 4; 91-131 (1970).

56. Becker, F. L., and Richardson, R. L., "Influence of Material Properties on Rayleigh Critical-Angle Reflectivity," The Journal of the Acoustical Society of America, 51, No. 5, Pt. 2, 1609-1617 (1972).

57. Firestone, F. A., and Frederick, J. R., "Refinements in Supersonic Reflectoscopy: Polarized Sound" The Journal of the Acoustical Society of America, 18, No. 1, 200-211 (July 1946).

58. Papadakis, E., "Elastic Wave Velocities in Various Alloy Strips," Metallurgical Transactions, 2, 575-578 (February 1971).

59. Waterman, P., "Orientation Dependence of Elastic Waves in Single Crystals," Physical Review, 113, 5, 1240-1253 (March 1, 1959).

60. Krautkramer, J. and Krautkramer, H., Ultrasonic Testing of Materials, Springer-Verlag, New York (1969)

61. Bray, D. E., and Finch, R. D., "Flaw Detection in Model Railway Wheels," Federal Railroad Administration, Report FRA-RT-71-75, February 1971, PB-199 956, National Technical Information Service, Springfield, Va.

APPENDIX A

PULSE CHARACTERISTICS AND ULTRASONIC CIRCUITRY

A conventional ultrasonic pulsing circuit was used throughout the present study. These circuits are described in several texts (e.g., see Ref. [60]). The discussion which is to follow has been excerpted from Ref. [61].

In this circuit, as shown in Figure 35, the piezoelectric transducer is seen primarily as an electrical capacitance, C_o. A high voltage electrical spike from a source (U_s) causes the piezoelectric ceramic to oscillate.

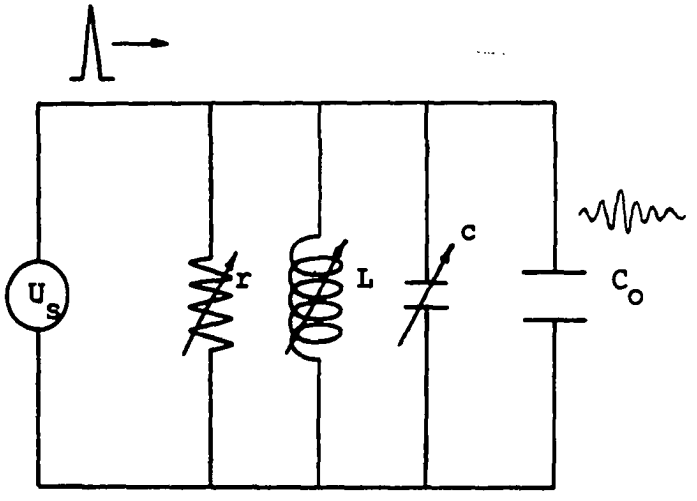

Figure 35. Basic Ultrasonic Pulse Circuit [61]

When excited by the electrical spike, the transducer will, in the ideal case, oscillate at the resonant frequency determined by:

$$f_{re} = \frac{1}{2\pi\sqrt{LC_o}} \qquad (A.1)$$

where L is the inductance of the coil in Figure 35. A piezoelectric transducer also has a mechanical resonant frequency determined by the equation:

$$f_{rm} = \frac{1}{2\pi}\sqrt{\frac{s}{M}} \qquad (A.2)$$

where s is the mechanical stiffness of the transducer material and M is the mass. Optimum performance occurs when the electrical resonant frequency is matched to the mechanical resonant frequency (i.e., $f_{re} = f_{rm}$). Since, for a particular transducer, s, M and C are fixed, this tuning is obtained by varying the inductance L. The electrical damping and, hence, the pulse length, adjusted through the variable resistance r and slight adjustments in the circuit capacitance, can be made through variable capacitor c.

Some of the work discussed in this report was done using, as the ultrasonic source, a Sperry Model UR Reflectoscope. It delivers an electrical spike of approximately 500 volts and contains four tuning inductances which are individually selected by a front panel switch. This selective

type of tuning (i.e., narrow bandwidth) limits its adaptability, since optimum matching of electrical and mechanical resonant frequencies requires small adjustments in the inductance over a large range of values. This difficulty may be overcome by the addition of a second tuning coil connected across the terminals of the crystal, i.e., parallel to C_o.

A typical output pulse obtained by this technique has a decaying, almost sinusoidal, shape, as is shown at the right of Fig. 35. The pulses propagating on new rail, and shown in Figs. 2d and 3d, are very similar in shape to the usual pulse generated by this system. As previously stated, the pulse shape can be optimized by changing the values of the resistance, inductance, and capacitance in the circuit.

Each source transducer used in work related to the propagation on the top of the rail was tuned so that the pulse had the smoothest possible shape and the longest pulse length. This was done by observing the change in the pulse shape with a Panametrics V109, wide-band, highly-damped transducer, which was mounted on the same type of wedge as was used for the source. The wave form was studied as it propagated down the length of a new rail in the send-receive mode previously described. Pulse frequency was obtained in each case by extracting the period directly from the oscillograph of the received pulse.

APPENDIX B

ARRIVAL TIME DETERMINATION

The methodology for arrival time determination can be demonstrated with the traces shown in Fig. 36. This oscillograph shows pulse arrivals at 100 mm, 200 mm, 300 mm, 400 mm, 500 mm, and 600 mm, top to bottom. The 600 mm trace is also shown as the top trace in Fig. 14, with the 100 mm arrival used as the zero reference. The respective arrival times and travel times (t_S and t_R) are marked below the oscillogram. As previously noted in Chapter III, the large pulse emerging from the base line was used as the arrival time, and the smaller signals just ahead of the large pulse were ignored. This choice was subjective, but it led to meaningful results when consistently followed.

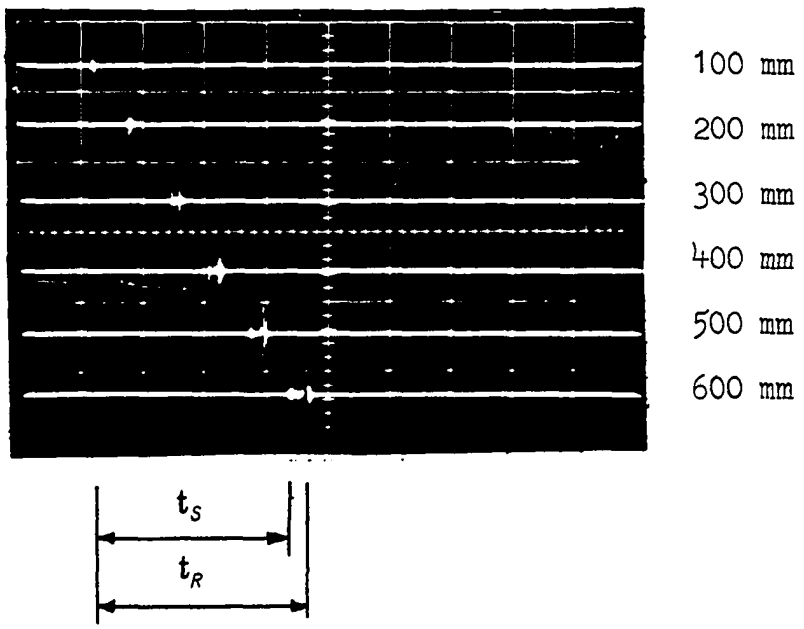

Figure 36. Shear Wave and Rayleigh Wave Arrivals at 2.0 MHz on Rail 11, Vertical 0.2 v/div., Time Base 50 μs/div.